N88-12208

APPENDIX 6

Transform fault earthquakes in the North Atlantic: Source mechanisms and depth of faulting

Eric A. Bergman and Sean C. Solomon

ABSTRACT

We have determined the centroid depths and source mechanisms of 12 large earthquakes on transform faults of the northern Mid-Atlantic Ridge from an inversion of long-period body waveforms. The earthquakes occurred on the Gibbs, Oceanographer, Hayes, Kane, 15°20', and Vema transforms. We have also estimated the depth extent of faulting during each earthquake from the centroid depth and the fault width. For five of the transforms, earthquake centroid depths lie in the range 7-10 km beneath the seafloor, and the maximum depth of seismic faulting is 15-20 km. On the basis of a comparison with a simple thermal model for transform faults, this maximum depth of seismic behavior corresponds to a nominal temperature of 900° ± 100°C. In contrast, the nominal temperature limiting the maximum depth of faulting during oceanic intraplate earthquakes with strike-slip mechanisms is 700° ± 100°C. The difference in these limiting temperatures may be attributed to the different strain rates characterizing intraplate and transfom fault environments. Three large earthquakes on the 15°20' transform have shallower centroid depths of 4-5 km and a maximum depth of seismic faulting of 10 km, corresponding to a limiting temperature of 600°C. The shallower extent of seismic behavior along the 15°20' transform may be related to a recent episode of extension across the transform as a consequence of the northward migration of the triple junction among North American, South American, and African plates to its present position near the transform. The source mechanisms for all events in this study display the strike slip motion expected for transform fault earthquakes; slip vector azimuths agree to 2-3° of the local strike of the zone of active faulting. The only anomalies in mechanism were for two earthquakes near the western end of the Vema transform which occurred on significantly nonvertical fault planes. Secondary faulting, occurring either precursory to or near the end of the main

episode of strike-slip rupture, was observed for 5 of the 12 earthquakes. For three events the secondary faulting was characterized by reverse motion on fault planes striking oblique to the trend of the transform. In all three cases, the site of secondary reverse faulting is near a compressional jog in the current trace of the active transform fault zone. We find no evidence to support the conclusions of Engeln, Wiens, and Stein that oceanic transform faults in general are either hotter than expected from current thermal models or weaker than normal oceanic lithosphere.

INTRODUCTION

The maximum depth of earthquake activity in a region appears to be controlled by the local thermal structure, through the strong temperature dependence of ductile deformation in crustal and upper mantle materials. This relationship has been well established in both continental [*Brace and Byerlee*, 1970; *Sibson*, 1982; *Chen and Molnar*, 1983; *Strehlau*, 1986] and oceanic [*Chen and Molnar*, 1983; *Wiens and Stein*, 1983; 1984; *Bergman et al.*, 1984; *Bergman and Solomon*, 1984; 1985; *Bergman*, 1987] lithosphere. In oceanic lithosphere, except perhaps along the ridge axis proper, the limiting depth of earthquake generation is controlled by the depth of the brittle-ductile transition in the mantle. Comparison of the temperature distribution given by the standard plate cooling model [*Parsons and Sclater*, 1977] with the centroid depths of oceanic intraplate earthquakes suggests that the isotherm limiting the deepest extent of seismic behavior in oceanic lithosphere is approximately 800°C [*Wiens and Stein*, 1983; 1984; *Bergman and Solomon*, 1984; *Bergman*, 1987].

Recently, *Engeln et al.* [1986] applied these ideas to transform faults along the

Mid-Atlantic Ridge. For 29 large transform earthquakes they estimated centroid depths with a body waveform inversion technique. These centroid depths were surprisingly shallow: for 24 earthquakes they obtained a centroid depth 4 km or less below the seafloor; none of the events they examined was found to have a centroid depth in excess of 7 km. On the basis of a simple thermal model of transform faults, they deduced that these depths correspond to temperatures no greater than 400°C. *Engeln et al.* [1986] concluded that either transform fault zones are weaker than normal oceanic lithosphere or else the transforms are significantly hotter than expected from the simple thermal model. If valid, this conclusion would have important implications for the constitution or thermal structure of oceanic fracture zones.

To test the findings of *Engeln et al.* [1986] we conducted body waveform inversions to determine the centroid depths and other source parameters for 12 large earthquakes on six transform faults on the northern Mid-Atlantic Ridge. Eight of these earthquakes are among those investigated by *Engeln et al.* [1986]. We found centroid depths consistently greater than those reported by *Engeln et al.* [1986]. When the finite depth extent of faulting during large earthquakes is considered, the maximum depth of seismic behavior along large-offset transforms in the north Atlantic appears to be generally limited by a temperature similar to or slightly larger than that marking the deepest seismic activity in oceanic intraplate environments.

MAJOR NORTH ATLANTIC TRANSFORM FAULTS

The earthquakes of this study occurred on the six most prominent transform faults

offsetting the Mid-Atlantic Ridge between latitudes 10° and 60°N (Figure 1): the Gibbs, Oceanographer, Hayes, Kane, 15°20', and Vema transforms. These transform faults have all been well studied by marine geophysical surveys, and the good distribution of seismic stations in surrounding areas makes the north Atlantic a nearly ideal region for teleseismic study of earthquake source properties.

For each transform, the characteristics of primary interest for the interpretation of earthquake source parameters are the transform length, the offset in lithosphere age, and the geometry of the active fault traces. In the discussion of active faults, we follow the nomenclature of *Fox and Gallo* [1986]. The zone of most recent faulting in Atlantic transforms is generally localized to a narrow band centered on the axis of the transform valley and consisting of numerous short, transform-parallel fault strands; this band of most recent activity is known as the transform fault zone, or TFZ. Where a single continuous fault strand that appears to be the surface expression of current transform motion can be identified, this strand is termed the principal transform displacement zone (PTDZ). *Fox and Gallo* [1986] distinguish the TFZ from the wider transform tectonized zone, which includes all active and inactive strike-slip structures within the transform fault domain. The intersection of the PTDZ and the neovolcanic zone of the spreading ridge segment at either end of the transform is the ridge-transform intersection (RTI). The neovolcanic zone near an RTI can generally be traced across the nodal basin [*Sleep and Biehler*, 1970] to where it terminates near the base of the opposite wall of the transform valley [*Karson and Dick*, 1983]. Within 5-10 km of the RTI, the neovolcanic zone often displays a significant change in trend, arcing toward

the center of the transform [*Karson and Dick,* 1983; *Macdonald et al.*, 1986]. We have taken this geometry into account in estimating the lengths and age offsets of the transforms in this study; these estimates are slightly lower than those based on the assumption that the RTI occurs at the intersection of the lines marking the regional trends of the transform valley and the adjacent median valley segments. Our estimates of RTI locations, transform length, and age offset for each transform are given in Table 1. Because neither the neovolcanic zone in the adjacent ridge segments nor the PTDZ have been identified for some of the transforms in this study, our locations for these RTIs may be uncertain by 5 km or more.

The principal features of the Gibbs transform (Figure 2) have been described by *Fleming et al.* [1970], *Olivet et al.* [1974], and *Searle* [1981]. The Gibbs is a double transform, consisting of two distinct sections separated by a short ridge segment near longitude 31.7°W [*Fleming et al.*, 1970; *Vogt and Avery*, 1974; *Lilwall and Kirk*, 1985]. The two large earthquakes considered in this paper from the Gibbs transform both occurred on the western (or northern) segment, which has a length of 195 km. From seafloor magnetic anomalies [*Klitgord and Schouten*, 1986], the offset in lithosphere age across the transform is about 22 m.y. The TFZ, identified from GLORIA side-scan sonar images, is 1.5-2 km wide [*Searle*, 1981, 1986]. The strike of the principal faults making up the TFZ is about N91°E near the western RTI, but to the east of a dilatational jog [*Sibson*, 1986] in the central transform the strike is N93°E (Figure 2).

The Oceanographer transform (Figure 3) has been described by *Fox et al.* [1969, 1976], *Phillips et al.* [1975], *Williams et al.* [1984], and *OTTER* [1984, 1985]. On the

basis of GLORIA images, the TFZ is approximately 2 km wide and a PTDZ has been identified along much of the transform length [*Searle*, 1986]. The strike of the transform is about N105°E. The morphology of the eastern RTI is rather typical [*OTTER*, 1984], but the western RTI is markedly more complex [*Williams et al.*, 1984]. According to *Williams et al.* [1984], the present position of the RTI is about 17 km east of the intersection of the transform valley and the most prominent expression of the central magnetic anomaly. They attribute this complexity to local perturbations to the stress regime at the RTI rather than to a recent change in plate motions. With this geometry, the distance between the RTIs is 105 km and the corresponding offset in magnetic anomalies [*Klitgord and Schouten,* 1986] yields a maximum age contrast of 10 m.y.

The Hayes transform (Figure 4), though less well-studied than the other five transforms, has been the target of a conventional geophysical survey [*Feden et al.*, 1975], aeromagnetic profiling [*Phillips et al.*, 1975], and a GLORIA survey [*Searle,* 1986]. From the GLORIA sonographs, the TFZ is well defined by a band 1-2 km wide of linear tectonic elements inferred to be fault scarps; the TFZ has a strike of about N104°E. A reexamination of the GLORIA data by R. C. Searle (personal communication, 1986) indicates that the eastern RTI was misidentified by *Feden et al.* [1975]; the Hayes transform is about 70 km long, and a minor transform about 10 km to the north offsets the ridge axis another 30 km to the east (Figure 4). This interpretation is supported by the bathymetric data of *Feden et al.* [1975], which clearly shows a nodal deep near 33.6°N, 38.3°W, and by the aeromagnetic data of *Phillips et al.* [1975], which indicates that the central anomaly to the immediate north of the Hayes swings sharply

east before trending in a more northerly direction. Because of the complexity of the eastern RTI region, the age offset across the transform is difficult to estimate directly from magnetic anomalies. From the transform length and the slip rate predicted from plate motion model RM2 [*Minster and Jordan,* 1978] the age offset is approximately 6 m.y.

Because of a recent Sea Beam survey [*Pockalny et al.*, 1987] the bathymetry of the Kane transform (Figure 5) is known unusually well, and both RTIs have been investigated in detail [*Karson and Dick*, 1983]. Although the TFZ has been delineated with GLORIA side-scan sonar data [*Roest et al.*, 1984; *Searle*, 1986], no PTDZ has been clearly defined along most of the transform. The transform length is about 150 km; the corresponding age offset is 11 m.y. The regional trend of the transform valley is about N100°E, nearly orthogonal to the neighboring median valley segments, but the trend and width of the TFZ vary along the transform [*Roest et al.*, 1984; *Searle*, 1986]. *Tucholke and Schouten* [1985] report evidence for a number of changes (by several degrees) in spreading direction at the Kane transform in the last 10 m.y.; such changes may account for the geometrical complexities in the TFZ.

The 15°20' transform (Figure 6) has been described by *Collette and Rutten* [1972], *Collette et al.* [1974], and *Roest and Collette* [1986]. The transform valley is about 10 km wide and has a rhomboid shape, bounded by trends of N90-93°E and N98-99°E, [*Roest and Collette*, 1986]. A TFZ about 5 km wide and trending N95.5°E has been reported from side-scan sonar data [*Searle*, 1986; *Roest and Collette*, 1986], but no PTDZ has been identified. The RTIs are separated by 180 km; the corresponding age

offset is about 13 m.y. The unusual shape and width of the transform valley are attributed by *Roest and Collette* [1986] to recent extension across the 15°20' transform caused by a northward migration of the triple junction between the North American, South American, and African plates to a present position near this transform

Characteristics of the Vema transform have been described by *Van Andel et al.* [1971]; *Eittreim and Ewing* [1975], *Rowlett and Forsyth* [1984], *Macdonald et al.* [1986], and *Bowen and White* [1986]. Two well-defined nodal basins at the RTIs are separated by 300 km. The age offset is about 20 m.y. [*Cande et al.*,1987]. Although much of the transform valley is partially filled with sediment, the PTDZ can be identified on the basis of bathymetry along the entire length of the transform [*Macdonald et al.*, 1986]. The average strike of the PTDZ is N93°E, but the strike varies considerably along the transform. Along the western portion of the transform (Figure 7) the strike of the PTDZ is N91°E [*Rowlett and Forsyth*, 1984]. A prominent perturbation to the trend of the PTDZ occurs at about 100 km from the eastern RTI at a large exposure of the median ridge known as the Vema Mound (Figure 8).

EARTHQUAKE DATA SET

During the period 1962-1984, 13 transform fault earthquakes with $m_b \geq 5.5$ occurred along the Mid-Atlantic Ridge system between 10° and 60°N. All were located along the six transform faults discussed above. One of these earthquakes, which occurred on the Vema transform on June 9, 1963 (m_b 5.6), was not sufficiently well

recorded on the limited World-Wide Standard Seismograph Network (WWSSN) then operational for a body waveform inversion study to be worthwhile. The remaining 12 earthquakes are the subject of this study. Epicentral data for these earthquakes are given in Table 2. Eight of these earthquakes were also investigated, to varying levels of detail, by *Engeln et al.* [1986].

Epicentral Bias

The epicenters of most of the earthquakes in Table 2 are taken from the Bulletin of the International Seismological Centre (ISC). As may be seen from Figures 2-8, ISC epicenters for large earthquakes along Atlantic transform faults do not, in general, lie within the TFZ. This is due in part to random error in the epicentral location, arising from reading errors, uneven station distribution, and lateral heterogeneity in Earth structure. For large earthquakes recorded by 100 or more well-distributed stations, this uncertainty should not greatly exceed the formal error calculated in the location procedure and is perhaps 5 km.

For oceanic earthquakes, a potentially larger and non-random error in teleseismic location results when the travel time tables are based on a velocity model incorporating a thick crust in the source region, as is the case with the *Jeffreys and Bullen* [1940] tables used by the ISC. The predicted travel times from shallow oceanic events will be systematically too large, and the epicenter will be "pulled" toward the greatest concentration of seismic stations. For the central north Atlantic, a predominance of stations at northern azimuths imparts a northward bias to the epicentral locations

[*Phillips et al.*, 1979]. This bias in latitude varies among the transforms considered here. The ISC epicenters of earthquakes on the Vema transform, the southernmost in our study, lie to the south of the PTDZ by about 5 km (Figures 7 and 8). On the 15°20' transform the ISC epicenters are about 5 km to the north of the TFZ (Figure 6). The ISC epicenters of large earthquakes on the remaining transforms all fall to the north of the respective TFZ by 10 to 15 km (Figures 2-5). The fact that the teleseismic epicenters of large, well-recorded earthquakes on the spreading center segments of the northern Mid-Atlantic Ridge lie very near the median valley axis [e.g., *Huang et al.*, 1986] suggests that there is little bias to the estimates of longitude for earthquakes in this region, as we would expect from the generally comparable distribution of seismic stations to the east and west.

Earthquake Relocations

The 1962 Vema and 1963 Kane earthquakes predate the ISC. Epicenters for these events were reported by the International Seismological Summary (ISS) and the U.S. Coast and Geodetic Survey (USCGS). For the 1962 Vema event, the USCGS epicenter is 7 km north of the PTDZ within the Vema transform, while the ISS epicenter is 17 km south of the PTDZ; the longitudes for the two locations differ by no more than about 10 km (Figure 7). These deviations in latitude from the most likely fault trace are not significantly larger than those of more recent epicenters determined by the ISC, but confidence in these epicenters is diminished by an unusually large (3.3 s) standard error in the ISS epicenter and a reported depth of 75 km (the USCGS assumed a depth

of 33 km). Examination of the P waves on several short-period records indicates that a small precursor occurred 4-5 s before the mainshock. The location of the 1962 Vema earthquake may therefore be biased to the extent that many of the reported first arrivals for this event are from the precursor. The ISS epicenter for the 1963 Kane earthquake is 70 km north of the center of the TFZ, while the USCGS epicenter, with virtually the same longitude, lies at the northern edge of the TFZ.

Because of the epicentral uncertainties suggested by these discrepancies we relocated both earthquakes. On the basis of the waveform inversion results reported below, we assumed focal depths of 10 km beneath the seafloor for both events. We performed relocations both with the latitude fixed and with latitude as a free parameter, using the single-event location algorithm of *Jordan and Sverdrup* [1980]. Theoretical travel times were obtained from the *Herrin* [1968] tables and the mean station corrections of *Dziewonski and Anderson* [1983].

In our relocation study of the 1962 Vema earthquake we confirmed that many reported arrival times listed by the ISS are for the precursor. By fixing the focal depth at 10 km, the latitude at that of the PTDZ, and the longitude at various locations along the transform and by successively downweighting stations with large negative residuals, we obtained an initial estimate of the mainshock epicentral coordinates and we identified most of the erroneous arrival time data. For the final location, we eliminated stations reporting a first arrival more than 3 s earlier than the predicted arrival time for the initial location; to avoid biasing the solution we also removed stations with positive residuals in excess of 3 s. The epicenter obtained with this reduced data set and with

only focal depth constrained (Table 2) is 20 km east of the ISS epicenter and 11 km south of the PTDZ (Figure 7). The residual error is virtually unchanged if the latitude is fixed at that of the PTDZ. Figure 9 shows a histogram of the residuals at all stations for this location. The secondary peak in residuals about 5 s early represents those stations reporting the arrival time of the precursor.

For the 1963 Kane earthquake we first fixed the focal depth at 10 km and the latitude and longitude at those of the USCGS epicenter, and we solved for the best-fitting origin time. With this initial location and with latitude, longitude, and origin time as free parameters, the location procedure converged to the solution given in Table 2. The epicenter is a few kilometers north of the TFZ (Figure 5).

WAVEFORM INVERSION

Procedure

For each of the events listed in Table 2 we determined the parameters of the best-fitting double-couple point source, using a formal inversion of long-period teleseismic P and SH waveforms [*Nabelek*, 1984]. The waveform data were digitized from WWSSN records and corrected for differences in magnification and epicentral distance, as described by *Bergman et al.* [1984]. The quantities to be determined in the inversion are the focal mechanism, the centroid depth, the scalar seismic moment, and the source time function (STF), which is generally parameterized as a series of overlapping triangular elements of assigned number and length. The relative amplitudes of the time function elements are determined in the inversion; the number of

elements is chosen so that the end of the STF approaches zero smoothly. If all waveforms were given equal weight, the SH waves would dominate the inversion, because the average amplitude of SH waves from strike-slip earthquakes is typically 3-5 times larger than that of P waveforms. All the SH waveform data in our inversions were therefore downweighted, relative to the P waveforms, by a common factor (usually 0.2-0.3) chosen so that the contributions to data variance from P and SH waveforms were approximately equal.

For larger earthquakes a point-source model is sometimes inadequate to match the observed waveforms. In such cases we can approximate the finite extent of the source in the body waveform inversion in two ways: (1) by parameterizing the rupture process as two (or more) point sources separated in space and time, or (2) by incorporating a model of unilateral horizontal rupture in the STF. In a multiple-subevent model the timing and location of the second subevent relative to the first are included as parameters in the inversion, as are the source parameters of the second subevent. For all large earthquakes in this study the relative locations of the subevents were constrained to lie along the strike of the transform. The model of unilateral horizontal rupture incorporates trapezoidal STF elements, the lengths of which are simple functions of the assumed rupture velocity and the angle between the rupture direction (always horizontal and along the strike of one of the nodal planes) and the departing ray path to each respective station [*Ben-Menahem*, 1962; *Nabelek*, 1985]. The waveform data are sensitive to the direction of rupture but not to the precise value assumed for the rupture velocity; we assumed a rupture velocity of 3.5 km/s (75% of the

upper mantle shear velocity) in all cases.

The procedure followed by *Engeln et al.* [1986] to estimate source parameters of transform fault earthquakes differs from ours in several respects. Because our conclusions regarding the source parameters of oceanic transform earthquakes are at variance with those of *Engeln et al.* [1986], these differences in procedure are worth noting. In a later section we discuss the extent to which procedural differences in the estimation of source parameters may account for the discrepancies between our results and those of *Engeln et al.* [1986].

From a combination of first motion polarities, forward modeling of long-period P waves, and Rayleigh wave spectral amplitudes, *Engeln et al.* [1986] estimate the parameters of the focal mechanism. With the mechanism held fixed and with the centroid depth constrained to a variety of values, a simultaneous deconvolution procedure is applied separately to the P and SH waveform data to retrieve the best-fitting STF for each type of waveform data. Only 5-6 waveforms of each type can be accommodated in this procedure [S. Stein, personal communication, 1986]. The minimum in the curve for residual versus depth is chosen as the preferred centroid depth. It is unclear whether any criterion is applied as to the form of the STF, or how discrepancies between the centroid depths indicated by P and SH waveform inversions are resolved. Refinement in some source parameters is achieved by fixing all parameters except one and performing deconvolutions in the vicinity of the preferred solution.

Structure of the Source Region

The choice of a velocity structure for the source region can have a significant effect on the results of a body waveform inversion study. The velocity structure obviously influences the estimated centroid depth, through the delay times of surface-reflected phases, but it also affects the estimated source parameters through the calculation of takeoff angles. An example of this effect is discussed by *Jemsek et al.* [1986].

Detailed refraction and gravity studies of the crustal structure have been carried out in the transform and nontransform portions of several of the fracture zones in this study, including the Vema [*Ludwig and Rabinowitz*, 1980; *Detrick et al., 1982; Bowen and White, 1986; Louden et al., 1986*], Kane [*Detrick and Purdy, 1980; Louden and Forsyth,* 1982; *Cormier et al., 1984*], Oceanographer [*Fox et al.*, 1976; *Sinha and Louden*, 1983; *Ambos and Hussong*, 1986], and Gibbs [*Calvert and Whitmarsh*, 1986] fracture zones. From these and other studies, the crustal structure of large-offset, slow-slipping transforms appears to be characterized by extreme variability, but with crustal thicknesses and seismic velocities generally less than are observed for normal oceanic crust [e.g., *White et al.*, 1984]. For example, a crustal thickness of as little as 1 km has been reported at the eastern nodal basin of the Kane transform [*Cormier et al.*, 1984], and depths of 2-3 km to material with velocities appropriate to the upper mantle have been inferred for extensive areas within several fracture zones [e.g., *Detrick and Purdy*, 1980; *Sinha and Louden*, 1983; *Cormier et al.*, 1984; *Mutter et al.*, 1984]. Conspicuously absent in most of the transform regions studied is evidence for the presence of a distinct layer 3 in the crust beneath the transform valley [e.g., *Detrick et*

al., 1982; *Louden et al.*, 1986].

In light of the variability in crustal structure within oceanic transforms, it is not possible to specify with confidence a source velocity structure for a body waveform inversion study except where detailed seismic experiments have been conducted in the neighborhood of the earthquake epicenter. Such a situation does not hold for most of the events in this study. We have therefore adopted what we consider to be a representative velocity structure, based most directly on the studies by *Bowen and White* [1986] and *Louden et al.* [1986] of the Vema transform. This velocity structure (Table 3) incorporates a two-layer crust with a total thickness and average velocity somewhat lower than for normal oceanic crust. For several transforms (Vema, Gibbs) there are significant thicknesses of sediment in the transform valleys. As noted in the discussion of the individual events, we include a sediment layer in the velocity structure for earthquakes in such regions.

Resolution of Centroid Depth

The ability to determine the centroid depth of moderate-size earthquakes to within a few kilometers is one of the principal strengths of the body waveform inversion technique. The resolution of centroid depth with this method has nonetheless been difficult to formalize, although aspects of the problem have been discussed by *Nabelek* [1984], *Christensen and Ruff* [1985], *Huang et al.* [1986], *Stein and Wiens* [1986], and *Goff et al.* [1987]. We summarize the results of these studies, as well as our own experience using body waveform inversion to determine average source parameters

for earthquakes spanning a wide range of sizes, mechanisms, depths, and tectonic environments, as follows. Under the best of circumstances the uncertainty in centroid depth using long-period WWSSN data is about 1-2 km. Assuming good signal-to-noise (S/N) ratios and station distribution, such an uncertainty is typically obtainable for moderate size earthquakes with dip-slip mechanisms at centroid depths greater than about 10 km, but not so deep (> 30 km) that uncertainty in the velocity structure becomes a serious additional source of error. In contrast, depth resolution for large, shallow strike-slip earthquakes with incomplete station distribution can be so poor that no depth between the surface and 15-20 km may be excluded [e.g., *Goff et al.*, 1987]. With the procedures used here, a reasonable rule-of-thumb for the transform earthquakes in this paper is that the uncertainty in the centroid depth is 2-5 km, subject to a long list of potentially qualifying factors including the S/N ratio, the station distribution, and the size, focal mechanism, depth, and complexity of the event.

The best approach to gaining an understanding of the resolution of centroid depth for a particular earthquake is to conduct a series of inversions with the depth fixed at various values over a wide range, solving at each depth for the combination of remaining parameters which best matches the observed data. Even with the depth fixed, the problem is highly non-linear, and it is easy to miss combinations of source parameters that, at certain depths, yield a misfit as low as that produced by the preferred solution. In this exercise the alignment between observed and synthetic waveforms at each station is a critical adjustable parameter, though it is not included in the formal inversion. While statistical approaches to the use of solution misfit to provide

a formal estimate of depth resolution have been explored [e.g., *Huang et al.*, 1986], such procedures involve somewhat arbitrary assumptions, such as the number of independent data in each waveform.

For the source studies of transform fault earthquakes in this paper, we base each estimate of centroid depth on an extensive series of inversion solutions with centroid depth constrained to various values. The misfit to be minimized for each inversion is the residual variance, defined as the weighted mean squared difference between observed and synthetic waveforms divided by the data variance (the weighted mean squared observed waveforms). On the basis of each series of inversions, we attempt to identify the range in centroid depth over which the residual variance is indistinguishable from the minimum value. A measure of distinguishability which is both compatible with the formal statistical test of *Huang et al.* [1986] and easier to implement is a change in the residual variance by more than 1% of the data variance. We believe that the range in centroid depth over which the residual variance is a minimum and varies by no more than 1% of the data variance provides a simple yet conservative estimate of the uncertainty in centroid depth, providing of course that a sufficiently vigorous attempt has been made to explore the full parameter space in the vicinity of each centroid depth [see also *Goff et al.*, 1987]. Because the actual fault rupture occurred over a finite depth interval, we regard the range in acceptable centroid depths for the best fitting point source as an approximate measure of the depth range over which significant fault slip occurred. By this view the midpoint of this range provides the preferred estimate of centroid depth, even if the residual variance at this

depth is not the absolute minimum.

The centroid depth chosen in this manner may be refined if depth phases can be identified, even if only from a small subset of the waveform data. Our experience has shown that the least-squares error criterion commonly employed as a measure of waveform misfit is frequently rather insensitive to the relatively short-period signals of the depth phases [e.g., *Huang et al.*, 1986], particularly for sources at shallow depths where direct and surface-reflected phases are not fully separated on long-period seismograms. The first half cycle of motion in many of the P waveforms from the transform fault earthquakes in this study displays a double-peaked character which we interpret as due to the delay between the direct P phase and the largest surface-reflected phase (usually sP). It is well known, however, that synthetic waveforms with apparent depth phases can be generated for an earthquake with a strike-slip mechanism by placing the centroid at the free surface (or 1-2 km depth) and invoking a multiply peaked STF. We generally discount such solutions for the large earthquakes of the present study, however, because of the implausibility of many of the implied source parameters (e.g., stress drop) if slip occurred on a fault having such a narrow width. Further, interpreting the double-peaked P waveforms as due to distinct direct and surface-reflected phases leads to estimates of centroid depths that lie in a narrow range, approximately 7-10 km, for all but one transform in this study. It is improbable that earthquake source complexity would consistently mimic depth phases appropriate to such a narrow range of depths.

Curves of residual variance versus centroid depth for two of the earthquakes of this

study are shown in Figure 10a. The curve for the 1967 Gibbs earthquake is typical of those we have found for large, shallow, strike-slip events; the residual variance is nearly constant over a significant range of centroid depths. The 1976 Hayes earthquake, in contrast, has a short STF, clear depth phases, and consequently a sharp minimum in residual variance between centroid depths of about 7 and 9 km. It may be seen that the 1% residual variance criterion and the formal *t* test of *Huang et al.* [1986] lead to similar uncertainties in the best fitting centroid depth. For both events there are also minima in residual variance at very shallow centroid depths; we reject these solutions, however, for the reasons discussed above. The manner in which the STF of the 1976 Hayes event develops two peaks at very shallow centroid depths, to mimic the depth phases, is illustrated in Figure 10b.

The source parameters obtained from waveform inversion are summarized in Table 2. A discussion of the inversion for each event is given in Appendix A. Additional source parameters (fault dimensions, stress drop, average slip) derived from the parameters estimated directly in the inversions are discussed in Appendix B and are given in Table 4. The focal mechanisms determined in the inversion studies are depicted in map view in Figures 2-8.

DEPTH OF FAULTING AND THERMAL MODELS OF TRANSFORM FAULTS

The best-fitting values of centroid depths for large strike-slip earthquakes on north

Atlantic transforms fall in the range 4-10 km beneath the seafloor (Table 2). Nine of the 12 events have centroid depths within the narrower range 7-10 km. The three earthquakes with centroid depths shallower than 7 km all occurred on the 15°20' transform. The comparatively shallow centroids of these earthquakes (4-5 km) cannot be attributed to the size of the events. The 1969 earthquake on the 15°20' transform had one of the larger moments of the events in this study, and the remaining two events were comparable in size to earthquakes with deeper centroids on other transforms. The centroid depths we obtained, both for transform events as a class and for individual events (including those on the 15°20' transform), are systematically greater than those reported by *Engeln et al.* [1986]. We elaborate on these differences and on possible causes in a later section.

For earthquakes as large as those of this study, it is necessary to consider the depth extent of seismic slip, or the fault width, in any assessment of the maximum depth of seismic behavior along transforms. For the five largest events in the study, each with a source time function at least 8 s long, we assume that the rupture surface extended from the seafloor to twice the centroid depth. This assumption may yield a slight overestimate of the depth extent of rupture if the distribution of moment release in the earthquake is weighted toward the lower part of the rupture zone. For the seven smaller events, we estimated the depth extent of rupture by means of a simple model of the rupture surface as a circular fault centered at the centroid depth, with the fault radius determined by the length of the STF (see Appendix B). The depth extent of rupture determined in this way is generally less than twice the centroid depth, but this

difference is significant only for the 1976 Hayes earthquake. The vertical extent of rupture so estimated for each event is depicted in Figures 11 and 12. The maximum depth of seismic behavior, following these arguments, is 15-20 km for most of the large-offset transforms in the north Atlantic and is about 10 km for the 15°20' transform.

Comparison with a Thermal Model for Transforms

To compare the maximum depth of seismic failure with the temperature at that depth we need to know the thermal structure of the transform. We assume that the temperature in the lithosphere on either side of the transform fault is that given by the plate cooling model of *Parsons and Sclater* [1977], and that because of efficient lateral heat conduction the temperature along the transform is given by a simple average of the temperature distributions in the adjoining lithospheric blocks [*Forsyth and Wilson*, 1984; *Phipps Morgan and Forsyth*, 1987]. Because the plate cooling model is unrealistic in the immediate vicinity of the ridge crest, we do not calculate temperatures along portions of the transforms where the lithosphere on either side is less than 0.5 m.y. old. It should be emphasized that the nominal values of temperature as a function of depth given by this simple model should not be accorded great significance; most isotherms are almost certainly too shallow, for instance, since the model does not account for the cooling effects of hydrothermal circulation. For the purpose of comparison with the depths of oceanic intraplate earthquakes, however, an internally consistent set of assumptions for the thermal model is more important than the accuracy of the model.

Selected isotherms calculated in the manner described above are shown in cross section for the six transforms in Figures 11 and 12. The most notable feature of the transform thermal model is the flatness of the isotherms. For a transform with 10 m.y. age offset, for instance, the 600°C isotherm is about 9 km deep at the center of the transform and shoals by only about 4 km near the RTI. The isotherms predicted by more sophisticated thermal models [*Phipps Morgan and Forsyth*, 1987] are even flatter in cross-section (a 3 km variation in depth for the example cited). Because of the nearly constant depth of isotherms within the transform, the maximum depth of faulting should not vary substantially with position along any given transform fault zone.

For five of the six transforms of this study, the maximum depth extent of faulting during large earthquakes coincides with the depth of an isotherm given nominally by 900° ± 100°C. As expected from the thermal model, the maximum depth extent indicated by two or more earthquakes on the same transform are generally consistent. The relative shallowness of the rupture zone of the Vema transform earthquake of August 25, 1979 (Figure 11), might be considered an exception, but the maximum depth of faulting during this event may have occurred during the reverse-faulting precursor, rather than the main rupture, which is depicted in Figure 11 (see Appendix A).

In constrast to the other five transforms, the 15°20' transform is anomalous in that seismic slip for the three earthquakes studied was confined to depths less than about 10 km; this depth corresponds to the nominal 600°C isotherm. As noted earlier, the 15°20' transform is unusual in the width and shape of the transform valley and TFZ

[*Searle*, 1986; *Roest and Collette*, 1986], features that may be associated with a recent episode of extension across the transform as the triple junction among the North American, South American, and African plates migrated northward to the approximate latitude of this transform [*Roest and Collette,* 1986]. Such an episode of leaky transform behavior may have led to a thermal structure significantly hotter than that given in Figure 11.

Comparison with Oceanic Intraplate Earthquakes

To evaluate the extent to which the mechanical behavior of oceanic transforms differs from that of typical oceanic lithosphere we must compare the depth extent of faulting in transform earthquakes with equivalent data for oceanic intraplate earthquakes. We base our comparison on the results of source studies of oceanic intraplate earthquakes obtained with the same body waveform inversion technique as has been used for the transform events [*Bergman et al.* 1984; *Bergman and Solomon*, 1984, 1985; *Bergman*, 1987]. Because of the dependence of brittle strength on the orientation of the principal stresses [*Brace and Kohlstedt,* 1980] we include only those oceanic intraplate earthquakes with strike-slip mechanisms, defined as having a slip angle within 20° of either 0° or 180°. Eighteen such earthquakes, in lithosphere between ages of 9 and 90 m.y., have been studied with our body waveform inversion procedure; we estimated fault dimensions for these earthquakes in the same manner as for the transform events (Appendix B). The resulting data are plotted as a function of lithosphere age in Figure 13. Also included in the figure are isotherms calculated from

the plate cooling model [*Parsons and Sclater,* 1977] that formed the basis for the simple thermal model of transforms. Faulting during oceanic intraplate earthquakes with strike-slip mechanisms appears to be limited to depths shallower than a nominal temperature of 700°±100°C.

The observation that the temperature limiting the maximum depth of faulting in transform earthquakes is somewhat greater than that which limits the depth of faulting in intraplate events is attributable, at least in part, to the difference in strain rates which likely characterize deformation in the two environments. If the maximum depth of faulting is controlled by the depth of a brittle-ductile transition or by a limit on differential stress in the ductile regime, the depth at which this condition is met will be a function of strain rate as well as the temperature distribution [e.g., *Goetze and Evans*, 1979]. As has been noted by *Engeln et al.* [1986], the higher average strain rates in transforms compared with intraplate environments should, for a given flow law, permit seismic behavior to extend to depths corresponding to a greater limiting temperature.

To quantify this argument, we consider the illustration (Figure 8) of *Bergman and Solomon* [1984] of the depth at which various stress levels would be reached in an olivine mantle as a function of lithospheric age and for ductile strain rates of 10^{-15} s^{-1} and 10^{-13} s^{-1}. Although the strain rates typical of intraplate deformation are poorly known and may vary substantially, 10^{-15} s^{-1} is approximately representative of the rate of lithospheric deformation associated with large intraplate earthquakes [*Wiens and Stein*, 1983; *Bergman and Solomon*, 1984]. A strain rate of 10^{-13} s^{-1} is appropriate for the transform fault zones treated in this study [e.g., *Engeln et al.*, 1986]. For lithosphere

10 m.y. old (or for the center of a transform with a 20 m.y. age offset), the depth at which the stress difference is 1 kbar increases from 17 to 19.5 km as the strain rate increases from 10^{-15} s^{-1} to 10^{-13} s^{-1}, with a corresponding increase in the temperature at that depth from 750° to 850°C. The change in the temperature will, of course, vary with the choice of lithosphere age, limiting stress difference, and strain rates. Given the uncertainties in our estimates of these quantities, we consider the difference of 200° ± 150° in the nominal temperatures marking the maximum depth of faulting for oceanic transform and intraplate earthquakes to be largely attributable to the strain-rate dependence of the relations governing ductile flow in the oceanic upper mantle.

ANOMALOUS FOCAL MECHANISMS

In their study of Atlantic transform earthquakes, *Engeln et al.* [1986] drew attention to events with mechanisms differing significantly from transform-parallel strike-slip motion on steeply dipping fault planes. They reported source mechanisms that were anomalous in this sense for 8 earthquakes, or 20 percent of the events for which they determined mechanisms.

Two of the earthquakes (May 14, 1976, and August 25, 1979, Vema transform events) in this study are among those for which *Engeln et al.* [1986] reported anomalous mechanisms. They suggested that the 1979 earthquake is characterized by reverse faulting. As we describe at greater length in Appendix A, however, this event involves primarily strike-slip faulting but has a small reverse-faulting precursor; the strike-slip component is not anomalous. Two additional earthquakes (June 6, 1972

and April 22, 1979) on the list of *Engeln et al.* [1986] of anomalous transform events were studied by *Huang et al.* [1986]. Combined inversion of P and SH waveforms for these two events indicates that the mechanisms involve primarily normal faulting, in agreement with their epicentral location in the Mid-Atlantic Ridge median valley [*Huang et al.*, 1986].

Only two events in this study displayed anomalous focal mechanisms: the Vema transform earthquakes of March 17, 1962, and May 14, 1976. The anomalous character of the latter event was noted by *Engeln et al.* [1986]; the former event was not among the earthquakes in their study. The probable fault planes of these two events, which are both at the western end of the transform, dip to the north (toward younger lithosphere) at an angle near 50°-60°. Another moderate earthquake (M_s 5.8) occurred between the epicenters of the 1962 and 1976 events on January 10, 1985 (Figure 7). A centroid moment tensor solution [*Dziewonski et al.*, 1985] for the 1985 event is characterized by strike-slip motion on a nearly vertical fault (dipping 84° to the north), but a more detailed source study is warranted to determine whether a fault geometry similar to that of the two flanking events provides an equally good fit to the waveforms.

Two hypotheses for the anomalous dip angles of the fault planes may be suggested. A tendency for the fault plane of transform earthquakes near RTIs to dip toward the younger lithosphere was predicted by *Fox and Gallo* [1984], on the grounds that the thinner lithosphere would be easier to fracture than the older and thicker plate on the opposite side. One difficulty with this proposal, however, is that it does not hold

as a general rule. Neither the May 17, 1964, nor the December 9, 1972, earthquake near RTIs on the Oceanographer and 15°20' transforms, respectively, show anomalous dip angles (Figures 3 and 6). A second possibility is that the shallow dip angle is related to the deep structure of the prominent transverse ridge to the south of the western Vema transform. Significant vertical motions of this transverse ridge have been documented and attributed in part to diapiric rise of altered mantle material [*Bonatti et al.*, 1983]. Limited gravity anomaly data are consistent with a northward-dipping upper boundary to the block of altered mantle beneath the ridge [*Robb and Kane*, 1975].

For the remaining 10 events of this study, strike slip motion occurred on faults with a dip angle within about 5° of vertical and (with one exception) a slip angle within 5° of either 0° or 180°. The exception is the 1979 Vema transform earthquake, with a slip angle of 172°. This event, however, had an impulsive reverse-faulting precursor, so some loss of resolution of the source parameters of the strike-slip subevent is to be expected.

SLIP VECTOR AZIMUTHS

The slip vectors of transform earthquakes provide important information on relative plate motions. The azimuths of the slip vectors for the transform earthquakes of this study are listed in Table 5. For those earthquakes with a multiple-subevent source model we give the slip vector for the primary strike-slip subevent. For comparison we also list a representative strike direction for each transform, obtained by averaging the

strike direction at the endpoints of the great circle segment connecting the two RTIs (Table 1). If the active part of the transform is composed of several en echelon segments, the strike of individual segments will differ systematically from this strike direction, but this difference should be at most a few degrees. With the exception of one event, the slip vector azimuths in Table 5 agree with the representative strike directions of the transform to within 3°. For the exception, the earthquake of August 25, 1979, on the Vema transform, the corresponding slip vector azimuth closely matches the local trend of the PTDZ, which has been mapped in detail in the epicentral region (Figure 8). On the basis of this agreement, as well as the consistency of slip directions for earthquakes on the same transform, we estimate that the uncertainty in slip vector azimuth for the transform events in this study is no more than 3°.

Also shown for comparison in Table 5 are the slip vector azimuths reported by *Engeln et al.* [1986] for events common to both studies. Their slip directions show considerably more scatter among earthquakes on the same transform, as well as poorer agreement with the strike directions of the transforms. The highly anomalous value for the slip vector azimuth they obtained for the 1979 Vema earthquake is a consequence of their having modeled the earthquake with a reverse-faulting mechanism (see above and Appendix A).

SECONDARY FAULTING

Among the earthquakes studied several displayed evidence of source complexity. For three events (1979 Vema and 1963 and 1980 Kane earthquakes) a significant

improvement to the source model was achieved by including a secondary subevent involving reverse faulting on a plane striking oblique to the trend of the transform. In the 1979 Vema earthquake, an episode of reverse faulting preceded the primary strike-slip rupture, while for the two earthquakes on the Kane transform reverse faulting apparently occurred near the cessation of rupture for the primary strike-slip subevent.

For all three earthquakes the locus of reverse faulting is probably attributable to irregularities in the geometry of the PTDZ. The 1979 Vema earthquake occurred near a compressional jog [*Sibson*, 1986] in the PTDZ in the vicinity of the Vema Mound (Figure 8). On the basis of the source parameters and relative timing and location of the two subevents, we suggest (see Appenidix A) that the central portion of the transform was temporarily locked by enhanced compressive stress across the fault at this jog, and that the failure of this barrier by the reverse-faulting subevent initiated more extensive strike-slip faulting along the transform to the east of the jog.

For the Kane transform, tectonic lineaments identified from GLORIA sonographs [*Roest et al.*, 1984; *Searle*, 1986] and demarking the TFZ (Figure 5) suggest that the principal faults change strike by several degrees near longitude 45°35'W (near the epicenter of the earthquake of March 26, 1980) and near 46°W (near the epicenter of the earthquake of May 19, 1963). While *Garfunkel* [1986] and *Pockalny et al.* [1987] have suggested that the PTDZ follows a straight line linking the two RTIs, on the grounds that such a trace would not cut through any major bathymetric features, a PTDZ characterized by several changes in strike would be in better agreement with the detailed bathymetry and with GLORIA images. Such changes in trend may have been

the result of the several minor changes in the direction of spreading in the last 10 m.y. noted by *Tucholke and Schouten* [1985]. For the 1963 earthquake, the reverse-faulting subevent apparently occurred spatially and temporally near the end of the rupture zone of the primary strike-slip subevent and can be interpreted as accompanying the stoppage of the eastward-propagating rupture of the strike-slip subevent at a compressional jog in the fault surface. For the 1980 event, in contrast, reverse faulting occurred near the centroid of the strike-slip subevent and at a shallower depth. The source time function of the reverse faulting subevent for the latter earthquake is quite long considering the small seismic moment; a low stress drop is suggested.

DISCUSSION

As noted above, the centroid depths we obtained for transform fault earthquakes are systematically greater than those reported by *Engeln et al.* [1986], both as a group and for individual events. Further, our analysis of the depth extent of faulting on oceanic transform faults does not support their conclusion that the maximum depth of seismic behavior occurs at a nominal temperature considerably less than that which limits the deepest extent of oceanic intraplate earthquakes. In this section we consider possible causes for these different findings.

Centroid Depths

A direct comparison of the centroid depths estimated by *Engeln et al.* [1986] with those in this paper can be made for the seven earthquakes for which depths were

determined in both studies. These seven events include two on the Gibbs transform, three on the 15°20' transform, and two (1976 and 1979) on the Vema tranform. The centroid depths reported by *Engeln et al.* [1986] for the two Gibbs transform earthquakes are 3-6 km shallower than those obtained here; their depths are 2 km shallower than those in Table 2 for all three events on the 15°20' transform; and their depths are 6-8 km shallower than those given here for the Vema transform earthquakes. For the largest of these events the trade off between centroid depth and source time function does not permit us to reject the centroid depths reported by *Engeln et al.* [1986] solely on the basis of residual variance (e.g., Figure 10a). For at least three earthquakes (the 1970 and 1972 events on the 15°20' transform and the 1976 Vema event), however, the centroid depths reported by *Engeln et al.* [1986] lie outside the range of acceptable values indicated by waveform inversion, given the assumption that we have correctly identified depth phases in the P waveforms from these events. Even if the shallower centroid depths reported by *Engeln et al.* [1986] cannot formally be rejected by waveform misfit criteria on an event-by-event basis, one can question why all of their depths are systematically shallower than those obtained here. A recent comparison of centroid depths determined by us for intraplate earthquakes with those found for the same events by methods ostensibly identical to those employed by *Engeln et al.* [1986] showed that the best-fitting centroid depths typically agree to within about 2 km and that neither set of depths is systematically shallower than the other [*Stein and Wiens,* 1986]. We believe that several aspects of the procedure employed by *Engeln et al.* [1986] to determine earthquake source parameters misled them to infer

incorrect centroid depths.

First, by fixing the focal mechanism during inversions for depth, they restricted unnecessarily the volume of solution space they investigated and they were unable to explore trade offs between the mechanism and other source parameters, trade offs that can be significant for strike slip events. By inverting P and SH waveforms separately, they do not enforce a consistent source description. As noted above, for instance, by not requiring a solution to match amplitudes of both P and SH waves simultaneously, they inferred an incorrect mechanism for the 1979 Vema transform event. Trade offs between mechanism and other parameters can be particularly severe when only a small number of waveforms are inverted at one time, as in the procedure of *Engeln et al.* [1986]. It has been our experience that waveform inversions become increasingly susceptible to bias in parameter estimation, simply from the choice of stations and the details of the data processing, as the number of stations falls below about ten.

Apparently, no attempt was made by *Engeln et al.* [1986] to realign synthetic and observed waveforms during the course of the inversions. In effect, as noted earlier, these alignments constitute additional parameters in a source study, parameters to which a least-squares error criterion is quite sensitive, especially when the number of waveform data is small. We suspect that the narrow minima displayed by curves for residual versus centroid depth given by *Engeln et al.* [1986], rather than indicating well-resolved depths, reflect an artificial circumscription of parameter space by failure to adjust the alignment of synthetic and observed waveforms as necessary to achieve an optimal fit. The correct "starting point" for the best-fitting point-source model is

frequently difficult to determine from inspection and is very dependent on the focal mechanism assumed. The only procedure we have found that permits a full exploration of parameter space is to perform inversions with a wide variety of starting models and with the alignment of waveforms optimized for each starting model.

A possible signature of systematic errors in the centroid depths reported by *Engeln et al.* [1986] is provided by the duration of the source time functions they obtained. They reported a narrow range of STF durations (5-11 s) for events varying in seismic moment by a factor of 150 (3×10^{24} to 5×10^{26} dyn cm). Taken at face value, these results would require large variations in the rupture process (e.g., stress drop) between the smallest and largest events. For two nearby events on the Romanche transform (March 24, 1966, and August 5, 1971), for instance, *Engeln et al.* [1986] report virtually identical centroid depths and STF durations, but the moments differ by nearly two orders of magnitude. This is the pattern one would expect if the source time functions of the smaller earthquakes were obtained at a centroid depth much shallower than the true value, so the extended duration and multiple peaks of the STF mimic the effect of the depth phases.

Depth Extent of Faulting

The method used by *Engeln et al.* [1986] to estimate the depth extent of faulting differs from ours, which was designed to exploit the estimates of centroid depth and STF in a manner consistent with the physical significance of these source parameters (Appendix B). *Engeln et al.* [1986] do not explicitly relate the STF to the spatial

distribution of rupture. Starting with the relation between stress drop, seismic moment, and fault dimensions (see equation B3) and assuming for all events a fault aspect ratio of 3 and a stress drop of 30 bar, they estimated fault width from the seismic moment through the expression

$$w = \sqrt[3]{\frac{2\,M_0}{3\pi\,\Delta\sigma}}$$

Typical values of fault width calculated with this formula are: 2, 4, and 9 km for $M_0 = 10^{24}$, 10^{25}, 10^{26} dyn cm, respectively. The uncertainty in the assumed values for fault aspect ratio and stress drop combine to produce an uncertainty of at least an order of magnitude in the denominator in the above expression, which leads to an uncertainty in w of at least a factor of 2. Worse, some of the source parameters reported by *Engeln et al.* [1986] are inconsistent with these assumed values. The Romanche transform earthquakes noted above, for example, cannot have occurred on faults with the same aspect ratio and stress drop if the source parameters given by *Engeln et al.* [1986] are correct.

After estimates have been obtained for centroid depth and fault width, further uncertainty in the depth extent of faulting derives from the uncertain position of the centroid with respect to the fault width. For a circular or rectangular fault in a homogeneous medium with constant slip, the depth extent of the rupture zone should be symmetric about the centroid. To the extent that these conditions fail to hold in the Earth, the centroid is probably biased toward the lower part of the fault zone, on the grounds that the contribution to seismic moment would be greater in the higher-velocity

lower reaches of the fault. If the fault width estimated by some independent means is significantly greater than twice the centroid depth (i.e., the centroid lies in the upper half of the fault zone), it is likely that one or both of these source parameters have been incorrectly determined. This is the case for the reported parameters for many of the largest events in the study by *Engeln et al.* [1986].

Transform Thermal Model

Though the thermal model for transforms adopted by *Engeln et al.* [1986] is incompletely described, some form of heat flux boundary condition is evidently imposed at the ridge axis because the isotherms do not tend to zero depth at zero age. Such a model contrasts with the simple plate cooling model of *Parsons and Sclater* [1977], which is the basis for the thermal model of transform faults employed in this study. More importantly, the *Parsons and Sclater* [1977] model was used by *Wiens and Stein* [1983, 1984] and *Bergman and Solomon* [1984] in their studies of oceanic intraplate earthquakes. Because *Engeln et al.* [1986] compared the nominal isotherm marking the deepest seismic behavior in their thermal model for transforms with the isotherm inferred by *Wiens and Stein* [1983, 1984] to limit the depth extent of oceanic intraplate earthquakes, the nominal limiting temperature for transforms was biased low in their analysis.

A minor additional difference between the study of *Engeln et al.* [1986] and this paper concerns the procedure for estimating the age offset across each tranform. They estimated age offset from transform length and present slip rate while we employed

seafloor magnetic anomalies for all but the Hayes transform. For the three transforms which are common to both studies we obtained slightly larger age offsets (22 versus 21 m.y. for the Gibbs transform, 13 versus 12 m.y. for the 15°20' transform, and 20 versus 19 m.y. for the Vema transform). Use of the same age offsets would increase slightly the discrepancies in limiting temperature between our results and those of *Engeln et al.* [1986].

Summary Assessment

There are many differences in procedure between the study of *Engeln et al.* [1986] and that of this paper. We believe that these differences account for the different results and interpretations obtained in the two studies. On the basis of a step-by-step comparison of procedures, we are confident that the centroid depths and fault widths obtained in this paper are valid measures of the depth extent of faulting on large-offset transform faults in the north Atlantic, and that these results require neither anomalous thermal structure nor anomalous mechanical properties for oceanic transform fault zones.

CONCLUSIONS

From an inversion of teleseismic long-period P and SH waveforms we have determined the centroid depths and other source parameters of 12 large earthquakes on six large-offset transform faults on the northern Mid-Atlantic Ridge. Trade offs between the centroid depth and the source time function generally limit the resolution

of centroid depth purely on the basis of misfit between synthetic and observed waveforms. By requiring the synthetic waveforms to match identified depth phases in the P waveforms, however, we are able to derive well-constrained centroid depths for many of the events studied. The best-fitting centroid depths of earthquakes on the Gibbs, Oceanographer, Hayes, Kane, and Vema transforms all lie in the range 7-10 km beneath the seafloor. For three events on the 15°20' transform, the centroid depths are 4-5 km. For seven of the earthquakes which were also studied with waveform inversion by *Engeln et al.* [1986], the centroid depths they reported are systematically shallower, by 2 to 8 km, than those determined in this paper.

For each earthquake we estimated the maximum depth of faulting from the centroid depth and the fault width. For the five largest earthquakes, we assumed that the rupture surface was rectangular and extended from the seafloor to twice the centroid depth. For the smaller events, we adopted a circular fault model, with the fault radius estimated from the duration of the source time function. The maximum depth of seismic faulting was compared with the transform thermal structure predicted by a simple model in which the temperature field on either side of the transform follows the plate cooling model and the temperature within the transform zone is given by the mean of the temperature distributions in the adjoining lithospheric blocks. With the exception of the 15°20' transform, the nominal temperature bounding the lower limit of seismic behavior in these transforms is 900° ± 100°C. By comparison, the deepest extent of rupture during oceanic intraplate earthquakes with strike-slip mechanisms corresponds to the 700° ± 100°C isotherm. The difference in limiting isotherms is attributable to the

different strain rates which characterize intraplate and transform fault deformation. The maximum depth of seismic rupture for earthquakes on the 15°20' transform appears to be limited by the nominal 600°C isotherm. This distinctive behavior may be the result of a recent episode of extension across the transform accompanying the northward migration of the North American - South American - African triple junction to the approximate position of the transform [*Roest and Collette*, 1986].

All but two of the earthquakes of this study have focal mechanisms characterized by strike-slip motion on near-vertical, transform-parallel faults. The two exceptions, both of which occurred on the western end of the Vema transform, are characterized by strike-slip faulting on fault planes dipping at 50-60° to the north. The slip vectors determined for the earthquakes in this study have an uncertainty of 3° or less and should provide reliable indicators of the local direction of relative plate motion.

For several earthquakes, the waveform data displayed evidence of sources more complex than simple strike-slip rupture. For three events on the Kane and Vema transforms secondary rupture is characterized by reverse faulting on planes with strike directions oblique to the trend of the transform. Events with significant secondary reverse faulting appear to be spatially related to compressional jogs in the trend of the active fault zone.

The source parameters we have obtained for large transform fault earthquakes do not support the conclusion of *Englen et al.* [1986] that oceanic transforms are, in general, either anomalously hotter than predicted by current models or anomalously weaker than normal oceanic lithosphere.

APPENDIX A. EARTHQUAKE SOURCE MECHANISMS FROM BODY WAVEFORM INVERSION

We present here the details of the source mechanisms, obtained from the inversion of long-period teleseismic P and SH waveforms, for the 12 transform fault earthquakes in the north Atlantic listed in Table 2. The earthquakes are grouped by transform, north to south. The convention for describing a double-couple source mechanism is that of *Aki and Richards* [1980]; the three angles are given in the order: strike/dip/slip. Centroid depths are given relative to the seafloor. In processing the waveform data for the inversions, we found a few instances in which the reported instrument gain or polarity for one or more of the long-period components at a station appears to be incorrect. When there are no waveform data from stations nearby which may be substituted for such seismograms and inclusion of the station is important for maintaining good station distribution, we have made *ad hoc* corrections to the gain (by a factor of 2) or polarity to achieve compatibility with other waveform data. All such cases are noted in the discussion of individual events.

February 13, 1967 - Gibbs (Figures 2 and A1)

A strike-slip mechanism (095/88/180) was first determined from P wave first motions for this event by *Solomon* [1973]. *Kanamori and Stewart* [1976] made an extensive study of this earthquake using surface and body waves; they confirmed the mechanism of *Solomon* [1973] and estimated the seismic moment to be 3.4 x 10^{26} dyn

cm from the surface wave excitation and about 2 x 10^{26} dyn cm from the SH wave amplitudes. The centroid depth was not independently determined by these investigators but was assumed to be 11 km for the surface wave study and 6 km for the body wave modeling. By matching synthetic and observed SH waveforms they estimated the source time function (STF) to be well-approximated by a trapezoid with a total duration of 17 s and a rise time of 7 s. *Kanamori and Stewart* [1976] found no evidence for source directivity for this event. From body waveform modeling and Rayleigh wave spectral amplitudes *Engeln et al.* [1986] determined a similar mechanism of 094/86/180, a seismic moment of 4.6 x 10^{26} dyn cm, a centroid depth of 7 km, and an STF duration of 11 s.

The station coverage and S/N ratios of the body waveform data for this earthquake are excellent. Many of the P waveform data contain a small pulse several seconds before the primary motion (e.g., ATU, TRN, SJG, COL). A small precursory pulse may also be seen on some of the SH waveform data (e.g., TRN, ATL, LON, COL). These pulses on the long-period records are clearly associated with a small early arrival on the short-period P seismograms [*Kanamori and Stewart*, 1976]; in most cases this precursor was picked as the first arrival reported to the ISC. The delay between the precursor and mainshock is larger (~5 s) at stations to the west, which indicates that the precursor occurred to the west of the mainshock. In our source study of this earthquake we used two subevents. The source parameters of the first subevent (precursor) were fixed in the inversion: centroid depth = 10 km, mechanism = 095/90/180, M_0 = 7 x 10^{24}

dyn cm, triangular STF 3 s in duration. The beginning of the inversion window for each long-period P waveform was fixed at the arrival time of the short-period P waveform of the precursor at that station. The delay and location of the centroid of the second subevent (mainshock) relative to the precursor were then included as unknown parameters in the waveform inversion. Because of the small size of the precursor compared with the mainshock, the precursor's source parameters have almost no effect on the inversion and we have therefore not included them in Table 2. The crustal structure assumed for the inversion contains a sediment layer 0.5 km in thickness [*Searle*, 1981]. The polarity of the SH waveform at LON was found to be reversed.

Test inversions with different starting models confirm that the epicenter of the mainshock was east of the precursor. In the better solutions, the centroid of the mainshock lies from 15 to 20 km east of the precursor and occurs 5-6 s later. This result suggests that the mainshock initiated near the focus of the precursor and ruptured toward the east. This sense of source directivity is also supported by the waveform data.

In our standard procedure, a value of 4 s is assumed for the attenuation parameter for SH waves (t^*_{SH}) at all stations. *Dziewonski and Anderson* [1981], among others, have suggested that t^*_{SH} might be distance-dependent, with higher values at larger epicentral distances. Because many of the SH waveform data at stations to the east for this event are at large epicentral distances compared with those to the west, we investigated the effect on the estimated source parameters of a distance-dependent

t^*_{SH}. With the relation of *Dziewonski and Anderson* [1981], values of t^*_{SH} range from 4.1 to 5.7 s for the stations used in our study. Utilizing these values in the inversion, which continued to indicate unilateral rupture toward the east, the residual variance decreased by 1.5% of the data variance (marginally significant), primarily because the average amplitude of the synthetic SH waves is reduced somewhat by the higher average value of t^*_{SH}, and the P waveforms are better fit by the higher value of M_0 (1.9 versus 1.8 x 10^{26} dyn cm) required to match the observed waveforms. To maintain consistency with our other source solutions, however, the solution given in Table 2 is that obtained with constant t^*_{SH} (4 s).

Because of the large size of the mainshock, no clear depth phases are evident in the waveforms and the resolution of centroid depth is poor. We fixed the centroid at various depths between 1 and 19 km below the seafloor and found a broad minimum in residual variance centered at a centroid depth of about 10 km (Figure 10). A second minimum exists at very shallow depth (1-2 km), but we consider such a solution unlikely for an event this large. Our preferred solution has a centroid depth of 10 km, a mechanism of 098/84/183, a moment of 1.8 x 10^{26} dyn cm, and an STF about 12 s in duration. This value for the moment is similar to that obtained by *Kanamori and Stewart* [1976] from SH waveform modeling, but as indicated by their surface wave study, it underestimates the total moment released by this earthquake. Though *Engeln et al.* [1986] do not describe in detail their procedure for estimating moment, we presume that the larger value they reported for this event was obtained from Rayleigh

wave amplitudes. The strike of the fault plane determined in our waveform inversion is tightly constrained by the many near-nodal SH waves. The non-vertical dip angle is indicated by the near-nodal P waveform data, but a vertical dip for the fault plane cannot be rejected with high confidence. The STF has a secondary peak which may indicate that the rupture occurred as several discrete pulses; while the P waveforms are consistent with such a view, we did not attempt to resolve such complexities further. Many of the P waveform data also have large oscillations late in the waveform which appear to be water reverberations. Such reverberations may have been excited by a small amount of dip-slip motion at shallow depths.

October 16, 1974 - Gibbs (Figures 2 and A2)

This earthquake was studied by *Kanamori and Stewart* [1976] using both surface waves and SH waves. They assumed that the focal mechanism was identical to that for the 1967 Gibbs event. In contrast to the results for the 1967 earthquake, the surface waves (4.5×10^{26} dyn cm) and body waves ($\sim 5 \times 10^{26}$ dyn cm) yielded similar estimates of seismic moment. By matching the SH waveforms they estimated that the STF is trapezoidal in shape, with a rise time of 10 s and a total duration of 22 s. Kanamori and Stewart noted that this duration is more consistent with the length of the aftershock zone (~80 km, on the basis on 4 aftershocks) if the rupture occurred bilaterally. *Engeln et al.* [1986] reported a mechanism of 102/88/182 and a centroid depth of 4 km. Their estimate of seismic moment (5.0×10^{26} dyn cm) agreed with that from the earlier study, but their STF duration was only 11 s in duration, half that

estimated by *Kanamori and Stewart* [1976].

The P waveform data are well distributed and the S/N ratios are excellent. The S waves on many horizontal component seismograms are clipped, too faint to digitize, or obscured by surface waves on later traces; the SH waveform data available for the inversion study are therefore fewer in number and less well-distributed than those for the 1967 earthquake. This earthquake had a small precursor, very similar to that for the 1967 Gibbs event [*Kanamori and Stewart*, 1976]. We employed a very small precursory subevent (centroid depth = 8 km, mechanism = 070/45/130, $M_0 = 4 \times 10^{24}$ dyn cm, STF = 2 s in duration) in the source model so that we could locate the centroid of the main event with respect to the precursor, which was the event located by the ISC. As for the 1967 event, the adopted crustal structure contains a sediment layer 0.5 km in thickness. The polarity of both the P and SH waveforms at BDF were found to be reversed.

A primary constraint on fault strike for the main subevent comes from the near-nodal SH waveforms at SJG and BHP. With the assumption that the SH nodal line lies between these two stations, the fault strike lies in the range 96°-104°. Waveform inversion confirms this result, consistently converging to solutions with a strike near 98°. The P waveform data, particularly at AAE, which lies nearly along the strike of the fault plane but which displays a clear compressional first motion, constrain the fault plane to be slightly non-vertical with a dip to the south, similar to the mechanism found for the 1967 earthquake. Waveform inversion indicates that the

centroid of the main subevent was located west of the precursor, by as much as 30 km. Curiously, the long-period body waves indicate that the main rupture propagated primarily from west to east, in the direction toward the epicenter of the precursor.

Many of the P waveforms have a double-peaked character which could be interpreted as the delay between direct and surface-reflected phases. A centroid depth of about 17 km for the main subevent is indicated if the waveforms are matched by a single pulse (of about 13 s duration), but the fit to all the waveform data is improved with a shallower centroid depth and a longer, more complicated STF, or with a multiple-source model with additional subevents (see below). This earthquake may be a case in which rupture complexities mimic depth phases, but we are unable to exclude the deeper solution with high confidence. Our preferred solution for this event has a centroid depth of 10 km, which is near the middle of the range of depths over which acceptable solutions may be obtained. SH waveforms at JCT, GSC, and COR have exceptionally elongated waveforms compared with those at other stations, particularly EIL. Even with the assumption of unilateral rupture toward the east we had difficulty reproducing the full extent of this asymmetry. The seismic moment at a centroid depth of 10 km is 3.2×10^{26} dyn cm. Matching the SH waveforms alone yielded higher estimates of the moment, comparable to those reported by *Kanamori and Stewart* [1976] and *Engeln et al.* [1986]. The STF is at least 15 s in duration. The mechanism at this centroid depth is 098/87/178. Several near-nodal P waveforms are poorly fit with this mechanism, but such problems are expected to be more pronounced for larger earthquakes, which are more likely than smaller events to involve non-planar fault

surfaces.

We also tested multiple-source models with additional later subevents for this earthquake, the most successful of which featured a secondary subevent with a reverse-faulting mechanism late in the rupture of the main strike-slip event. Such secondary faulting is not unreasonable for an event this large. We obtained substantial reductions in residual variance with several models of this type, primarily through improvements in the fit to the P waves. The parameters of this secondary rupture are poorly constrained, however, and we do not include such a secondary subevent in the source model in Figure A2 and Table 2.

May 17, 1964 - Oceanographer (Figures 3 and A3)

From P wave first motions *Sykes* [1967] obtained a strike-slip focal mechanism (266/84/344) with a strike direction deviating considerably from that of the transform (approximately 285°). *Wyss* [1970] reported a seismic moment of 1.7×10^{25} dyn cm from a surface wave amplitude measurement. *Weidner and Aki* [1973] investigated this event with a technique employing surface waves from pairs of events with differing mechanisms to remove common path effects; they determined a strike-slip mechanism (271/84/014), a seismic moment of 1.9×10^{25} dyn cm, and a centroid depth of 6 ± 3 km.

The station coverage and S/N ratios of the body waveform data are very good. The strike of the focal mechanism is constrained by the nodal SH waveform at CAR. In trial inversions, several stations with large amplitude anomalies were encountered. For the purpose of normalizing the observed waveform data to a common instrument gain, the

reported gains of the following stations were changed: DAL (SH) from 1500 to 3000, AAE (SH) from 375 to 750, and TOL (P) from 1500 to 3000. The amplitude anomaly at TOL may be due not to miscalibration or misreporting of the true gain, but rather to the short epicentral distance of this station (25°), for which the geometric spreading correction is quite uncertain.

The P waveforms at stations in the western hemisphere have a clear expression of a double peak in the first half cycle of motion which we interpret as due to the separation between the P and sP phases. P waveforms to the northeast all have an emergent character, which could be duplicated in the synthetics only by assuming that rupture propagated unilaterally from east to west. The separation of the two peaks in the P waveforms at stations to the northwest is consistent with a centroid depth of about 9 km, while the P waveforms at stations to the southwest are better fit with a depth of about 11 km. The residual variance is effectively constant for centroid depths between 6 and 12 km. We give the solution at 9 km centroid depth in Table 2. The mechanism (280/89/001) and seismic moment (2.6×10^{25} dyn cm) are stable with respect to variations in centroid depth in the range investigated.

On June 6, 1982, an earthquake occurred on the Oceanographer transform with an epicenter about 10 km to the east of that of the 1964 event. Because of its small body wave magnitude (5.2), the 1982 earthquake was not included in this study. A centroid moment tensor solution by *Dziewonski et al.* [1983] indicates that the mechanisms (105/69/012) and moment (3.6×10^{25} dyn cm) are comparable to those of the 1964

earthquake.

March 28, 1976 - Hayes (Figures 4 and A4)

On the basis of P wave first motions, *Engeln et al.* [1986] reported a strike-slip mechanism (271/88/000). This earthquake was not among those for which they modeled waveforms.

The P waveform data are somewhat noisy, but virtually every record displays the characteristic double peak in the first half-cycle which we interpret as the delay between direct and surface-reflected phases. The SH waveform data are very good; the strike of the focal mechanism is well constrained by near-nodal waveforms at STU, TRI, and SJG. Because of the short STF, the clear presence of depth phases on P waveforms in 3 quadrants of the focal mechanism, and the better response at short periods of WWSSN instruments after 1965, the centroid depth for this earthquake is among the better constrained values in this study (Figure 10). The delay between direct and surface-reflected phases on the P waveforms can be adequately matched by synthetic waveforms only for centroid depths between about 7.5 and 9.5 km below the seafloor. Our preferred solution has a centroid depth of 9 km, a mechanism of 281/85/002, and a seismic moment of 8.4×10^{24} dyn cm. A dip angle constrained at 90° does not seriously affect the residual variance, but the data are consistently better fit with a fault plane which dips slightly to the north.

May 19, 1963 - Kane (Figures 5 and A5)

From P wave first motions for this event, *Sykes* [1967] determined a strike-slip mechanism (103/90/183) on a fault striking ~5° more clockwise than the average trend of the transform. *Wyss* [1970] reported the seismic moment to be 2.6 x 10^{26} dyn cm from a surface wave amplitude measurement.

The available WWSSN records, while few in number, have excellent S/N ratios. Among the SH waveform data only ATU is near-nodal, however, and few of the P waveforms are near a nodal plane; the focal mechanism is therefore less well constrained than those of most other events in this study. The P waveforms from this event, particularly those recorded in Europe (COP, ATU), are remarkably impulsive. We take the strong contrast between the records at these stations and those from North America (GOL, AAM, CMC) as evidence that rupture propagated from west to east; our source model incorporates this sense of directivity in the source time function

P waveforms at the European stations and, to a lesser extent, the South American stations display a double-peaked character which we interpret as the result of the delay between direct and surface-reflected phases. With this interpretation, the centroid depth is constrained to be about 7 km. The focal mechanism is characterized by strike-slip motion (099/83/175) on a fault surface parallel to the average trend of the transform. The seismic moment is 5.2 x 10^{25} dyn cm, considerably smaller than the value reported by *Wyss* [1970].

The SH waveforms are well-matched by a strike-slip source model as described above, but the fit to the P waveforms is rather poor, particularly for the later parts of the

waveforms. A significantly better fit to the observed waveforms, with a decrease in the residual variance from 25% to 18%, is obtained if the source model includes a second episode of rupture, characterized by reverse faulting on a fault plane trending oblique to the strike of the transform. In our preferred model, the reverse-faulting subevent (048/44/098) is delayed by ~4.5 s and is located ~20 km to the east of the strike-slip subevent; the moment is 1.7×10^{25} dyn cm and the centroid depth is 6 km, similar to that of the strike-slip subevent. None of the source parameters of the reverse-faulting subevent are well-resolved.

March 26, 1980 - Kane (Figures 5 and A6)

Giardini et al. [1985] reported a centroid-moment tensor for this event from an inversion of long-period waveforms from the Global Digital Seismic Network (GDSN) and the International Deployment of Accelerometers (IDA) network. They obtained a strike-slip mechanism (282/66/170) with a fault plane dipping to the north at a significantly non-vertical angle and a moment of 5.3×10^{25} dyn cm.

The body waveform S/N ratios and station distribution are unusually good, and there is excellent coherence between waveforms from stations near one another on the focal sphere. For the purpose of normalizing the observed waveform data to a common instrument gain, the reported gain of LPS (P) was changed from 1500 to 3000. The mechanism is tightly constrained by near-nodal P waves at four azimuths (GDH, KBS, WIN, LPA, JCT) and by the change in polarity of SH wave first motion between STU and ATU. The SH waveform at COL is also near-nodal. Despite these favorable

factors, the detailed source parameters of this event are difficult to resolve because a significant component of dip-slip motion accompanied the strike-slip rupture. The existence of the dip-slip component is strongly suggested by the prominent water reverberations on many P waveforms and by the strong compressional first motion at NAI, which must be close to a nodal line for the strike-slip mechanism. The P wave at PRE (not used in the inversion) and WIN also show compressional first motions in the dilatational quadrant of the strike-slip focal mechanism. It is not possible to perturb the strike-slip mechanism to accommodate these waveforms without introducing severe misfits at other stations.

In attempting to disentangle the two episodes of rupture involved in this earthquake we took advantage of the distinct differences between the body waveforms produced by strike-slip and shallow dip-slip earthquakes. The observed SH waveforms are almost completely due to the strike-slip component of rupture; they constrain the focal mechanism and seismic moment but are very insensitive to the STF or centroid depth. Except for the large water reverberations later in the waveform, the P waveforms at stations well removed from the nodal planes of the strike-slip mechanism (e.g., NUR, MAL, NNA, LPS, WES) are very typical of waveforms from other earthquakes in this study. In forward modeling trials we found that these non-nodal P waveforms and all of the SH waveforms could be well matched with the expected strike-slip focal mechanism (098/90/180), a centroid depth of 8 km, a moment of 5×10^{25} dyn cm, and an STF about 4 s in duration. We suspect that the *non-vertical* dip angle in the solution reported by *Giardini et al.* [1985] resulted from attempting to describe, with a single

moment tensor, an earthquake consisting of two subevents with significantly different focal mechanisms.

To investigate the dip-slip component of rupture, we performed forward modeling trials and inversions of the P waveforms which are near-nodal for the strike-slip mechanism (GDH, KBS, NAI, LPA, and JCT). Our ability to resolve the details of this dip-slip component is compromised by the small number of stations used, the lack of SH waveform data, and the fact that there must be some contribution to these waveforms from the strike-slip event. Nevertheless, we feel the following characterization may be made with some confidence: the secondary dip-slip rupture associated with this earthquake involved thrust faulting at shallow (crustal) depth, on a fault plane striking to the northeast, and having a total moment release in the range 0.7 - 1.4 x 10^{25} dyn cm. When multiple-element source time functions were used in the inversions, the STF consisted of several small pulses spanning a total duration of about 6 s, but to remove instabilities in the inversion we fixed the STF as a single trapezoidal element with a length of 4 s for most of the inversions. The shallow centroid depth is required in order to produce sufficiently large water reverberations, and a shorter STF degrades the fit significantly. The reverse-faulting subevent thus appears to have involved rupture with a distinctly low average stress drop, a result consistent with rupture in the shallow portion of the crust.

We performed a series of inversions with the entire set of waveform data to refine the source parameters of the two subevents and to investigate their spatial and temporal relationships. The centroid depth of the thrust faulting subevent was held

fixed at 4 km below the seafloor, while the remaining source parameters were left as free parameters. The final mechanism for the thrust faulting subevent was 033/38/084, with large uncertainties in all components, especially the strike and slip angles. The seismic moment is 1.0 x 10^{25} dyn cm. The time delay is 2.5 s and the centroid of this subevent is located 7 km east of the centroid of the strike-slip subevent, although solutions in which the time delay and separation are even less than these values are equally acceptable. The mechanism of the strike-slip subevent is 100/86/179, with somewhat greater uncertainty than usual due to the interference from the thrust faulting subevent. The fit to the waveforms is improved if unilateral rupture to the east is assumed. The seismic moment is 4.4 x 10^{25} dyn cm, in good agreement with the moment reported by *Giardini et al.* [1985]. The centroid depth of the strike-slip subevent is well constrained at about 8 km below the seafloor, with an uncertainty of about 2 km. The addition of the thrust faulting subevent to the source model reduces the residual variance from 26% to 15% of the data variance.

The strike-slip component of rupture for this earthquake appears to be very similar to the other events in this study. At some point in the upper half of the rupture surface, however, the strike-slip motion was apparently impeded by one or more obstacles, resulting in a sequence of small thrust faulting events or possibly a single rupture with very low stress drop. The thrust faulting could have occurred at one end of the strike-slip rupture zone (perhaps stopping it) or at shallow depth along the same segment of the transform which ruptured in the strike-slip subevent.

September 24, 1969 - 15°20' (Figures 6 and A7)

This event was among those studied by *Engeln et al.* [1986], but in a table and figure these authors mistakenly give the epicenter of a much smaller (m_b 5.3) earthquake which occurred on the Gibbs transform 14 hours earlier on the same day. *Engeln et al.* [1986] report a strike-slip mechanism (103/89/181), a moment of 1.2 x 10^{26} dyn cm, a centroid depth of 3 km, and an STF 9 s in duration.

The body waveform data display excellent station distribution and S/N ratios for both P and SH waves. For the purpose of normalizing the observed waveform data to a common instrument gain, the reported gain of PTO (P) was changed from 1500 to 3000. Unusually tight constraints on the focal mechanism result from having nodal SH waves at three azimuths: ATU, ARE, and WES. The waveforms are quite simple in appearance; there is no evidence for multiple rupture (e.g., as with the 1980 Kane earthquake) or an anomalous mechanism (e.g., the Vema earthquakes of 1962 and 1976; see below). Despite these favorable circumstances, the strongest constraint that can be placed on the centroid depth with the body waveform data is that it is less than about 10 km below the seafloor. We performed inversions with the depth fixed at 1 km intervals between 2.5 and 10.5 km below the seafloor. The residual variance for solutions to a depth of 9.5 km varied by only 0.5% of the data variance. In this range there are two minima: a sharp one at a depth of 8.5 km and a broad one between 0 and 6 km depth. Solutions within the crust (centroid depth $\leq$ 4.8 km) have nearly pure strike-slip mechanisms (e.g., 098/89/181 at a depth of 3.5 km) while those in the upper

mantle deviate slightly from vertical strike-slip faulting, with dip angles of 75-82° to the south and slip angles of 165-177°. We prefer a solution with a centroid near the crust-mantle boundary (~ 5.0 km) because the mechanism is closer to pure strike-slip and because this depth is near the midpoint of the depth range over which the minimum error is achieved. Another reason for preferring a shallower solution is that, at depths of 8-10 km, the synthetic P waveforms begin to develop a double-peaked character which is not evident in the observed waveforms. Over the full range of depths tested, the strike of the fault plane varied only between 96° and 98° and the seismic moment varied between 8.8 and 9.8 x 10^{25} dyn cm. For all solutions the waveform data are better matched if we assume that rupture occurred unilaterally from west to east.

June 19, 1970 - 15°20' (Figures 6 and A8)

Weidner and Aki [1973] studied the surface waves from this earthquake with the same paired-event technique that they used on the Oceanographer transform earthquake of May 17, 1964. They found a strike-slip mechanism (097/70/177), a moment of 1.0 x 10^{25} dyn cm, and a centroid depth of 6 ± 3 km. *Engeln et al.* [1986] report a mechanism of 095/84/179, a moment of 2.1 x 10^{25} dyn cm, a centroid depth of 3 km, and an STF 6 s in duration.

Station coverage and S/N ratios for this earthquake are quite good; as with the 1969 event on this transform, nodal SH waves were recorded at three azimuths (MAL, ARE, NNA, and AAM). A number of the P waveforms show a double-peaked form which we take to represent the distinct pulses of the direct P and sP phases (PTO, MAL,

LPB, SHA, AAM). We performed inversions with the centroid depth fixed at various depths between 3.5 and 7.5 km below the seafloor. At 3.5 km, the depth phases in the P waves cannot be matched with a simple STF; at 7.5 km, the separation of the depth phases is clearly too large. Our preferred centroid depth for this event is 5 km, with an uncertainty of no more than 2 km. The mechanism is well constrained (097/89/179), the STF is 3 s in duration, and the seismic moment is 1.2×10^{25} dyn cm, similar to that obtained by *Weidner and Aki* [1973].

December 9, 1972 - 15°20' (Figures 6 and A9)

Engeln et al. [1986] conducted body waveform modeling for this event. They reported a mechanism (100/89/180) but not a seismic moment or an STF duration. They suggested a centroid depth of 2 km but noted that this value was "less well constrained."

The station distribution and S/N ratios of the SH waveform data are excellent, but the P waveform data are largely confined to stations in the western hemisphere and there is some noise on the seismograms at North American stations. We found an unusually large number of amplitude anomalies in the waveform data for this event; instrument gains were changed for the P waveforms at HLW (from 3000 to 6000) and LPB (from 1500 to 3000) and for the SH waveforms at LPA (from 750 to 375) and BHP (from 750 to 375). In addition, the horizontal component records from BHP were found to have reversed polarity. All the P waveforms in the northern hemisphere have a double peak in the first half-cycle which we take to be due to the separation of direct

and surface-reflected phases, but the P waveforms at South American stations have only a single broad peak. At any centroid depth less than about 6 km, the residual variance is effectively constant. Our preferred solution has a centroid depth of 4 km. At depths shallower or deeper than this value by more than about 1 km, the synthetic waveforms violate either the apparent depth phases in the north or the lack of depth phases in the south. The mechanism, virtually identical to those of the other two events on this transform, is characterized by nearly pure strike-slip motion (097/89/178), and the seismic moment is 8.7×10^{24} dyn cm.

March 17, 1962 - Vema (Figures 7 and A10)

The only previous source study of this event was a P wave first-motion study by *Sykes* [1967], who reported a strike-slip focal mechansm (270/86/174). The body waveforms are quite simple in appearance and the S/N ratios are very good. Because the S waves are clipped or faint on many of the horizontal component records of this large event, SH waveforms were obtained at only two stations, but the azimuthal distribution of P waveform data is good. The P waveform at BHP was found to have reversed polarity. Qualitatively, the first motions of the P waveforms appear to be inconsistent with the expected focal mechanism (i.e., right-lateral strike-slip on a vertical fault trending E-W): at all three stations in the northwest quadrant the first motion is compressional, while IST in the northeast quadrant has a dilatational first motion. The short-period P waveforms generally confirm these anomalous first motions.

The source region velocity structure assumed in the inversion study includes a sediment layer 0.5 km thick [*Rowlett and Forsyth*, 1984]. Trial inversions confirmed the anomalous nature of the focal mechanism (276/58/187). The 1976 Vema earthquake has a nearly identical mechanism (see below). No other earthquake in this study has a mechanism in which the fault plane departs so substantially from the vertical. For centroid depths in the range 7-13 km below the seafloor the residual variance is nearly constant and unusually low (~10% of the data variance). The residual variance increases significantly above this minimum only at depths shallower than 4 km or greater than 15 km. The lowest residual variance was found at a centroid depth of 12 km, but we take 10 km (the mid-point of the depth range with essentially constant residual variance) as the best estimate of the centroid depth for this event. The seismic moment is 3.1 x 10^{26} dyn cm. No source directivity is evident in the P waveforms. A prime factor in the low residual variance achieved for this event is the scarcity of SH waveform data; the average amplitude of P and SH waveform data are usually slightly inconsistent, requiring a compromise (when there are approximately equal numbers of both data types) which often contributes as much as 10% to the residual variance.

May 14, 1976 - Vema (Figures 7 and A11)

Engeln et al. [1986] reported first motions and waveform modeling results for this earthquake. They considered this event anomalous on the basis of its focal mechanism (279/61/165), which is characterized by a fault plane dipping to the north at an angle departing significantly from the vertical. They also reported an extremely

shallow, but "less well constrained," centroid depth of 1 km, a seismic moment of 1.5 x 10^{25} dyn cm, and an STF 7 s in duration.

The P waveforms have the same distinctive characteristics of the much larger 1962 event, which occurred about 45 km to the east, characteristics which require a fault plane dipping to the north at a significantly non-vertical angle, in agreement with the findings of *Engeln et al.* [1986]. For this earthquake, the clear dilatations at EIL and HLW and the large, impulsive, compressional motion at BHP are the most obvious evidence for non-vertical dip. Other P waveform data lying between BHP and BEC on the focal sphere, but not used in the inversion study, also show clearly compressional first motions. The dip angle is not well resolved, however, because it depends strongly on the seismic velocities at the centroid depth, and the range of acceptable centroid depths includes both the lower crust and upper mantle. For a centroid in the lower crust a dip angle of 60° is required; the dip angle for mantle solutions is shallower, ranging from 41° for a centroid immediately beneath the crust to 55° at a depth of 13 km below the seafloor. For the purpose of normalizing the observed waveform data to a common instrument gain, the reported gains of the P and SH waveforms at LPB were changed from 1500 to 3000.

Depth resolution for this event is quite poor, because so many of the P waveform data lie near a nodal line. We fixed the centroid at a variety of depths between 2 and 13 km below the seafloor. The curve of residual variance versus depth is quite flat in this range, with a total range in residual variance of only 2% of data variance. The depth range of acceptable solutions is judged to be 5-12 km, with a minimum misfit at a

depth of 9 km. This solution, given in Table 2, has a mechanism of 269/49/175 and a moment of 1.0 x 10^{25} dyn cm.

August 25, 1979 - Vema (Figures 8 and A12)

From a centroid-moment tensor inversion of GDSN and IDA waveform data, *Giardini et al.* [1985] obtained a strike-slip mechanism (271/78/167) and a seismic moment of 1.6 x 10^{26} dyn cm for this earthquake. Guided apparently by P wave first motions, *Engeln et al.* [1986] reported that body waveform inversion indicates a thrust-faulting mechanism (051/48/085) for this event. They reported a centroid depth of 1 km but acknowledged that this value is not well constrained. Engeln and coworkers also reported a seismic moment of 8.1 x 10^{25} dyn cm and an STF 10 s in duration.

The waveform data are excellent, with very good S/N ratios and station coverage for both P and SH waves. The polarity of the SH waveform at DAG was found to be reversed. The complexity of the rupture history in this earthquake is clearly revealed in the multiple pulses on the P waveforms recorded in Europe and the Middle East (e.g., KEV, PDA, TOL, JER). Our analysis of the waveform data for this event indicates that the main rupture in this earthquake occurred with a strike-slip motion consistent with the geometry of the transform and with the mechanism obtained by *Giardini et al.* [1985], but this faulting was preceded by a small thrust-faulting subevent with a mechanism similar to that inferred by *Engeln et al.* [1986] in their model for the entire earthquake. A strike-slip mechanism for the precursory subevent is ruled out by the

compresional first motions seen at stations in North America (e.g., GOL, WES). A small pulse from the precursor can also be seen on some of the SH waves (e.g., GDH, DAG, BUL). A strike-slip earthquake can be distinguished from a thrust-faulting event quite easily by noting the average amplitude of the SH waveforms relative to the P waveforms: a strike-slip mechanism produces SH waveforms 3-5 times larger than the P waveforms, while a thrust mechanism produces P and SH waves of comparable amplitude. By this criterion the 1979 Vema earthquake is clearly dominated by strike-slip motion, despite the pattern of first motion polarities.

Other than the approximate mechanism and seismic moment, the source parameters of the precursory subevent are poorly resolved. We fixed all parameters for this subevent in the inversion, solving for the source parameters of the main strike-slip subevent and the time delay and distance between the two subevents. The parameters assumed for the precursor are 070/70/120, $M_0 = 7.5 \times 10^{24}$ dyn cm, and h = 13 km. The surprisingly great depth is required so that the surface-reflected phases are sufficiently delayed so as to arrive after the initial motion from the subsequent strike-slip subevent, which occurred 4-5 s later. Extensive trials failed to reveal a satisfactory shallow solution for the precursor. The epicentroid of the larger strike-slip subevent has a location within a few kilometers of that of the precursor, but the centroid depth (7 km) is shallower. The fault strike indicated by the mechanism (087/89/172) of the main subevent differs by about 10° (counterclockwise) from the average trend of the transform, but this strike is nearly parallel to the trend of the PTDZ in the epicentral

region to the east of the Vema Mound (Figure 8). The strike is constrained by the change in polarity between the SH waveforms at NUR and ATU and by the nodal SH waveforms at GOL and MSO. The seismic moment we obtain is 1.2×10^{26} dyn cm, more than an order of magnitude greater than that of the precursor, and similar to the value determined by *Giardini et al.* [1985]. The STF for the main event is 10 s in duration. The waveform data favor a source model with unilateral rutpure from west to east.

It has commonly been inferred that large earthquakes initiate near the bottom of their rupture zone [e.g., *Das and Scholz*, 1983]. The inversion results for this earthquake suggest that the lower part of the fault zone may have been locked by a geometrical barrier, possibly related to the deep structure of the Vema Mound. The extremely impulsive character of the precursor is consistent with a high stress-drop event on the deeper, stronger portion of the fault. Strike-slip rupture on the shallower portions of the fault ensued after a delay of several seconds, with rupture propagating primarily to the east, away from the barrier.

APPENDIX B. DERIVED SOURCE PARAMETERS

From the source parameters estimated directly in the waveform inversion studies (Table 2), several other parameters of tectonic importance may be derived. These include fault dimensions, average stress drop, and average slip. To estimate these quantities we must adopt a source geometry. We approximate the rupture surface either as a circle or as a rectangle with a fault length significantly greater than the fault width. In the latter case, a choice between bilateral and unilateral rupture must also be made. We make use of a relationship, derived by *Ebel et al.* [1978], between the total duration T of the source time function (STF) and the radius a of an equivalent circular fault with constant stress drop, embedded in a whole space,

$$a = \frac{28 \pi V_s T}{64 + 7 \pi (5 + 4 \sin \delta)} \qquad \text{(B1)}$$

where V_s is the shear wave velocity and δ is the angle between the departing sP ray and the normal to the fault. The simplicity of the expression in (B1) reflects the idealized nature of the fault model on which it is based. The angle δ generally falls in the range 60°-70°, so sin δ is ~0.9. With a value for V_s appropriate to the mantle (4.6 km/s), this relation reduces to a = 1.6 T, with T in seconds and a in kilometers. Clearly, the fault radii calculated with this expression will bear, at best, only a loose relationship to the actual rupture dimensions, but the relation provides a convenient criterion for

estimating the transition between an approximately equidimensional fault and one with an aspect ratio (length/width) significantly greater than 1.

Fault radii for the transform earthquakes were calculated with (B1) and the STF durations in Table 2. The rupture surfaces of those earthquakes for which the calculated radius is similar to or less than the centroid depth will be approximated by circular faults. Values of fault radius for these events are given in Table 4. Only one event, the 1976 Hayes earthquake, has a calculated radius significantly less than its centroid depth. Since we believe that this centroid depth is well resolved, we speculate that the upper portion of the fault failed under such a low stress that it made little contribution to the teleseismic signal. We regard the alternative explanation, that rupture did not extend to the seafloor, as less plausible.

For the five largest events, the calculated radius is significantly greater than the centroid depth. These events are best described with a rectangular fault model. For the rupture surface of these events we assume that the fault width w is equal to twice the centroid depth. If the moment release during these earthquakes is concentrated in the lower part of the fault zone, doubling the centroid depth will yield an overestimate of the fault width, leading to an underestimate of stress drop and fault slip. Fault length L is estimated from

$$L = k v_r t_c \qquad \text{(B2)}$$

where k = 1 for unilateral rupture and 2 for bilateral faulting, v_r is the rupture velocity

(taken to be 3.5 km/s), and t_c is the rupture time. Rupture time is found by subtracting the rise time from T; rise time is taken as the time interval between the beginning of the STF and the point at which the amplitudes of successive elements of the STF cease to increase. Inferred rupture and rise times are given for all events in Table 4.

We observed evidence of directivity in the waveforms for four of the five earthquakes with 'rectangular' rupture surfaces; we assumed unilateral rupture propagation in these cases. Assumption of bilateral rupture will halve the estimates of average slip and stress drop. In the absence of clear evidence for directivity, a bilateral rupture model was used for the 1962 Vema earthquake. The longer free period of the WWSSN seismometers in 1962 (30 s versus 15 s after 1965) and the small number of observed waveforms (especially SH waves) precluded a clear test for directivity for this event. We observed evidence of directivity in the waveforms from the 1964 Oceanographer event and both of the earthquakes on the Kane transform, but the source time functions suggest that the length and width of the faults are approximately equal for these events. We therefore modeled these three earthquakes with circular faults.

In no case do we consider the evidence for unilateral rupture to be compelling. The fact that the preferred direction of rupture was toward the east in six of the seven cases in which we observed directivity suggests that factors other than the rupture processes of the earthquakes may be important. A possible alternative explanation is that the greater pulse widths observed in waveforms to the west are caused by higher

average attenuation along wave paths to these stations than to stations to the east. There is abundant evidence for higher attenuation in the upper mantle beneath the western United States, where many of the stations used in our source studies are located. Because the issue of source directivity is peripheral to this study, we have not conducted a detailed investigation of the possible role of path-dependent attenuation in biasing the inferences on rupture direction.

The stress drop $\Delta\sigma$ is determined from

$$\Delta\sigma = \frac{2\,M_0}{\pi\,w^2\,L} \qquad \text{(B3)}$$

for rectangular faults or

$$\Delta\sigma = \frac{7\,M_0}{16\,a^3} \qquad \text{(B4)}$$

for circular faults [*Kanamori and Anderson*, 1975]. The average fault slip u is given by

$$u = \frac{M_0}{\mu S} \qquad \text{(B5)}$$

where S is the fault area and μ is the rigidity. We assume a value for μ of 5×10^{11} dyn/cm^2, an average of the values appropriate for crustal and mantle materials. The

derived values for stress drop and slip are summarized in Table 4. Given the uncertainty in these estimates (at least a factor of two for all parameters), the values obtained are typical of those found for moderate-size earthquakes in a variety of tectonic settings: average fault slip of 15-90 cm and average stress drop of 10-75 bars. As expected, average slip increases with seismic moment. Although there is considerable scatter, average stress drop tends to decrease with increasing moment. This result is consistent with models of rupture in which the rupture area of larger earthquakes includes more regions of low strength or low stress.

Acknowledgements. We thank Bob Detrick for providing Sea Beam bathymetry for the Kane transform prior to publication, Roger Searle for providing an unpublished interpretation of GLORIA data from the Hayes transform, and John Goff and Seth Stein for helpful discussions. Jean Kahl assisted in drafting figures. This research was supported by the National Science Foundation under grants EAR-8416192 and EAR-8617967 and by the National Aeronautics and Space Administration under contract NAS 5-27339 and grant NAG 5-814.

REFERENCES

Aki, K., and P. G. Richards, *Quantitative Seismology: Theory and Methods*, vol. 1, p. 114, W. H. Freeman, San Francisco, Calif., 1980.

Ambos, E. L., and D. M. Hussong, Oceanographer transform fault structure compared to that of surrounding oceanic crust: Results from seismic refraction data analysis, *J. Geodynamics, 5*, 79-102, 1986.

Ben-Menahem, A., Radiation of seismic body waves from a finite moving source in the Earth, *J. Geophys. Res., 67*, 345-350, 1962.

Bergman, E. A., Intraplate earthquakes and the state of stress in oceanic lithosphere, *Tectonophysics, 132*, 1-35, 1987.

Bergman, E. A., and S. C. Solomon, Source mechanisms of earthquakes near mid-ocean ridges from body waveform inversion: Implications for the early evolution of oceanic lithosphere, *J. Geophys. Res., 89*, 11415-11441, 1984.

Bergman, E. A., and S. C. Solomon, Earthquake source mechanisms from body-waveform inversion and intraplate tectonics in the northern Indian Ocean, *Phys. Earth Planet. Inter., 40*, 1-23, 1985.

Bergman, E. A., J. L. Nabelek, and S. C. Solomon, An extensive region of off-ridge normal-faulting earthquakes in the southern Indian Ocean, *J. Geophys. Res., 89*, 2425-2443, 1984.

Bonatti, E., R. Sartori, and A. Boersma, Vertical crustal movements at the Vema Fracture Zone in the Atlantic: Evidence from dredged limestones, *Tectonphysics, 91*, 213-232, 1983.

Bowen, A. N., and R. S. White, Deep-tow seismic profiles from the Vema transform and ridge-transform intersection, *J. Geol. Soc. Lond., 143*, 807-817, 1986.

Brace, W. F., and J. D. Byerlee, California earthquakes: Why only shallow focus?,

Science, 168, 1573-1576, 1970.

Brace, W. F., and D. L. Kohlstedt, Limits on lithospheric stress imposed by laboratory experiments, *J. Geophys. Res., 85*, 6248-6252, 1980.

Calvert, A. J., and R. B. Whitmarsh, The structure of the Charlie-Gibbs Fracture Zone, *J. Geol. Soc. Lond., 143*, 819-821, 1986.

Cande, S., J. L. LaBrecque, and W. B. Haxby, Plate kinematics of the South Atlantic: Chron 34 to present, *J. Geophys. Res.*, submitted, 1987.

Chen, W.-P., and P. Molnar, Focal depths of intracontinental and intraplate earthquakes and their implications for the thermal and mechanical properties of the lithosphere, *J. Geophys. Res., 88*, 4183-4214, 1983.

Christensen, D. H., and L. J. Ruff, Analysis of the trade-off between depth and source time function, *Bull. Seismol. Soc. Am., 75*, 1637-1656, 1985.

Collette, B. J., and K. W. Rutten, Crest and fracture zone geometry of the Mid-Atlantic Ridge between 10° and 16°N, *Nature Phys. Sci., 237*, 131-134, 1972.

Collette, B. J., H. Schouten, K. Rutten, and A. P. Slootweg, Structure of the Mid Atlantic Ridge province between 12° and 18°N, *Mar. Geophys. Res., 2*, 143-179, 1974.

Cormier, M.-H., R. S. Detrick, and G. M. Purdy, Anomalously thin crust in oceanic fracture zones: New seismic constraints from the Kane Fracture Zone, *J. Geophys. Res., 89*, 10249-10266, 1984.

Das, S., and C. H. Scholz, Why large earthquakes do not nucleate at shallow depths, *Nature, 305*, 621-623, 1983.

Detrick, R. S., and G. M. Purdy, The crustal structure of the Kane Fracture Zone from seismic refraction studies, *J. Geophys. Res., 85*, 3759-3777, 1980.

Detrick, R. S., M. H. Cormier, R. A. Prince, D. W. Forsyth, and E. L. Ambos, Seismic constraints on the crustal structure within the Vema Fracture Zone, *J. Geophys. Res.,*

87, 10599-10612, 1982.

Dziewonski, A. M., and D. L. Anderson, Preliminary reference Earth model, *Phys. Earth Planet. Inter., 25*, 297-356, 1981.

Dziewonski, A. M., and D. L. Anderson, Travel times and station corrections for P waves at teleseismic distances, *J. Geophys. Res., 88*, 3295-3314, 1983.

Dziewonski, A. M., A. Friedman, D. Giardini, and J. H. Woodhouse, Global seismicity of 1982: Centroid-moment tensor solutions for 308 earthquakes, *Phys. Earth Planet. Inter., 33*, 76-90, 1983.

Dziewonski, A. M., J. E. Franzen, and J. H. Woodhouse, Centroid-moment tensor solutions for January-March 1985, *Phys. Earth Planet. Inter., 40*, 249-258, 1985.

Ebel, J. E., L. J. Burdick, and G. S. Stewart, The source mechanism of the August 7, 1966 El Golfo earthquake, *Bull. Seismol. Soc. Am., 68*, 1281-1292, 1978.

Eittreim, S., and J. Ewing, Vema Fracture Zone transform fault, *Geology, 3*, 555-558, 1975.

Engeln, J. F., D. A. Wiens, and S. Stein, Mechanisms and depths of Atlantic transform earthquakes, *J. Geophys. Res., 91*, 548-577, 1986.

Feden, R. H., H. S. Fleming, R. K. Perry, and J. D. Phillips, The Mid-Atlantic Ridge at 33°N: The Hayes Fracture Zone, *Earth Planet. Sci. Lett., 26*, 292-298, 1975.

Fleming, H. S., N. Z. Cherkis, and J. R. Heirtzler, The Gibbs Fracture Zone: A double fracture zone at 52°30'N in the Atlantic Ocean, *Mar. Geophys. Res., 1*, 37-45, 1970.

Forsyth, D. W., and B. Wilson, Three-dimensional temperature structure of a ridge-transform-ridge system, *Earth Planet. Sci. Lett., 70*, 355-362, 1984.

Fox, P. J., and D. G. Gallo, A tectonic model for ridge-transform-ridge plate boundaries: Implications for the structure of oceanic lithosphere, *Tectonophysics, 104*, 205-242, 1984.

Fox, P. J., and D. G. Gallo, The geology of North Atlantic transform plate boundaries and their aseismic extensions, in *The Geology of North America, Vol. M, The Western North Atlantic Region*, edited by P. R. Vogt and B. E. Tucholke, Geol. Soc. Am., Boulder, Colo., pp. 157-172, 1986.

Fox, P. J., A. Lowrie, Jr., and B. C. Heezen, Oceanographer Fracture Zone, *Deep Sea Res., 16*, 59-66, 1969.

Fox, P. J., E. Schreiber, H. Rowlett, and K. McCamy, The geology of the Oceanographer Fracture Zone: A model for fracture zones, *J. Geophys. Res., 81*, 4117-4128, 1976.

Garfunkel, Z., Review of oceanic transform activity and development, *J. Geol. Soc. Lond., 143,* 775-784, 1986.

Giardini, D., A. M. Dziewonski, and J. H. Woodhouse, Centroid-moment tensor solutions for 113 large earthquakes in 1977-1980, *Phys. Earth Planet. Inter., 40*, 259-272, 1985.

Goetze, C., and B. Evans, Stress and temperature in the bending lithosphere as constrained by experimental rock mechanics, *Geophys. J. R. Astron. Soc., 59*, 463-478, 1979.

Goff, J. A., E. A. Bergman, and S. C. Solomon, Earthquake source mechanisms and transform fault tectonics in the Gulf of California, *J. Geophys. Res., 92,* 10485-10510, 1987.

Herrin, E., (Chairman), Seismological tables for P phases, *Bull. Seismol. Soc. Am., 58*, 1193-1241, 1968.

Huang, P. Y., S. C. Solomon, E. A. Bergman, and J. L. Nabelek, Focal depths and mechanisms of Mid-Atlantic Ridge earthquakes from body waveform inversion, *J. Geophys. Res., 91*, 579-598, 1986.

Jeffreys, H., and K. E. Bullen, *Seismological Tables,* Brit. Assoc. Advance. Sci., Gray

Milne Trust, London, 1940.

Jemsek, J. P., E. A. Bergman, J. L. Nabelek, and S. C. Solomon, Focal depths and mechanisms of large earthquakes on the Arctic mid-ocean ridge system, *J. Geophys. Res., 91*, 13993-14005, 1986.

Jordan, T. H., and K. A. Sverdrup, Teleseismic location techniques and their application to earthquake clusters in the south-central Pacific, *Bull. Seismol. Soc. Am., 71*, 1105-1130, 1981.

Kanamori, H., and D. L. Anderson, Theoretical basis of some empirical relations in seismology, *Bull. Seismol. Soc. Am., 65*, 1073-1095, 1975.

Kanamori, H., and G. S. Stewart, Mode of strain release along the Gibbs Fracture Zone, Mid-Atlantic Ridge, *Phys. Earth Planet. Inter., 11*, 312-332, 1976.

Karson, J. A., and H. J. B. Dick, Tectonics of ridge-transform intersections at the Kane Fracture Zone, *Mar. Geophys. Res., 6*, 51-98, 1983.

Kent, D. V., and F. M. Gradstein, A Jurassic to Recent chronology, in *The Geology of North America, Vol. M, The Western North Atlantic Region*, edited by P. R. Vogt and B. E. Tucholke, Geol. Soc. Am., Boulder, Colo., pp. 45-50, 1986.

Klitgord, K. D., and H. Schouten, Plate kinematics of the central Atlantic, in *The Geology of North America, vol. M, The Western North Atlantic Region*, edited by P. R. Vogt and B. E. Tucholke, pp. 351-378, Geol. Soc. Amer., Boulder, Colo., 1986.

Lilwall, R. C., and R. E. Kirk, Ocean-bottom seismograph observations on the Charlie-Gibbs Fracture Zone, *Geophys. J. R. Astron. Soc., 80*, 195-208, 1985.

Louden, K. E., and D. W. Forsyth, Crustal structure and isostatic compensation near the Kane Fracture Zone from topographic and gravity measurements, 1, Spectral analysis approach, *Geophys. J. R. Astron. Soc., 68*, 725-750, 1982.

Louden, K. E., R. S. White, C. G. Potts, and D. W. Forsyth, Structure and

seismotectonics of the Vema Fracture Zone, Atlantic Ocean, *J. Geol. Soc. Lond., 143*, 795-805, 1986.

Ludwig, W. J., and P. D. Rabinowitz, Structure of Vema Fracture Zone, *Mar. Geol., 35*, 99-110, 1980.

Macdonald, K. C., D. A. Castillo, S. P. Miller, P. J. Fox, K. A. Kastens, and E. Bonatti, Deep-tow studies of the Vema Fracture Zone, 1, Tectonics of a major slow slipping transform fault and its intersection with the Mid-Atlantic Ridge, *J. Geophys. Res., 91*, 3334-3354, 1986.

Minster, J. B., and T. H. Jordan, Present-day plate motions, *J. Geophys. Res., 83*, 5331-5354, 1978.

Mutter, J. C., R. S. Detrick, and North Atlantic Transect Study Group, Multichannel seismic evidence for anomalously thin crust at Blake Spur Fracture Zone, *Geology, 12*, 534-537, 1984.

Nabelek, J. L., Determination of earthquake source parameters from inversion of body waves, Ph.D. thesis, 346 pp., Mass. Inst. of Technol., Cambridge, 1984.

Nabelek, J. L., Geometry and mechanism of faulting of the 1980 El Asnam, Algeria, earthquake from inversion of teleseismic body waves and comparison with field observations, *J. Geophys. Res., 90*, 12713-12728, 1985.

Olivet, J.-L., X. LePichon, S. Monti, and B. Sichler, Charlie-Gibbs Fracture Zone, *J. Geophys. Res., 79*, 2059-2072, 1974.

OTTER (J. A. Karson, P. J. Fox, H. Sloan, K. T. Crane, W. S. F. Kidd, E. Bonatti, J. B. Stroup, D. J. Fornari, D. Elthon, P. Hamlyn, J. F. Casey, D. G. Gallo, D. Needham, and R. Sartori), The geology of the Oceanographer transform: The ridge-transform intersection, *Mar. Geophys. Res., 6*, 109-141, 1984.

OTTER (P. J. Fox, R. H. Moody, J. A. Karson, E. Bonatti, W. S. F. Kidd, K. T. Crane, D. G.

Gallo, J. B. Stroup, D. J. Fornari, D. Elthon, P. Hamlyn, J. F. Casey, D. Needham, and R. Sartori), The geology of the Oceanographer transform: The transform domain, *Mar. Geophys. Res., 7*, 329-358, 1985.

Parsons, B., and J. G. Sclater, An analysis of the variation of ocean floor bathymetry and heat flow with age, *J. Geophys. Res., 82*, 803-827, 1977.

Phillips, J. D., H. S. Fleming, R. H. Feden, W. E. King, and R. K. Perry, Aeromagnetic study of the Mid-Atlantic Ridge near the Oceanographer Fracture Zone, *Geol. Soc. Am. Bull., 86*, 1348-1357, 1975.

Phillips, J. D., R. E. Needham, and R. M. Sheppard, Seismic ray tracing for relocating oceanic ridge earthquakes, in *Seismic Discrimination*, Semiannual Technical Summary, M.I.T. Lincoln Laboratory Tech. Rep. ESD-TR-78-259, pp. 7-14, 1979.

Phipps Morgan, J., and D. W. Forsyth, 3-D flow and temperature perturbations due to a transform offset: Effects on oceanic crustal and upper mantle structure, *J. Geophys. Res.*, in press, 1987.

Pockalny, R. A., R. S. Detrick, and P. J. Fox, The morphology and tectonics of the Kane transform from Sea Beam bathymetry data, *J. Geophys. Res.*, in press, 1987.

Poppe, B. B., D. A. Naab, and J. S. Perry, Seismograph station codes and characteristics, *U.S. Geol. Surv. Circ., 791*, 171 pp., 1978.

Robb, J. M., and M. F. Kane, Structure of the Vema Fracture Zone from gravity and magnetic intensity profiles, *J. Geophys. Res., 80*, 4441-4445, 1975.

Roest, W. R., and B. J. Collette, The Fifteen Twenty Fracture Zone and the North American - South American plate boundary, *J. Geol. Soc. Lond., 143*, 833-843, 1986.

Roest, W. R., R. C. Searle, and B. J. Collette, Fanning of fracture zones and a three-dimensional model of the Mid-Atlantic Ridge, *Nature, 308*, 527-531, 1984.

Rowlett, H., and D. W. Forsyth, Recent faulting and microearthquakes at the intersection of the Vema Fracture Zone and the Mid-Atlantic Ridge, *J. Geophys. Res., 89*, 6079-6094, 1984.

Searle, R. C., The active part of Charlie-Gibbs Fracture Zone: A study using sonar and other geophysical techniques, *J. Geophys. Res., 86*, 243-262, 1981.

Searle, R. C., GLORIA investigations of oceanic fracture zones: Comparative study of the transform fault zone, *J. Geol. Soc. Lond., 143*, 743-756, 1986.

Sibson, R. H., Fault zone models, heat flow, and the depth distribution of earthquakes in the continental crust of the United States, *Bull. Seismol. Soc. Am., 72*, 151-163, 1982.

Sibson, R. H., Rupture interaction with fault jogs, in *Earthquake Source Mechanics, Geophys. Monogr. Ser.*, vol. 37, edited by S. Das, J. Boatwright, and C. H. Scholz, pp. 157-167, AGU, Washington, D.C., 1986.

Sinha, M. C., and K. E. Louden, The Oceanographer Fracture Zone, 1, Crustal structure from seismic refraction studies, *Geophys. J. R. Astron. Soc., 75*, 713-736, 1983.

Sleep, N. H., and S. Biehler, Topography and tectonics at the intersections of fracture zones with central rifts, *J. Geophys. Res., 75*, 2748-2752, 1970.

Solomon, S. C., Shear wave attenuation and melting beneath the Mid-Atlantic Ridge, *J. Geophys. Res., 78*, 6044-6059, 1973.

Stein, S., and D. A. Wiens, Depth determination for shallow teleseismic earthquakes: Methods and results, *Rev. Geophys., 24*, 806-832, 1986.

Strehlau, J., A discussion of the depth extent of rupture in large continental earthquakes, in *Earthquake Source Mechanics, Geophys. Monogr. Ser.*, vol. 37, edited by S. Das, J. Boatwright, and C. H. Scholz, pp. 131-145, AGU, Washington, D.C., 1986.

Sykes, L. R., Mechanism of earthquakes and nature of faulting on the mid-oceanic ridges, *J. Geophys. Res., 72*, 2131-2153, 1967.

Tucholke, B. E., and H. Schouten, Global plate motion changes recorded in the Kane Fracture Zone (abstract), *Geol. Soc. Am. Abstracts with Programs, 17*, 737, 1985.

van Andel, T. H., R. P. von Herzen, and J. D. Phillips, The Vema Fracture Zone and the tectonics of transverse shear zones in oceanic crustal plates, *Mar. Geophys. Res., 1*, 261-283, 1971.

Vogt, P. R., Portrait of a plate boundary: The Mid-Atlantic Ridge axis from the equator to Siberia (map), in *The Geology of North America, Vol. M, The Western North Atlantic Region*, edited by P. R. Vogt and B. E. Tucholke, Geol. Soc. Am., Boulder, Colo., Plate 8A, 1986.

Vogt, P. R., and O. E. Avery, Detailed magnetic surveys in the northeast Atlantic and Labrador Sea, *J. Geophys. Res., 79*, 363-389, 1974.

Weidner, D. J., and K. Aki, Focal depth and mechanism of mid-ocean ridge earthquakes, *J. Geophys. Res., 78*, 1818-1831, 1973.

White, R. S., R. S. Detrick, M. C. Sinha, and M.-H. Cormier, Anomalous seismic crustal structure of oceanic fracture zones, *Geophys. J. R. Astron. Soc., 79*, 779-798, 1984.

Wiens, D. A., and S. Stein, Age dependence of oceanic intraplate seismicity and implications for lithospheric evolution, *J. Geophys. Res., 88*, 6455-6468, 1983.

Wiens, D. A., and S. Stein, Intraplate seismicity and stresses in young oceanic lithosphere, *J. Geophys. Res., 89*, 11442-11464, 1984.

Williams, C. A., K. E. Louden, and S. J. Tanner, The western intersection of Oceanographer Fracture Zone with the Mid-Atlantic Ridge, *Mar. Geophys. Res., 6*, 143-158, 1984.

Wyss, M., Apparent stresses of earthquakes on ridges compared to apparent stresses

of earthquakes in trenches, *Geophys. J. Roy. Astron. Soc., 19*, 479-484, 1970.

E. A. Bergman and S. C. Solomon, Bldg. 54-512, Department of Earth, Atmospheric, and Planetary Sciences, Masachusetts Institute of Technology, Cambridge, MA 02139

FIGURE CAPTIONS

Figure 1. Schematic map of the northern Mid-Atlantic Ridge, showing fracture zone traces (dashed lines) and the six transform faults considered in this study. Transverse Mercator projection, centered on the 40°W meridian. Adapted from *Vogt* [1986].

Figure 2. Bathymetry, tectonic lineations, and locations and mechanisms of large earthquakes on the western segment of the Gibbs transform. The epicenters of the earthquakes of February 13, 1967, and October 16, 1974, are from the ISC and are probably mislocated by 10-15 km to the north (see text). The focal mechanisms determined in this study by body waveform inversion are shown as equal-area projections of the lower focal hemisphere; compressional quadrants are shaded. Major transform-parallel tectonic lineations (heavy lines), identified from GLORIA side-scan sonar images, and bathymetric contours, in kilometers, are from *Searle* [1981]. Ridge-transform intersections are indicated by solid diamonds.

Figure 3. Bathymetry of the western end of the Oceanographer transform. Bathymetric contours, in hundreds of meters at 200 m intervals, are from *Williams et al.* [1984]. The positions of the RTI (solid diamond) and the PTDZ are from *Williams et al.* [1984]. Also shown are the focal mechanism, determined by body waveform inversion, and the ISC epicenter (probably mislocated by 10-15 km to the north) for the earthquake of May 17, 1964.

Figure 4. Bathymetry and tectonic lineations of the Hayes transform. Bathymetric contours, in hundreds of meters at 500 m intervals, are from *Feden et al.* [1975]. Tectonic lineations (heavy lines), inferred from a GLORIA side-scan sonar survey, are from R. C. Searle (personal communication, 1986); barbed lines indicate normal faults (barb on the downthrown side). The inferred positions of the RTIs are indicated by solid diamonds. Also shown are the ISC epicenter (probably mislocated by 10 km to the north) of the earthquake of March 28, 1976, and the focal mechanism determined in this study by body waveform inversion.

Figure 5. Bathymetry and tectonic lineations of the Kane transform. Bathymetric contours, in hundreds of meters at 500 m intervals, are from a Sea Beam survey by *Pockalny et al.* [1987]. Areas deeper than 4500 m are shaded, and closed highs and lows are indicated by + and - signs. Tectonic lineations (heavy lines) are from a GLORIA side-scan sonar survey reported by *Searle* [1986]. Positions of ridge-transform intersections are indicated by solid diamonds. Also shown are the ISC epicenter of the earthquake of March 26, 1980, and the relocated epicenter of the earthquake of May 19, 1963 (see text). Both epicenters are probably mislocated to the north by 5-15 km. Focal mechanisms were determined in this study by body waveform inversion.

Figure 6. Bathymetry and tectonic lineations of the 15°20' transform. Bathymetric contours, in hundreds of meters at 500 m intervals, are from *Searle* [1986].

Tectonic lineations (heavy lines) are from a GLORIA side-scan sonar survey [*Searle*, 1986]. Positions of ridge-transform intersections are indicated by solid diamonds. Also shown are the ISC epicenters (probably mislocated by about 5 km to the north) of the earthquakes of September 24, 1969, June 19, 1970, and December 9, 1972, along with the focal mechanisms determined in this study by body waveform inversion.

Figure 7. Bathymetry of the western end of the Vema transform. Bathymetric contours, in hundreds of meters, are from *Louden et al.* [1986]. The position of the PTDZ is from *Rowlett and Forsyth* [1984]. The position of the RTI is shown by a solid diamond. Also shown are the ISC epicenter for the earthquake of May 14, 1976, the epicenters determined for the earthquake of March 17, 1962 by the USCGS, ISS, and our relocation (see text), and the ISC epicenter for a large (M_s 5.8) earthquake that occurred on January 10, 1985. All teleseismic epicenters are probably mislocated to the south by 5-10 km. Focal mechanisms were determined in this study by body waveform inversion.

Figure 8. Bathymetry and locus of the PTDZ for a portion of the central section of the Vema transform, from *Macdonald et al.* [1986]. The 5 km isobath is shown. Also shown are the ISC epicenter (mislocated by about 5 km to the south) for the earthquake of August 25, 1979, and the focal mechanism determined in this study by body waveform inversion.

Figure 9. Histogram of travel-time residuals (observed - theoretical) for P waves from stations at epicentral distances of less than 105° from the Vema transform earthquake of March 17, 1962. The bimodal distribution shows the contribution to the reported arrival times of a small precursor which preceded the main rupture by about 5 s (see text).

Figure 10. (a) Residual variance as a function of centroid depth for two of the earthquakes in this study. The horizontal lines indicate the range in acceptable centroid depths at 90% confidence as given by the paired *t* test of *Huang et al.* [1986]. The shaded region indicates the range in acceptable centroid depths based on the 1% residual variance rule discussed in the text. (b) Best-fitting source time function (STF) for the 1976 Hayes transform earthquake, obtained in a series of waveform inversions with the centroid depth constrained at the indicated values. The double-peaked character at shallow depths yields waveforms that mimic depth phases.

Figure 11. Cross-sections for the Vema, Gibbs, and 15°20' transforms, showing the centroid depths and approximate depth extent of rupture during the earthquakes of this study and nominal isotherms (400, 600, 800, and 1000°C) given by a simple thermal model (see text). No vertical exaggeration. One estimate of the depth extent of rupture is from the seafloor to twice the centroid depth (vertical bars). For the smaller events

of this study, the depth extent of rupture has also been estimated from a simple circular fault model (circles).

Figure 12. Cross-sections for Kane, Oceanographer, and Hayes transforms, showing the centroid depths and approximate depth extent of rupture during the earthquakes of this study and nominal isotherms (400, 600, 800, and 1000°C) given by a simple thermal model (see text). See Figure 11 for further information.

Figure 13. Centroid depth versus lithosphere age for 18 oceanic intraplate earthquakes with strike-slip mechanisms. Two pairs of data points represent strike-slip subevents of earthquakes modelled as two or three point sources. Isotherms are from the plate cooling model of *Parsons and Sclater* [1977], with parameters identical to those assumed for the transform fault thermal model shown in Figures 11 and 12. Source parameters for these intraplate earthquakes were determined with the same body waveform inversion procedure as that used in this study. Fault radii were determined from the length of the source time function in the same manner as for the transform fault earthquakes (Appendix B). For three shallow events with apparent fault radii greater than their centroid depths, a rectangular fault geometry has been assumed and the rupture is assumed to extend from the seafloor to twice the centroid depth.

Figure A1. Observed (solid lines) long-period P and SH waves from the earthquake of February 13, 1967, on the Gibbs transform compared with synthetic

waveforms (dashed lines) generated for a source model with two point sources. The parameters of the first, small subevent were fixed in the inversion; the source parameters of the second subevent and its origin time and location relative to the first subevent were found from body-waveform inversion. The radiation pattern of the largest subevent is shown. P and SH radiation patterns are shown on the lower focal hemisphere (equal area projection). All amplitudes are normalized to an epicentral distance of 40° and a WWSSN instrument magnification of 1500; the amplitude scales correspond to the waveforms that would be observed on an original seismogram from such an instrument. The two vertical lines delimit the portion of each time series used in the inversion. For SH waves, compression corresponds to positive motion as defined by *Aki and Richards* [1980]. Full names and locations of all stations are given by *Poppe et al.* [1978].

Figure A2. Observed P and SH waves from the earthquake of October 16, 1974, on the Gibbs transform compared with synthetic waveforms generated for a source model with two point sources. The parameters of the first, small subevent were fixed in the inversion; the source parameters of the second subevent and its origin time and location relative to the first subevent were found from body-waveform inversion. The radiation pattern of the largest subevent is shown. See Figure A1 for further explanation.

Figure A3. Observed P and SH waves from the earthquake of May 17, 1964, on the

Oceanographer transform compared with synthetic waveforms generated for the best-fitting point source mechanism found from body-waveform inversion. See Figure A1 for further explanation.

Figure A4. Observed P and SH waves from the earthquake of March 28, 1976, on the Hayes transform compared with synthetic waveforms generated for the best-fitting point source mechanism found from body-waveform inversion. See Figure A1 for further explanation.

Figure A5. Observed P and SH waves from the earthquake of May 19, 1963, on the Kane transform compared with synthetic waveforms generated for a source model with two point sources, the parameters of which were found from body-waveform inversion. The radiation pattern of the largest subevent is shown. See Figure A1 for further explanation.

Figure A6. Observed P and SH waves from the earthquake of March 26, 1980, on the Kane transform compared with synthetic waveforms generated for a source model with two point sources, the parameters of which were found from body-waveform inversion. The radiation pattern of the largest subevent is shown. See Figure A1 for further explanation.

Figure A7. Observed P and SH waves from the earthquake of September 24, 1969, on the 15°20' transform compared with synthetic waveforms generated for the best-fitting point source mechanism found from body-waveform inversion. See Figure A1 for further explanation.

Figure A8. Observed P and SH waves from the earthquake of June 19, 1970, on the

15°20' transform compared with synthetic waveforms generated for the best-fitting point source mechanism found from body-waveform inversion. See Figure A1 for further explanation.

Figure A9. Observed P and SH waves from the earthquake of December 9, 1972, on the 15°20' transform compared with synthetic waveforms generated for the best-fitting point source mechanism found from body-waveform inversion. See Figure A1 for further explanation.

Figure A10. Observed P and SH waves from the earthquake of March 17, 1962, on the Vema transform compared with synthetic waveforms generated for the best-fitting point source mechanism found from body-waveform inversion. See Figure A1 for further explanation.

Figure A11. Observed P and SH waves from the earthquake of May 14, 1976, on the Vema transform compared with synthetic waveforms generated for the best-fitting point source mechanism found from body-waveform inversion. See Figure A1 for further explanation.

Figure A12. Observed P and SH waves from the earthquake of August 25, 1979, on the Vema transform compared with synthetic waveforms generated for a source model with two point sources. The parameters of the first, small subevent were fixed in the inversion; the source parameters of the second subevent and its origin time and location relative to the first subevent were found from body-waveform inversion. The radiation pattern of the largest subevent is shown. See Figure A1 for further explanation.

TABLE 1. Transform Fault Data

Transform	Ridge-Transform Intersections[a]				Length,[b] km	Age Offset,[c] m.y.
	°N	°W	°N	°W		
Gibbs (West)	52.74	34.70	52.56	31.69	195	22
Oceanographer	35.25	36.20	35.05	35.00	105	10
Hayes	33.75	39.06	33.58	38.27	70	6
Kane	23.84	46.34	23.65	44.87	150	11
15°20'	15.33	46.62	15.20	44.95	180	13
Vema	10.85	43.64	10.71	40.90	300	20

[a] Location convention described in the text.

[b] Length of the transform, calculated as the distance between the two ridge-transform intersections, rounded to the nearest 5 km.

[c] Offset in seafloor age across the transform, determined for most transforms from magnetic anomalies [*Klitgord and Schouten,* 1986] and the magnetic chronology scale of *Kent and Gradstein* [1986]. For the Hayes transform, the age offset is estimated from the transform length and the spreading rate given by plate motion model RM2 [*Minster and Jordan*, 1978]. For the Vema transform the age offset is from the South American-African plate reconstruction of *Cande et al.* [1987].

TABLE 2. Epicentral Data[a] and Earthquake Source Parameters

Position[b]	Date	Origin Time, UT	Lat., °N	Long., °W	m_b	M_S	M_0[c]	Mechanism[d]	Depth,[e] km	STF,[f] s
Gibbs										
20	Feb. 13, 1967[g]	2314:22.3	52.82	34.25	5.6	6.5[h]	18	098/84/183	10	12
175	Oct. 16, 1974[g]	0545:11.2	52.71	32.00	5.7	6.9	32	098/87/178	10	15
Oceanographer										
10	May 17, 1964	1926:21.6	35.35	36.08	5.6		2.6	280/89/001	9	4
Hayes										
35	March 28, 1976	2019:45.8	33.79	38.64	5.5	5.8	0.84	281/85/002	9	2.5
Kane										
45	May 19, 1963	2135:49.3	23.83	45.94	6.0	6.5	5.2	099/83/175	7	4.5
							1.7	048/44/098	6	2
75	March 26, 1980	2043:36.4	23.86	45.57	5.8	6.3	4.4	100/86/179	8	4
							1.0	033/38/084	4	4
15°20'										
90	Sept. 24, 1969	1803:19.9	15.30	45.78	5.8	6.4	9.1	098/88/180	5	8
75	June 19, 1970	1425:20	15.34	45.92	5.5	5.8	1.2	097/89/179	5	3
160	Dec. 9, 1972	0644:40	15.25	45.15	5.5	5.7	0.87	097/89/178	4	2.5
Vema										
60	March 17, 1962	2047:33.6	10.77	43.11		7	31	276/58/187	10	10
15	May 14, 1976	0625:33	10.79	43.51	5.5	5.7	1.0	269/49/175	9	4
215	Aug. 25, 1979[g]	0844:04.5	10.72	41.68	6.0	6.6	12	087/89/172	7	10

[a] For events in 1964-1980, epicentral data and m_b are from the ISC and M_S is from the ISC, NEIS, or USCGS. For events in 1962 and 1963, the epicentral data are determined in this study (see text), m_b values are from USCGS, and M_S values are Pasadena magnitudes.

[b] Position of the epicenter along the transform, to the nearest 5 km east of the western ridge-transform intersection.

[c] Seismic moment in units of 10^{25} dyn cm (10^{18} N m).

[d] Double couple mechanism (strike/dip/slip), specified with the convention of *Aki and Richards* [1980].

[e] Centroid depth below the seafloor.

[f] Duration of the source time function (STF).

[g] Source parameters are for the primary subevent in a multiple-source model. See Appendix A.

[h] From *Kanamori and Stewart* [1976].

TABLE 3. Assumed Source Structure

Layer	V_p, km/s	V_s, km/s	Density, g/cm^3	Thickness, km
Water	1.5	0.0	1.0	variable
Sediment	2.0	0.5	2.0	variable
Crust	4.3	2.5	2.5	2.2
Crust	5.9	3.4	2.6	2.6
Mantle	8.1	4.6	3.4	halfspace

TABLE 4. Derived Source Parameters[a]

Date	Rupture Direction	Rise Time, s	Rupture Time, s	Length, km	Width, km	Radius, km	Area, km^2	Slip, cm	$\Delta\sigma$, bars
Gibbs									
Feb. 13, 1967[b]	East	5	7	25	20		500	72	11
Oct. 16, 1974[b]	East	5	10	35	20		700	91	15
Oceanographer									
May 17, 1964	West	1	3			6.4	130	40	43
Hayes									
March 28, 1976		1.2	1.2			4.0	50	33	57
Kane									
May 19, 1963[b]	East	1.5	3			7.2	160	64	61
March 26, 1980[b]	East	1	3			6.4	130	68	73
15°20'									
Sept. 24, 1969	East	2	6	21	10		210	87	28
June 19, 1970		1.5	1.5			4.8	70	33	47
Dec. 9, 1972		1	1.5			4.0	50	35	59
Vema									
March 17, 1962		4	6	42	24		1000	62	8
May 14, 1976		2	2			6.4	130	16	17
Aug. 25, 1979[b]	East	2	8	28	14		390	61	14

[a] Estimates of fault dimensions and average rupture characteristics are derived from the source parameters (seismic moment, double-couple mechanism, centroid depth, and source time function) determined in the body waveform inversion, as discussed in Appendix B.

[b] Source parameters are for the primary strike-slip subevent of a multiple-subevent model. See Appendix A.

TABLE 5. Earthquake Slip Vector Azimuths

Date	Transform Strike[a]	Slip Vector Azimuth	
		This Study	*Engeln et al.* [1986]
Gibbs	96		
Feb. 13, 1967[b]		98	94
Oct. 16, 1974[b]		98	102
Oceanographer	102		
May 17, 1964		100	
Hayes	104		
March 28, 1976		101	91
Kane	98		
May 19, 1963[b]		100	
March 26, 1980[b]		100	
15°20'	95		
Sept. 24, 1969		98	103
June 19, 1970		97	95
Dec. 9, 1972		97	100
Vema	93		
March 17, 1962		92	
May 14, 1976		92	106
Aug. 25, 1979[b]		87	148

All azimuths are given in degrees measured clockwise from north.

[a] A representative strike direction of the transform fault, given by the average direction at the endpoints of the great circle segment connecting the ridge-transform intersections (Table 1).

[b] Slip vector from this study is for the primary strike-slip subevent in a multiple-source model. See Appendix A.

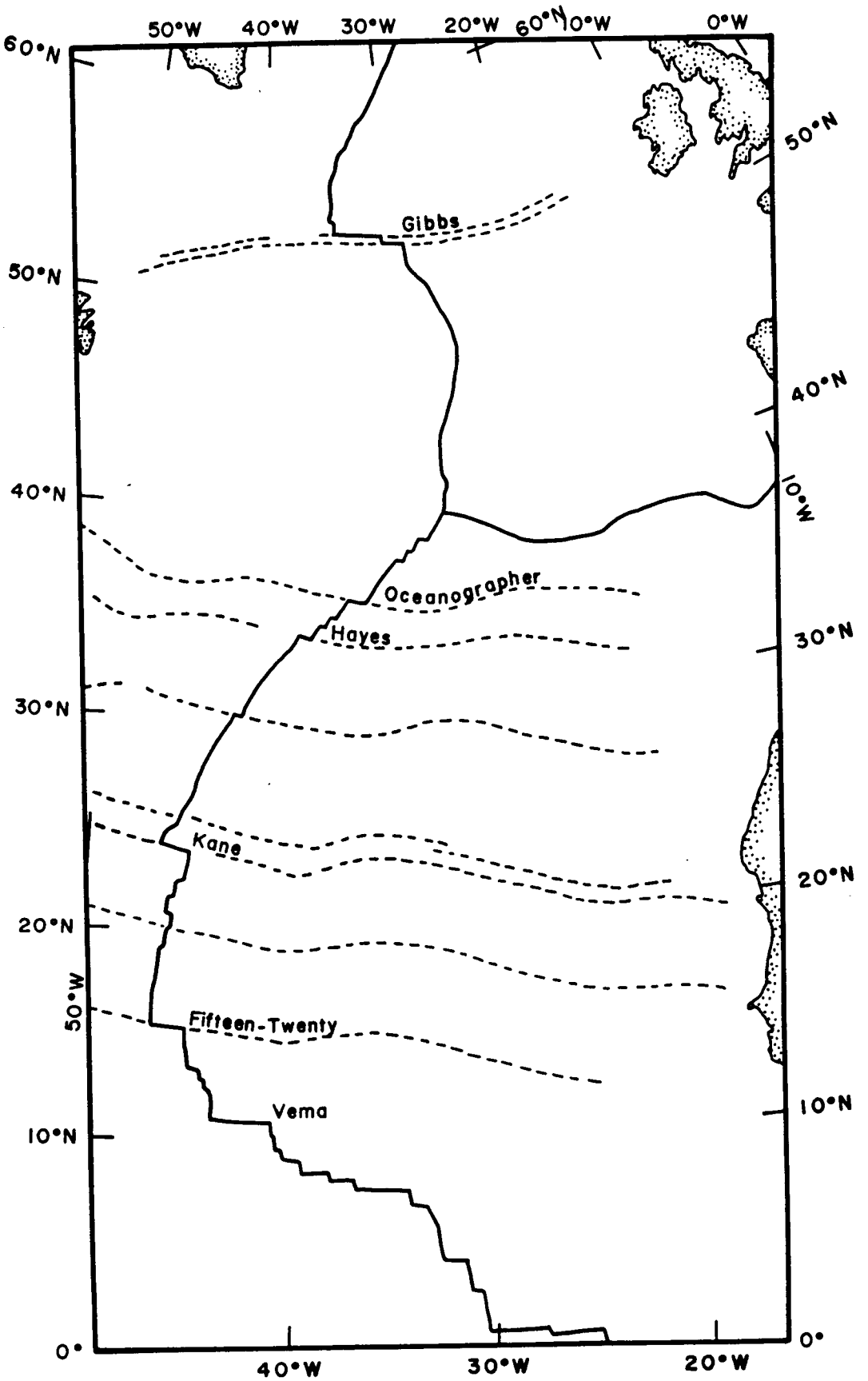
50°W
40°W
30°W
20°W
60°N
10°W
0°W
60°N
50°N
40°N
30°N
20°N
10°N
0°
Gibbs
Oceanographer
Hayes
Kane
Fifteen-Twenty
Vema

Figure 1

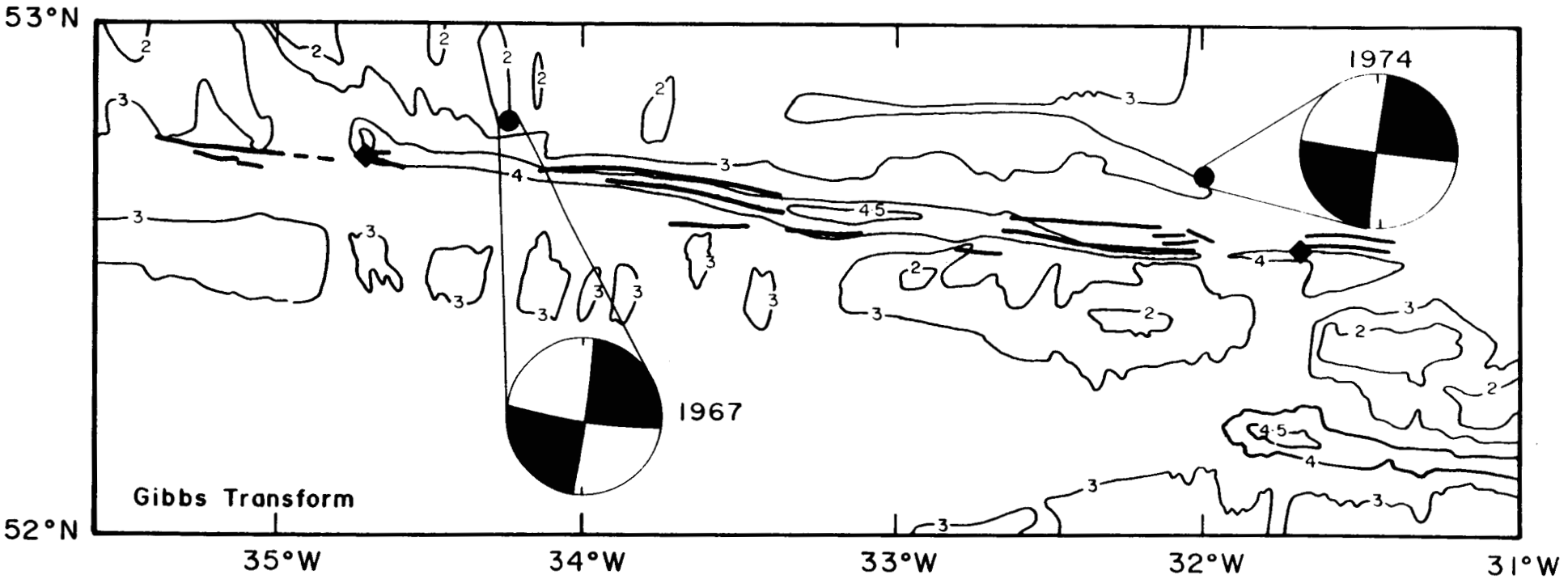

Figure 2

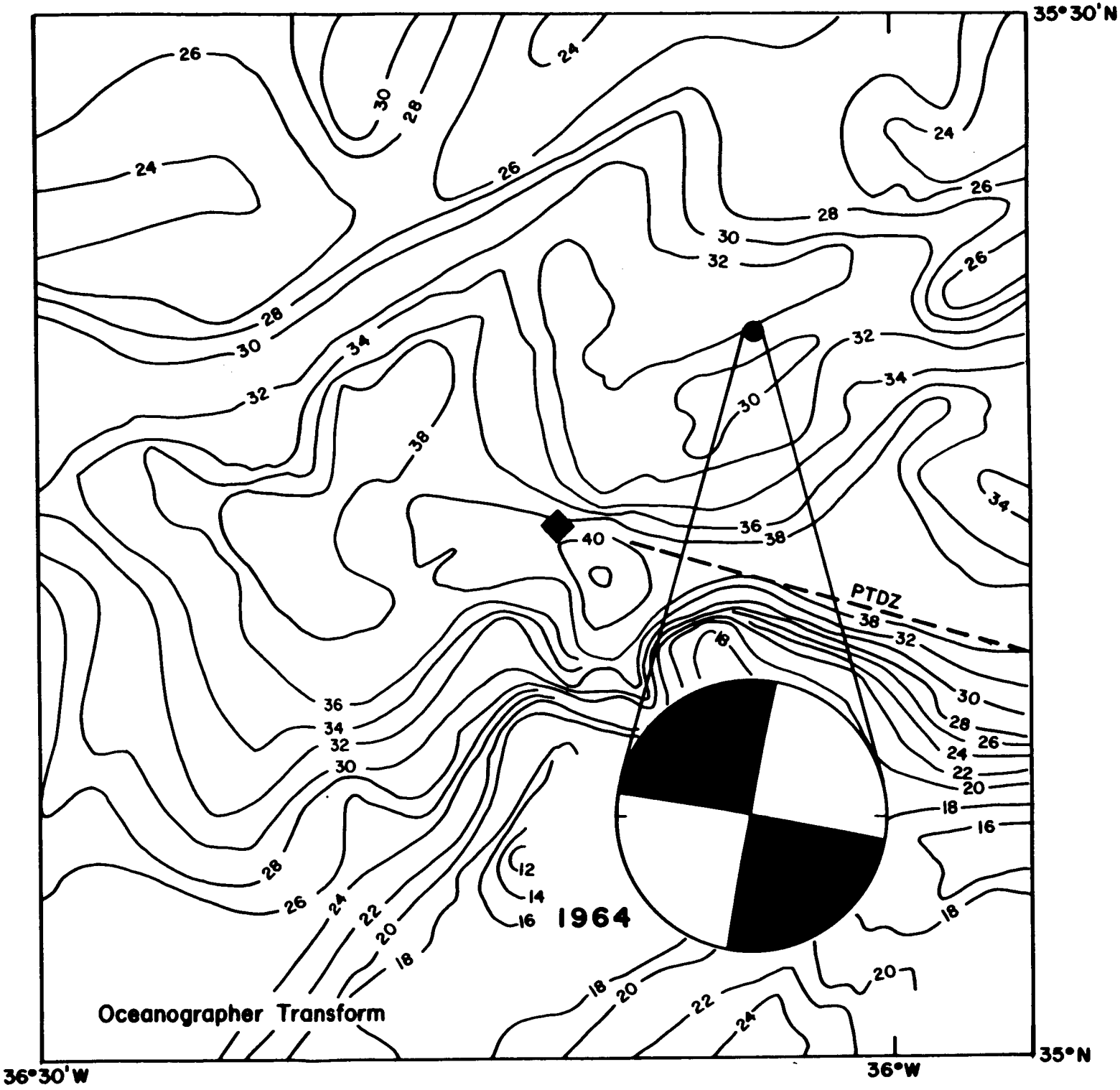

Figure 3

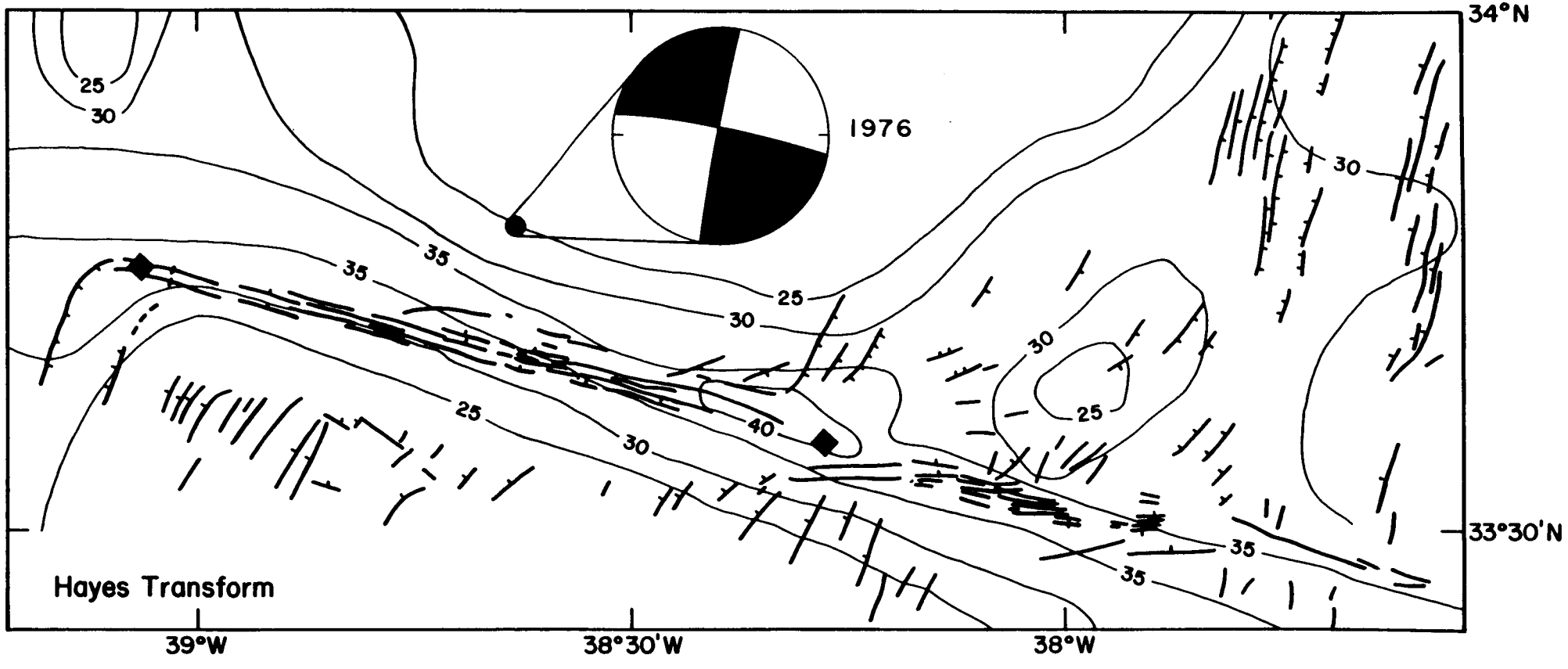
34°N
1976
25
30
35
35
25
30
30
25
40
25
30
30
35
35
Hayes Transform
39°W
38°30'W
38°W
33°30'N

Figure 4

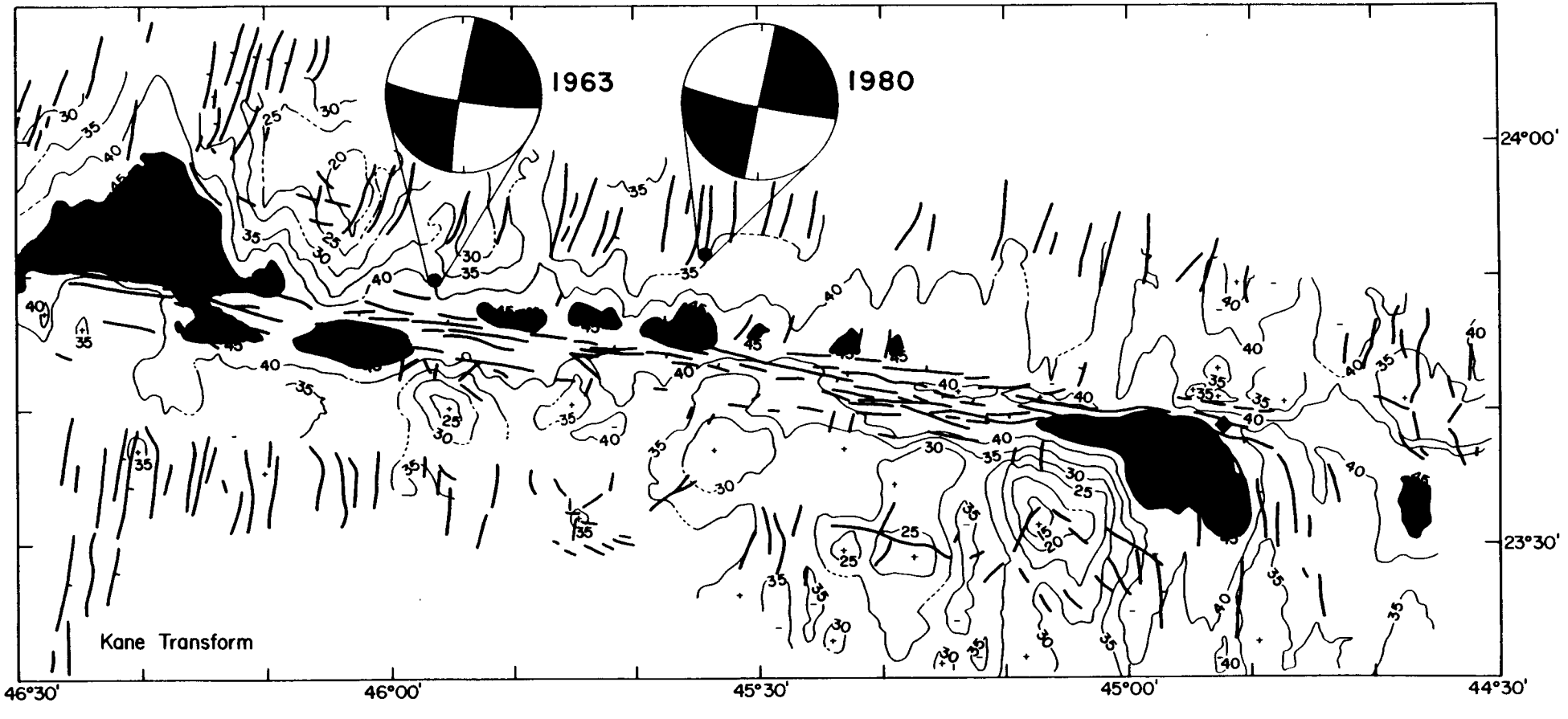

Figure 5

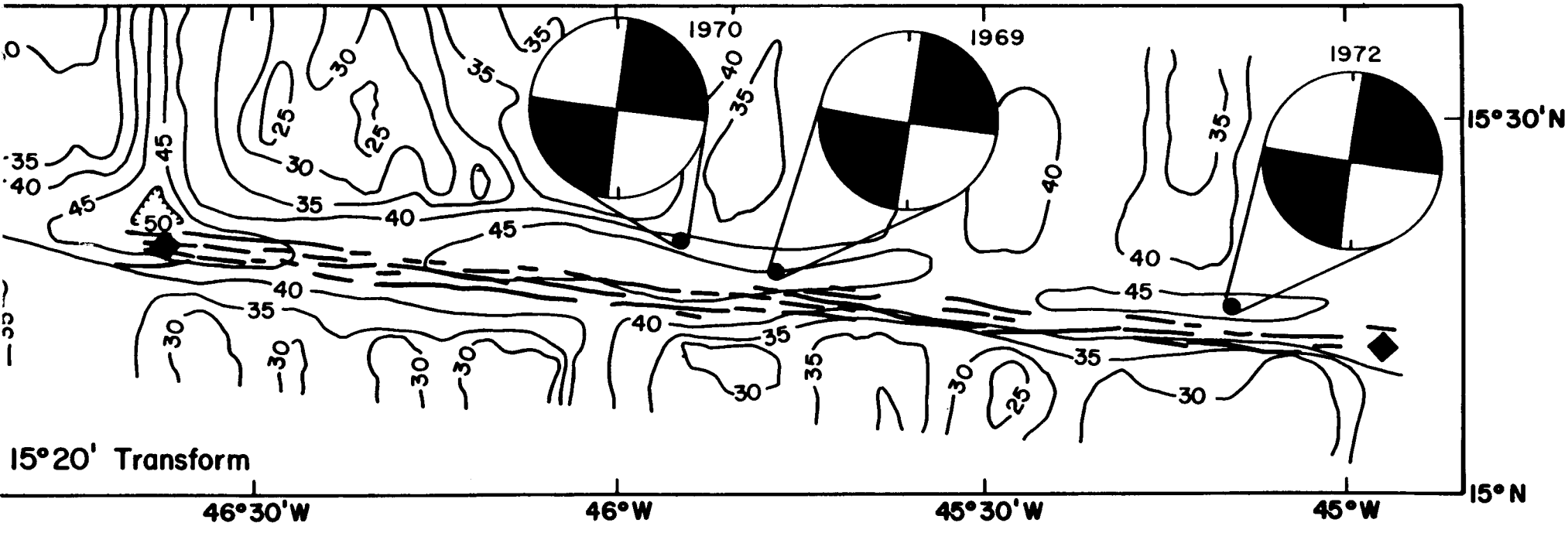

Figure 6

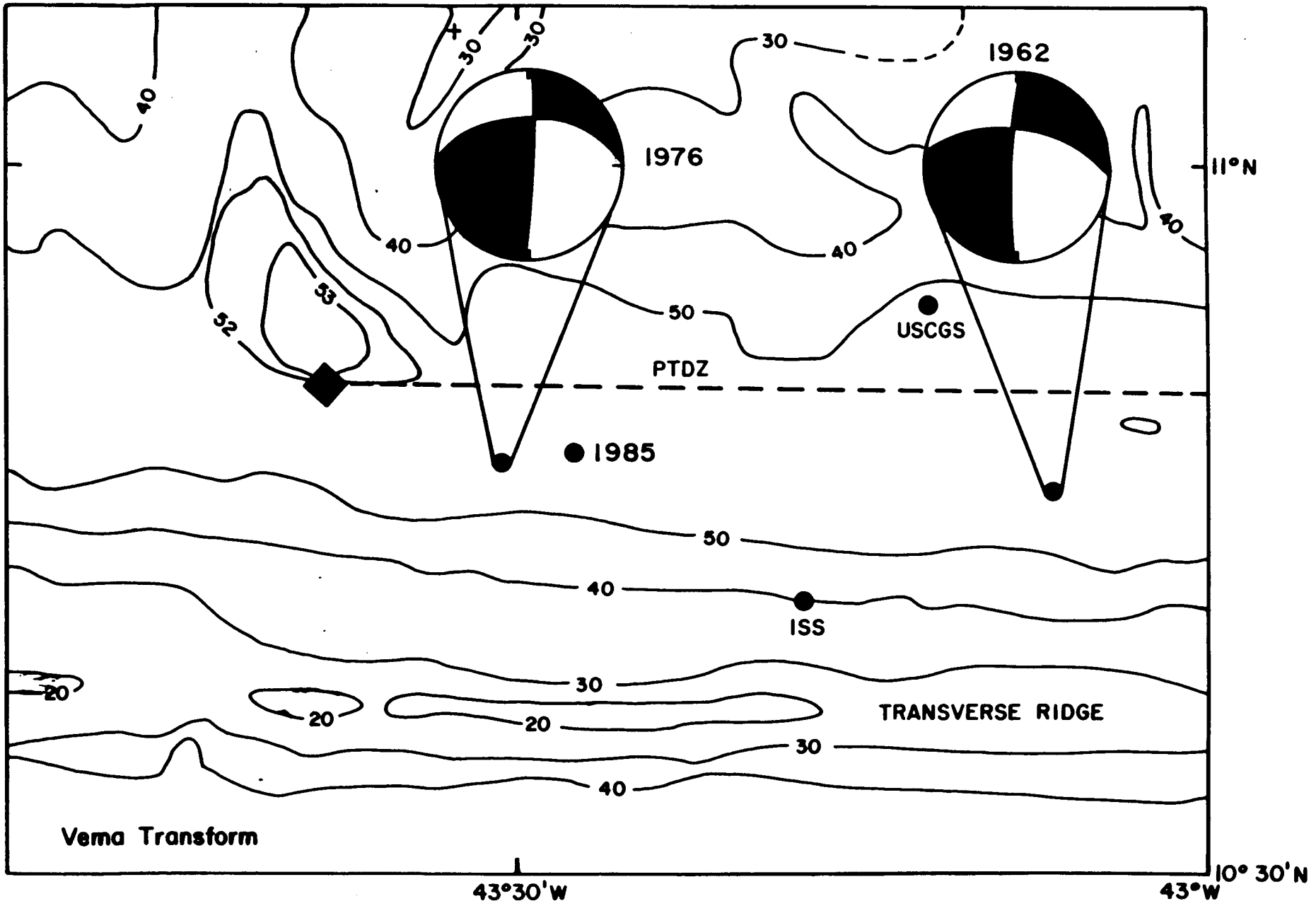
1962
1976
1985
USCGS
PTDZ
ISS
TRANSVERSE RIDGE
Vema Transform
11°N
10° 30'N
43°30'W
43°W
40
30
50
52
53
20

Figure 7

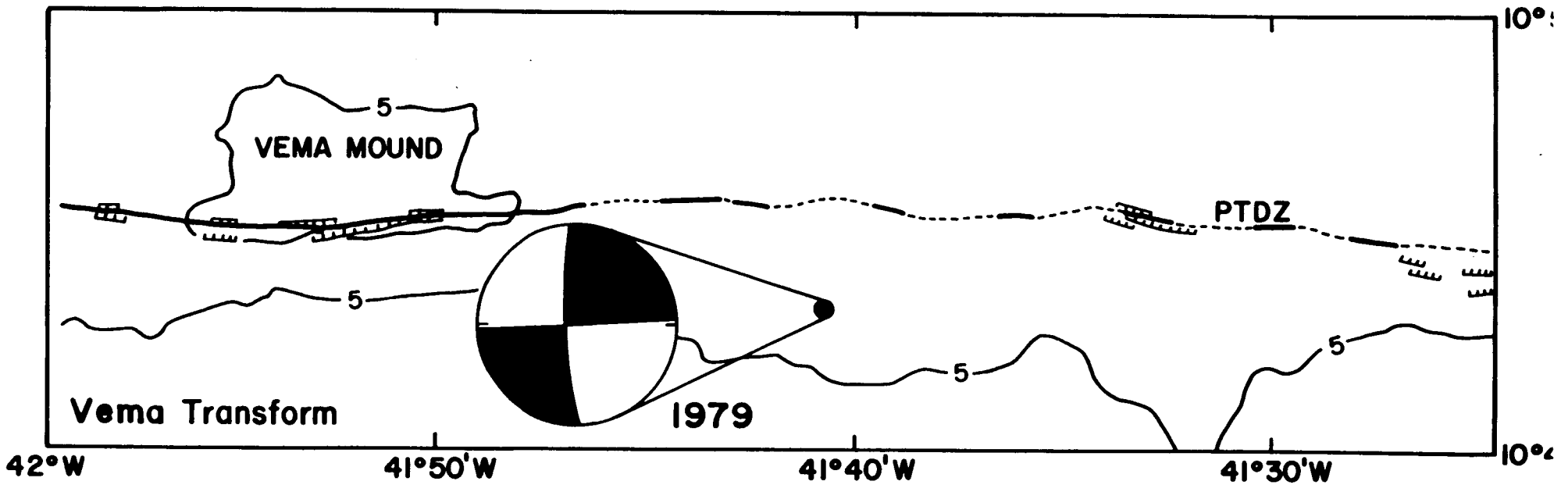
VEMA MOUND
5
PTDZ
5
5
5
Vema Transform
1979
42°W
41°50'W
41°40'W
41°30'W
10°

Figure 8

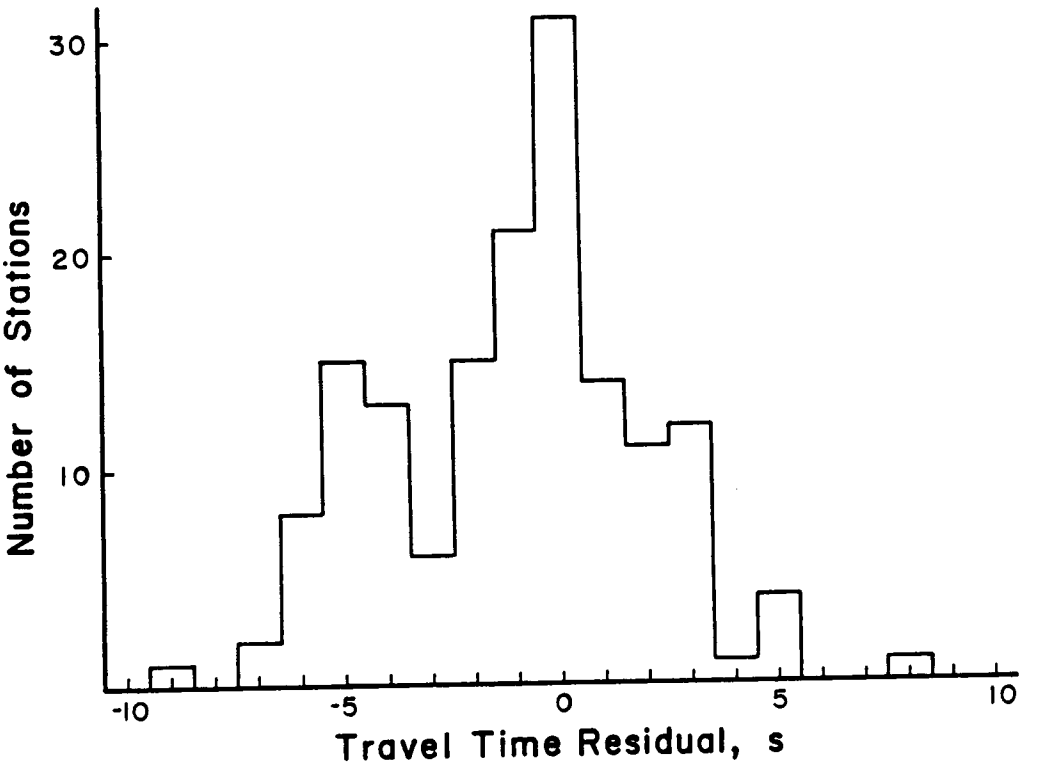

Figure 9

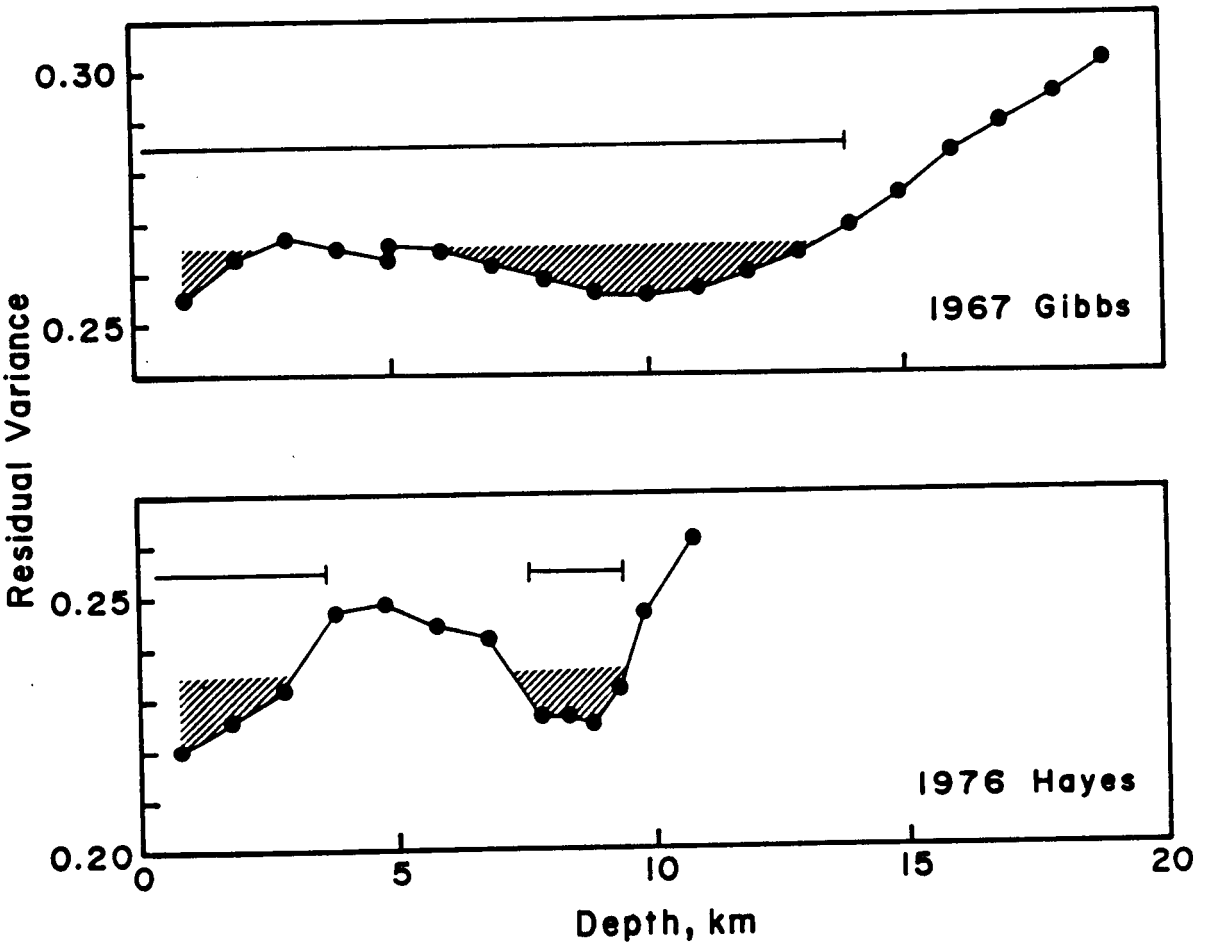
0.30
0.25
Residual Variance
1967 Gibbs
0.25
0.20
1976 Hayes
0
5
10
15
20
Depth, km

Figure 10a

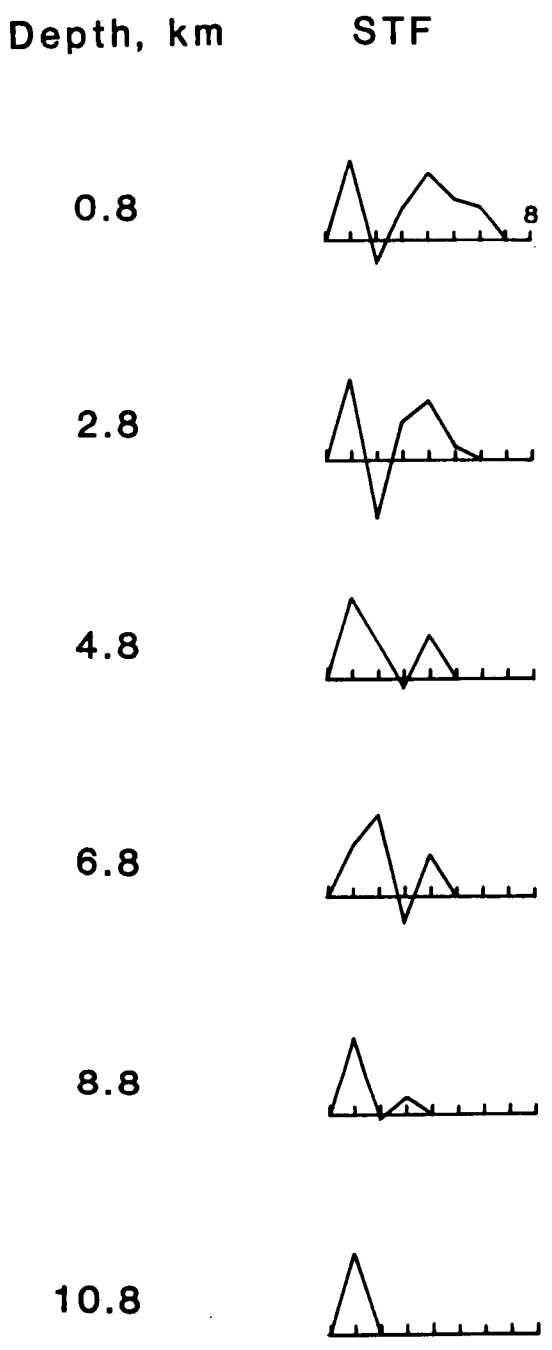

Figure 10b

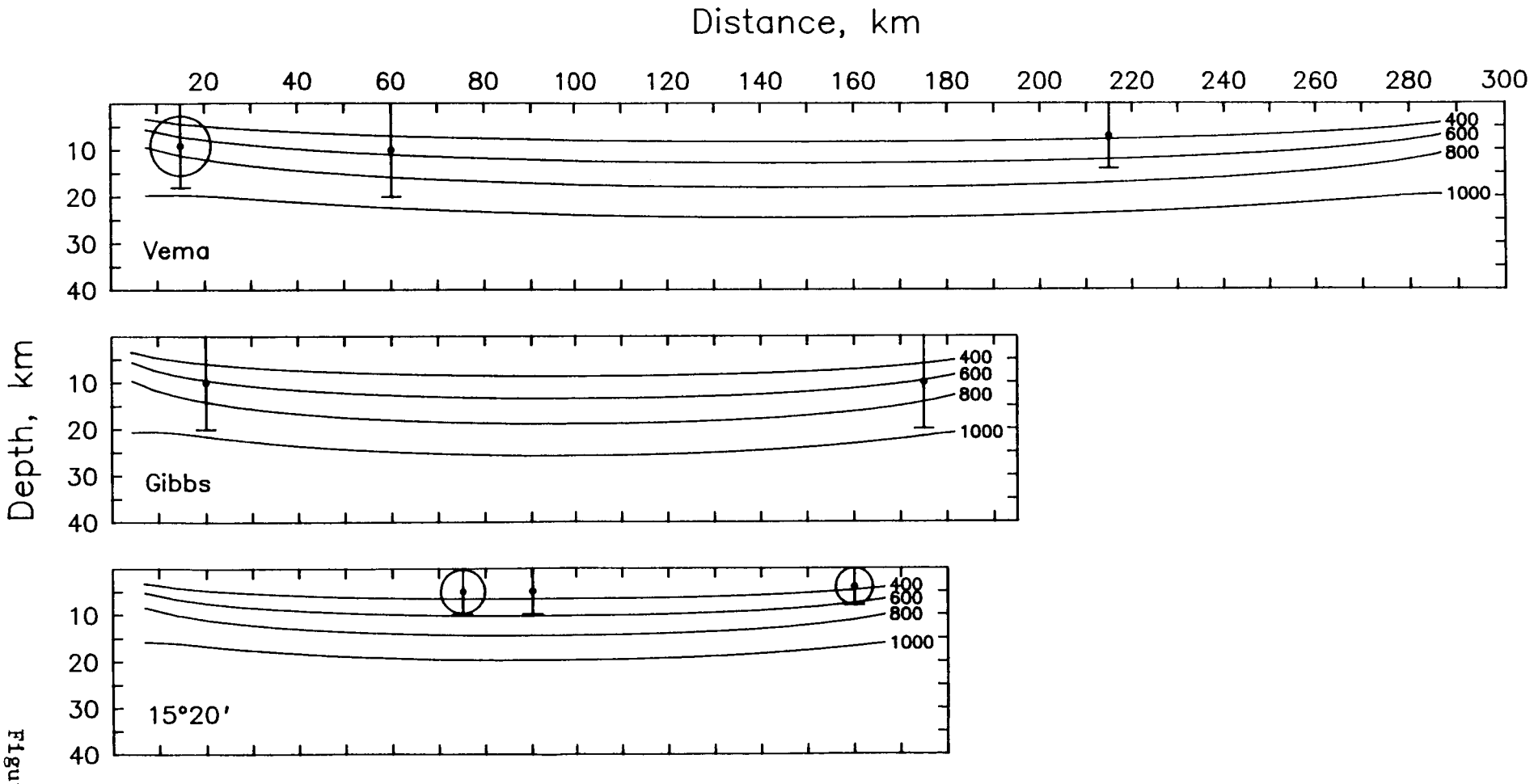
Distance, km
20
40
60
80
100
120
140
160
180
200
220
240
260
280
300
Depth, km
10
20
30
40
400
600
800
1000
Vema
Gibbs
15°20'

Figure 11

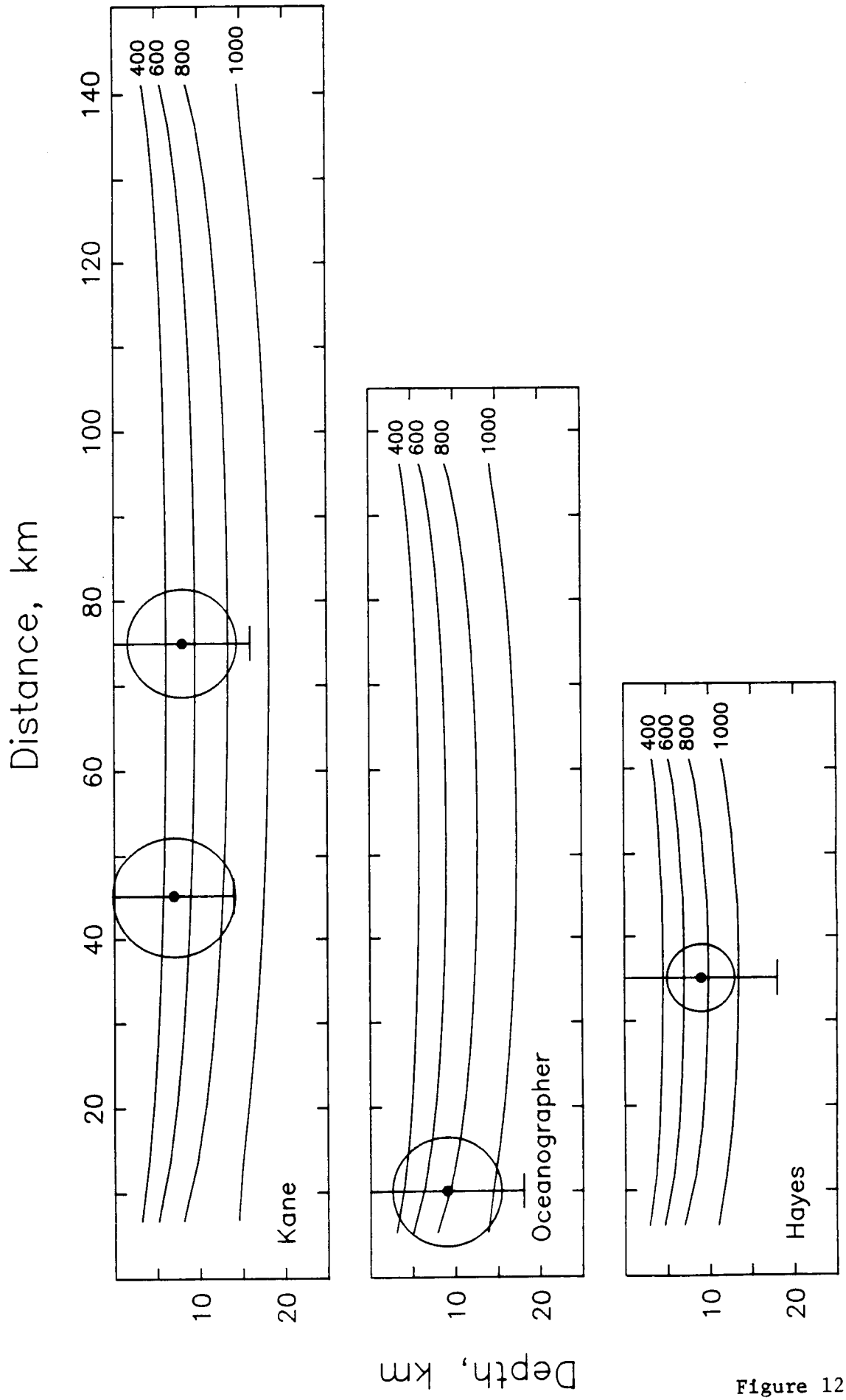
Distance, km
20
40
60
80
100
120
140
400
600
800
1000
Kane
Oceanographer
Hayes
10
20
Depth, km

Figure 12

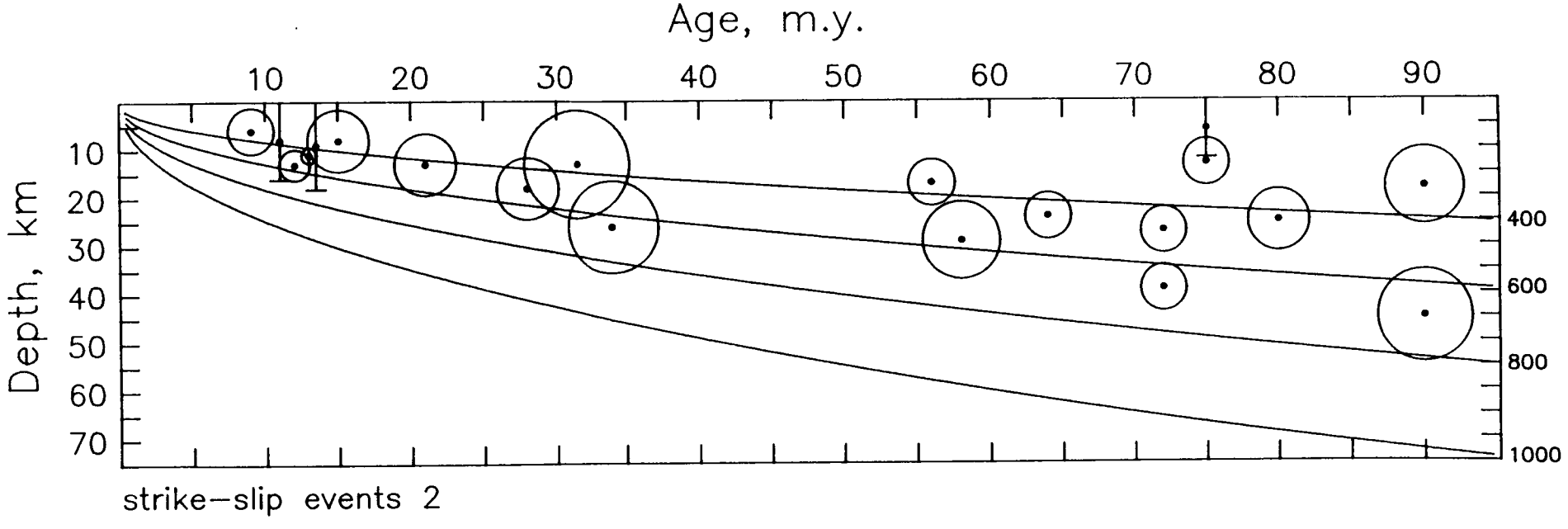
Age, m.y.
10
20
30
40
50
60
70
80
90
Depth, km
10
20
30
40
50
60
70
400
600
800
1000
strike–slip events 2

Figure 13

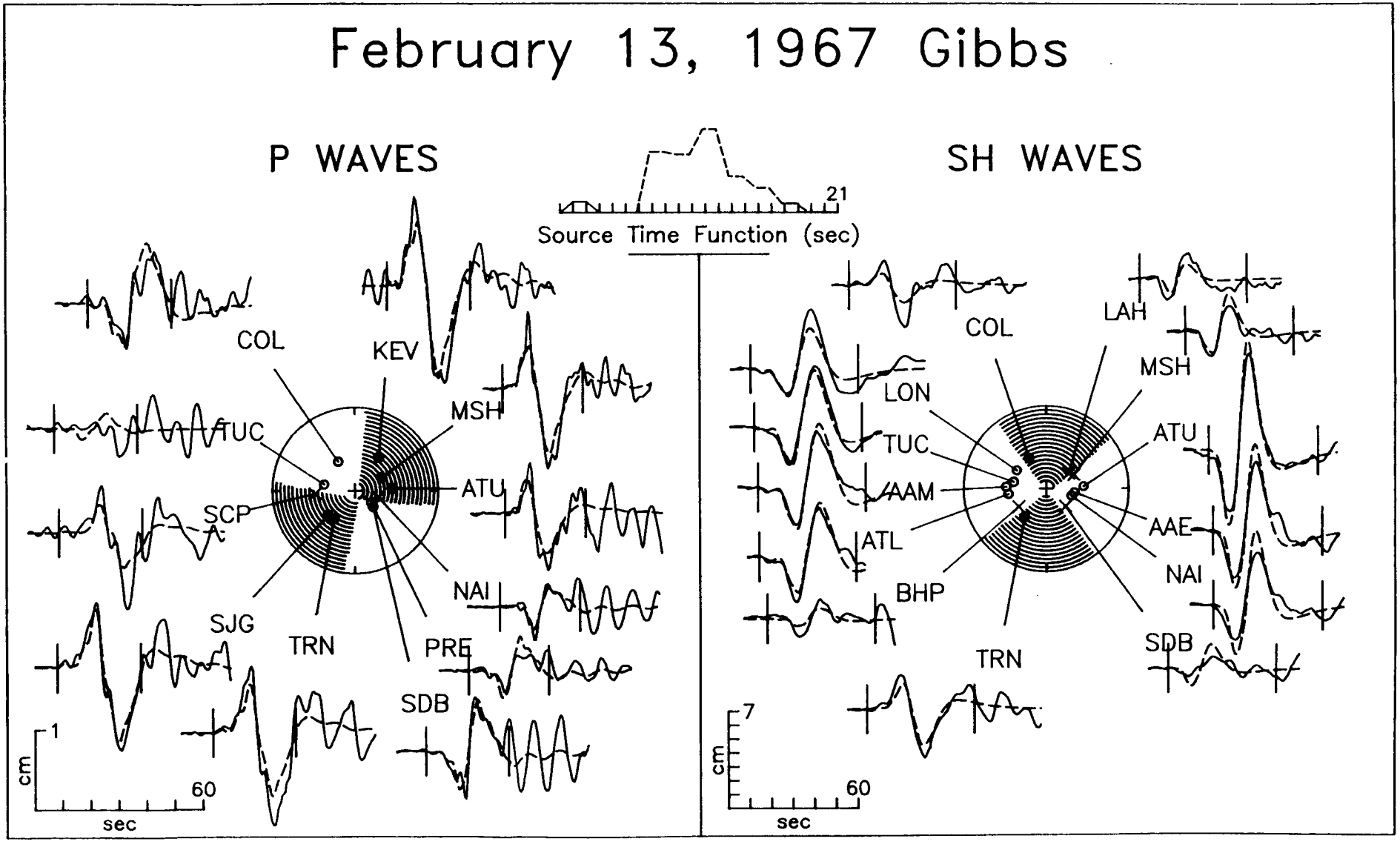
February 13, 1967 Gibbs
P WAVES
SH WAVES
Source Time Function (sec)
21
COL
KEV
TUC
MSH
ATU
SCP
NAI
SJG
TRN
PRE
SDB
1
60
cm
sec
COL
LAH
LON
MSH
TUC
ATU
AAM
AAE
ATL
NAI
BHP
SDB
TRN
7
60
cm
sec

Figure A1

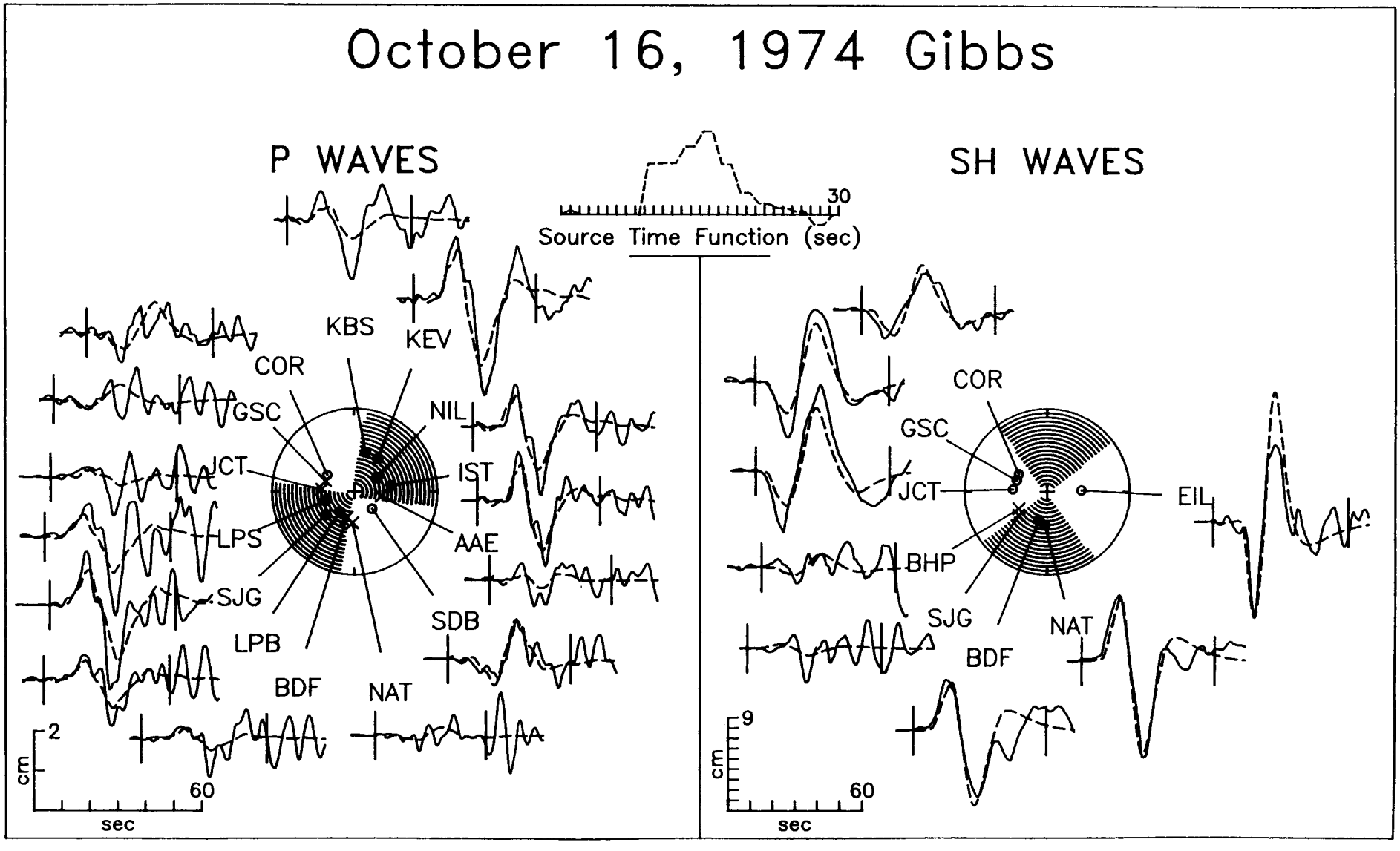
October 16, 1974 Gibbs
P WAVES
SH WAVES
Source Time Function (sec)
30
KBS
KEV
COR
GSC
NIL
JCT
IST
LPS
AAE
SJG
SDB
LPB
BDF
NAT
EIL
BHP
2
cm
60
sec
9
cm
60
sec

Figure A2

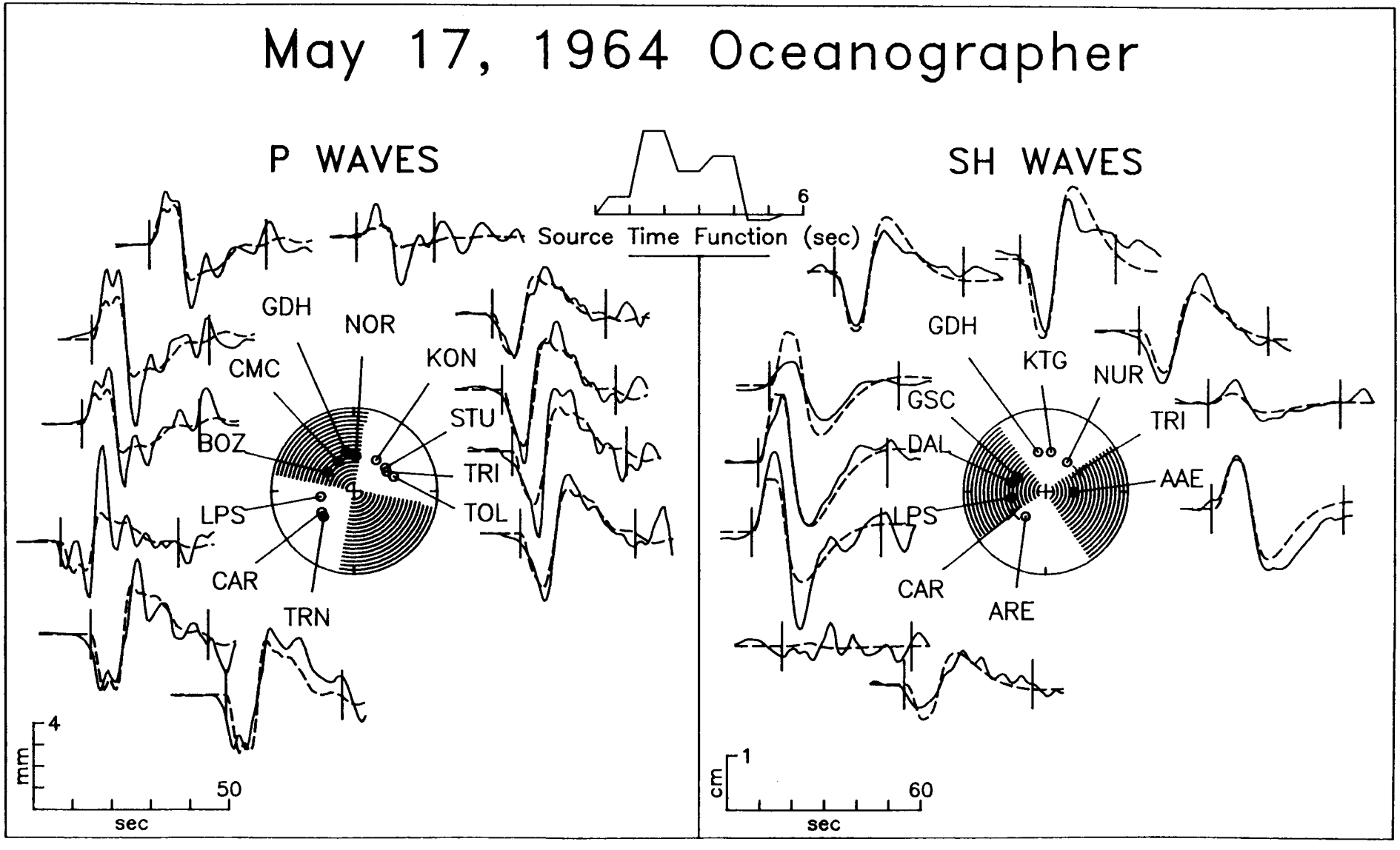
May 17, 1964 Oceanographer
P WAVES
SH WAVES
Source Time Function (sec)
6
GDH
NOR
KON
CMC
STU
BOZ
TRI
TOL
LPS
CAR
TRN
4
mm
50
sec
GDH
KTG
NUR
GSC
TRI
DAL
AAE
LPS
CAR
ARE
1
cm
60
sec

Figure A3

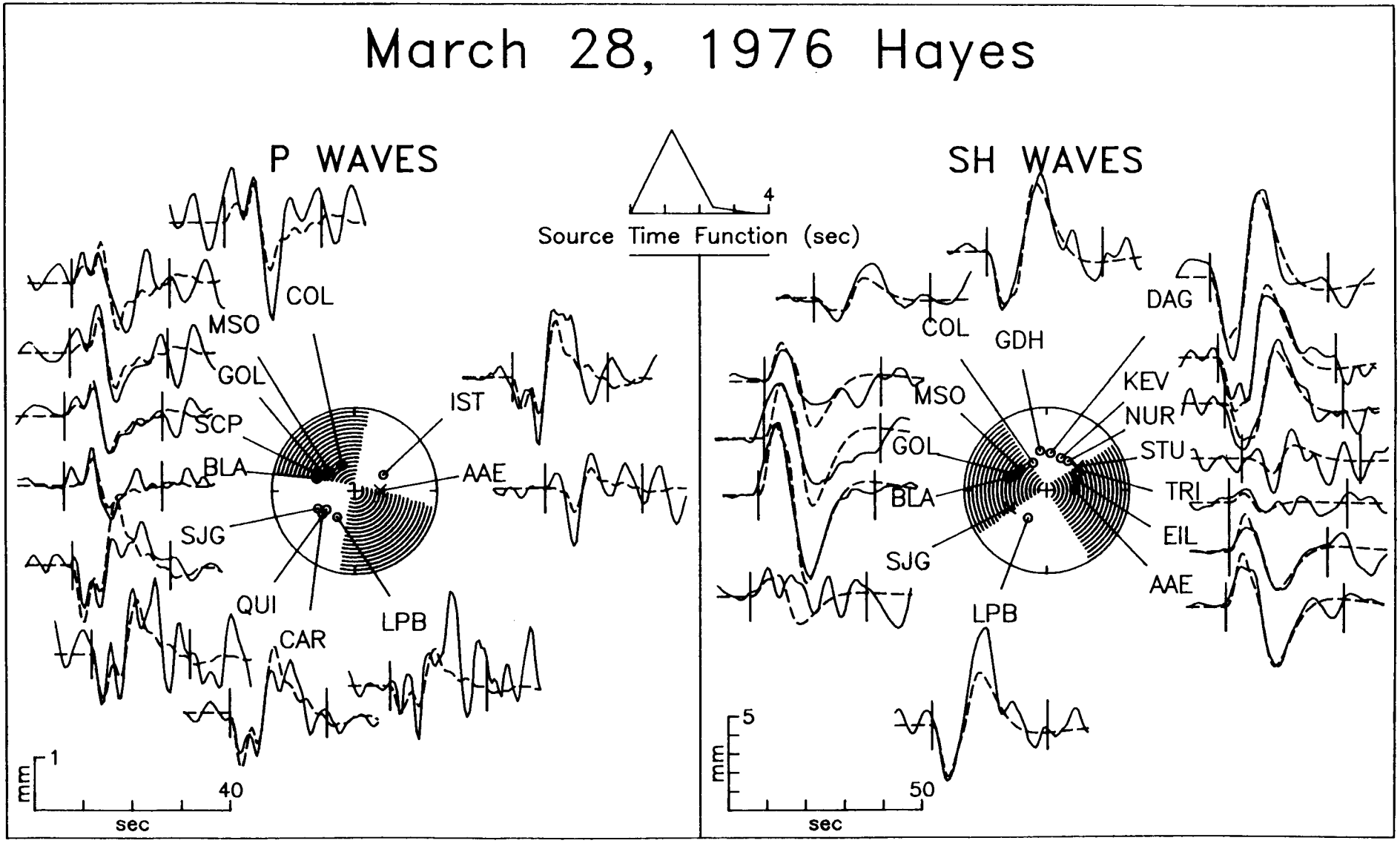
March 28, 1976 Hayes
P WAVES
SH WAVES
Source Time Function (sec)
4
COL
MSO
GOL
SCP
BLA
SJG
QUI
CAR
LPB
IST
AAE
DAG
GDH
KEV
NUR
STU
TRI
EIL
1
40
sec
mm
5
50

Figure A4

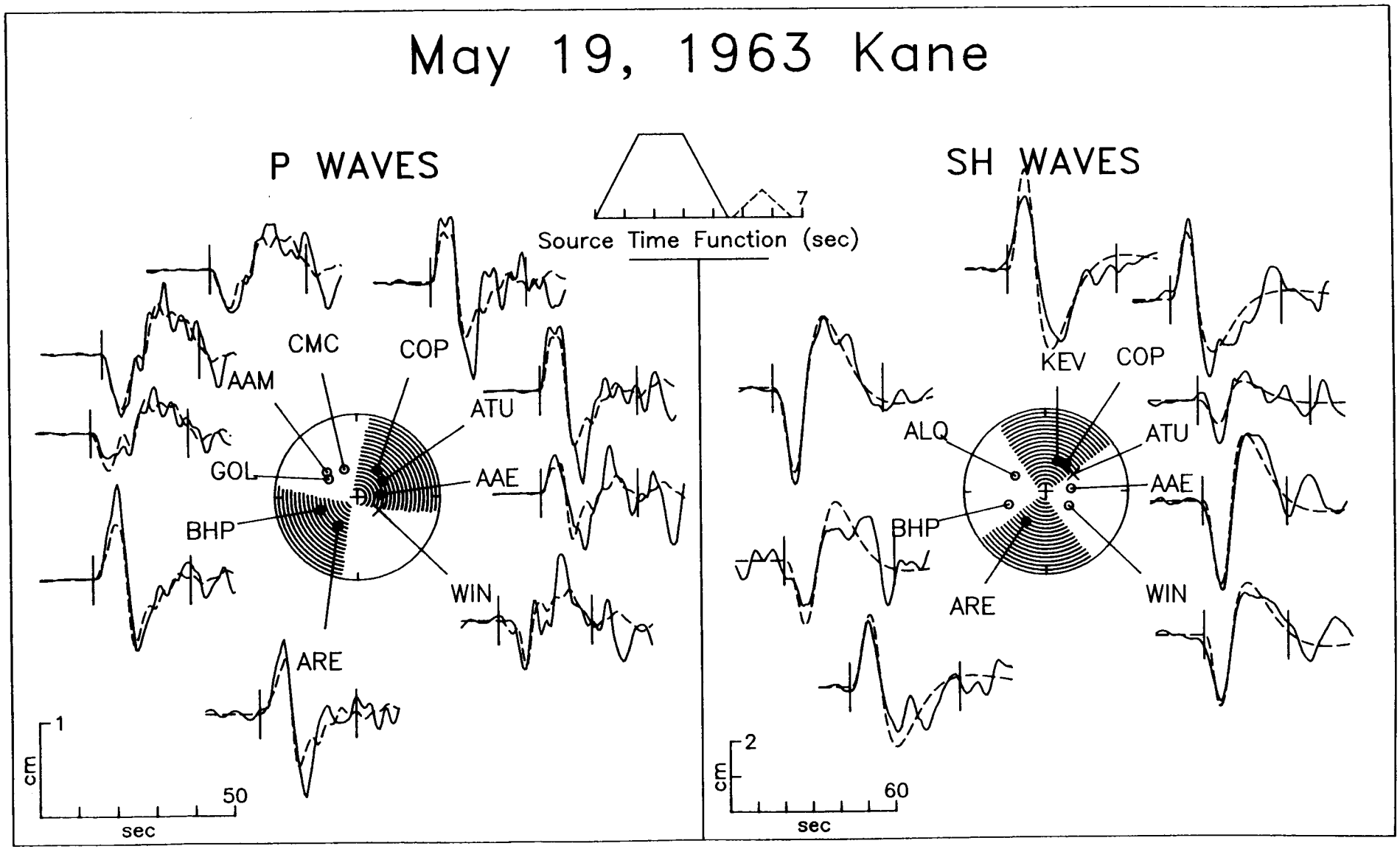
May 19, 1963 Kane
P WAVES
SH WAVES
Source Time Function (sec)
7
AAM
CMC
COP
ATU
GOL
AAE
BHP
WIN
ARE
KEV
COP
ALQ
ATU
AAE
BHP
ARE
WIN
1
cm
50
sec
2
cm
60
sec

Figure A5

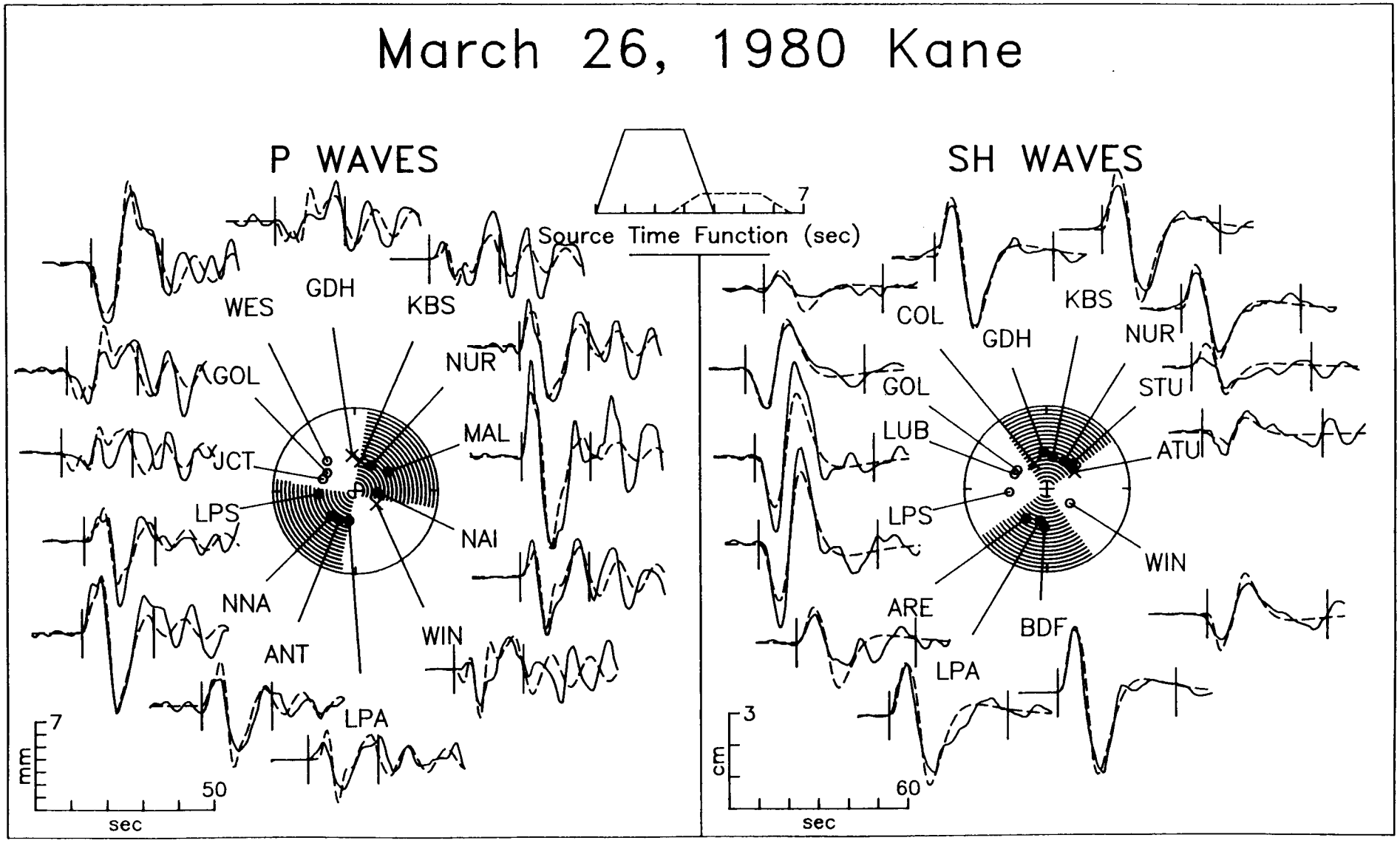
March 26, 1980 Kane
P WAVES
SH WAVES
Source Time Function (sec)
7
WES
GDH
KBS
GOL
NUR
JCT
MAL
LPS
NAI
NNA
ANT
WIN
LPA
7
mm
50
sec
COL
KBS
GDH
NUR
GOL
STU
LUB
ATU
LPS
WIN
ARE
BDF
LPA
3
cm
60
sec

Figure A6

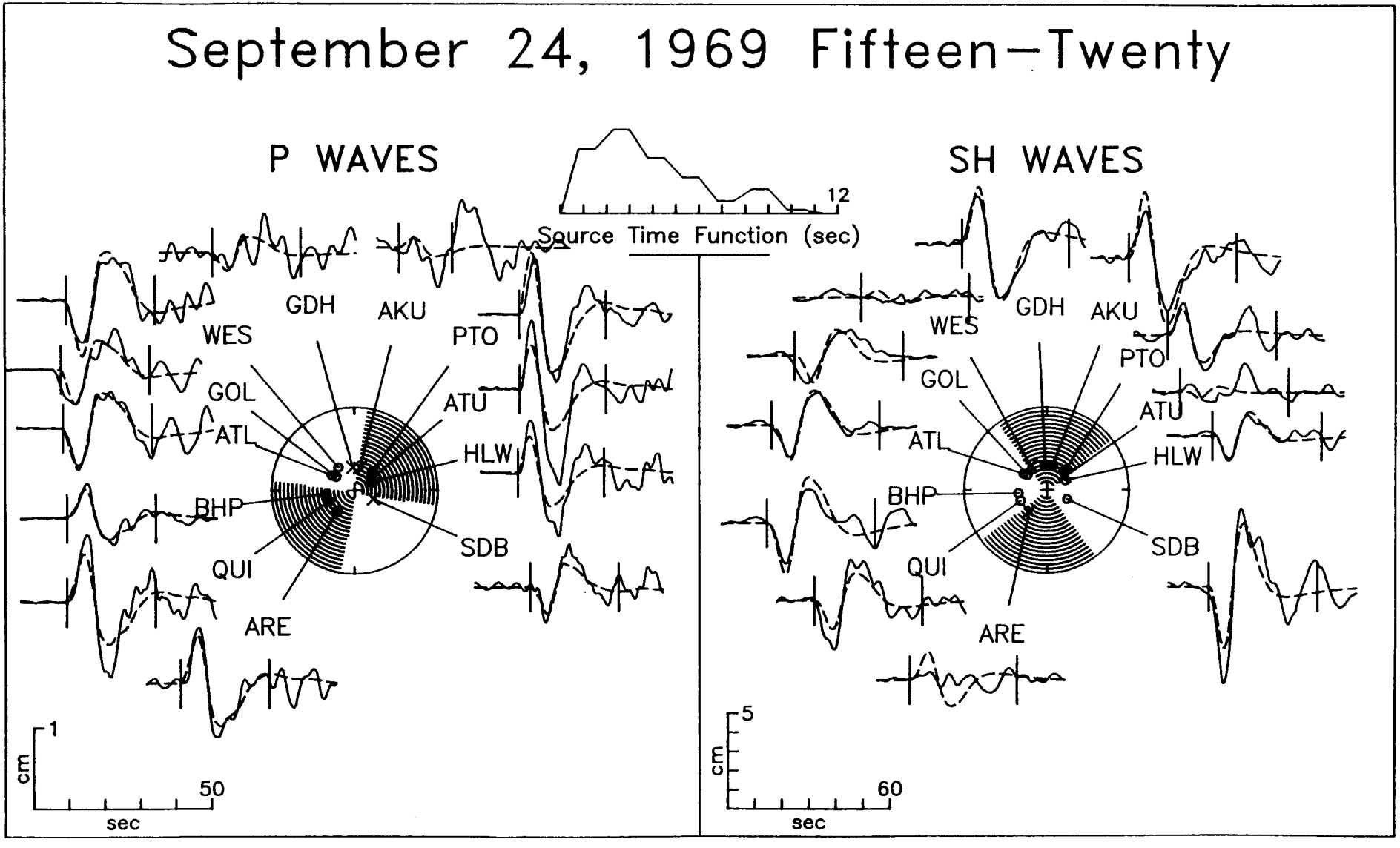
September 24, 1969 Fifteen-Twenty
P WAVES
SH WAVES
12
Source Time Function (sec)
GDH
AKU
WES
PTO
GOL
ATU
ATL
HLW
BHP
SDB
QUI
ARE
1
cm
50
sec
5
cm
60
sec

Figure A7

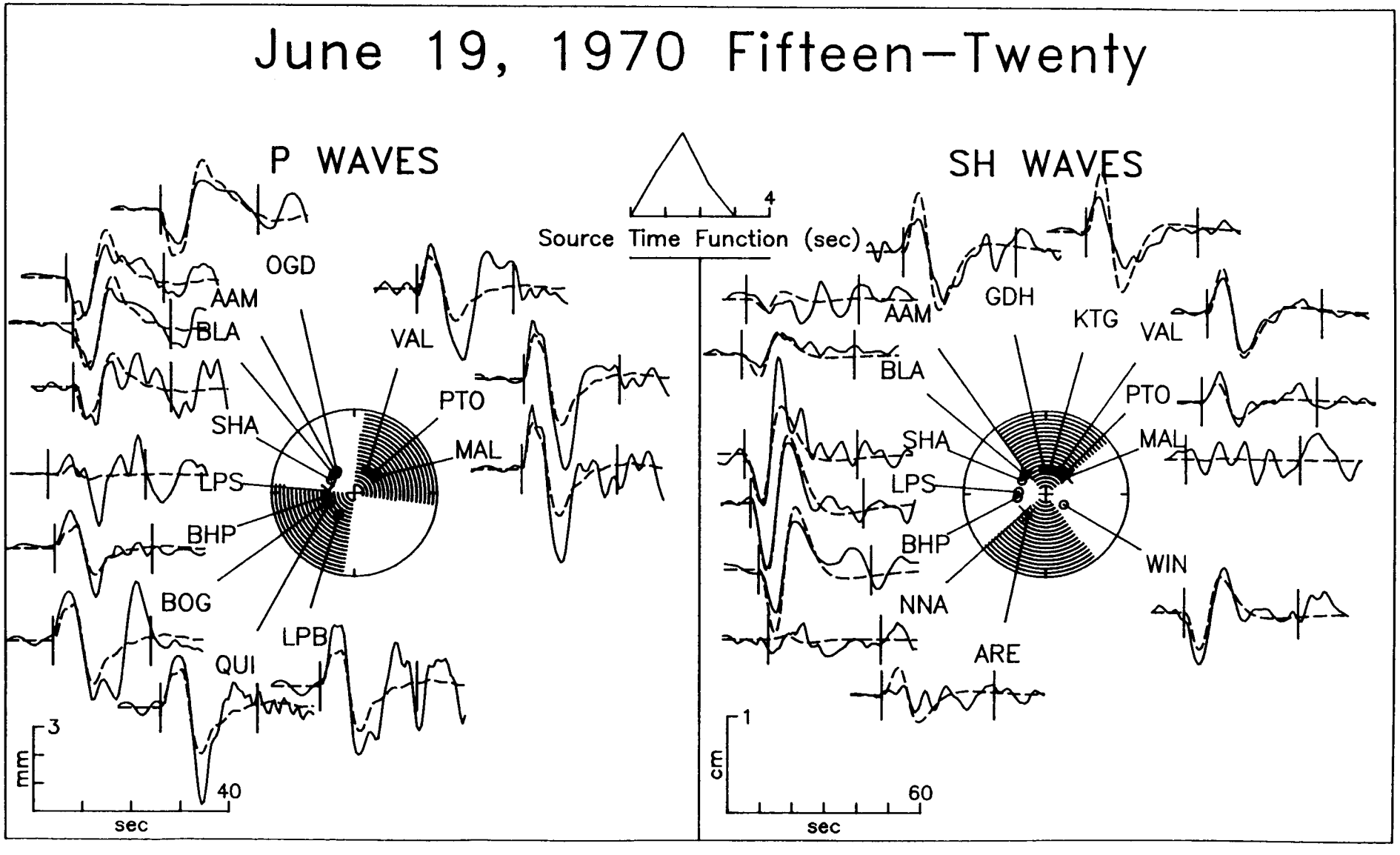
June 19, 1970 Fifteen–Twenty
P WAVES
SH WAVES
Source Time Function (sec)
4
OGD
AAM
BLA
VAL
PTO
SHA
MAL
LPS
BHP
BOG
LPB
QUI
3
mm
40
sec
GDH
KTG
VAL
AAM
BLA
PTO
SHA
MAL
LPS
BHP
WIN
NNA
ARE
1
cm
60
sec

Figure A8

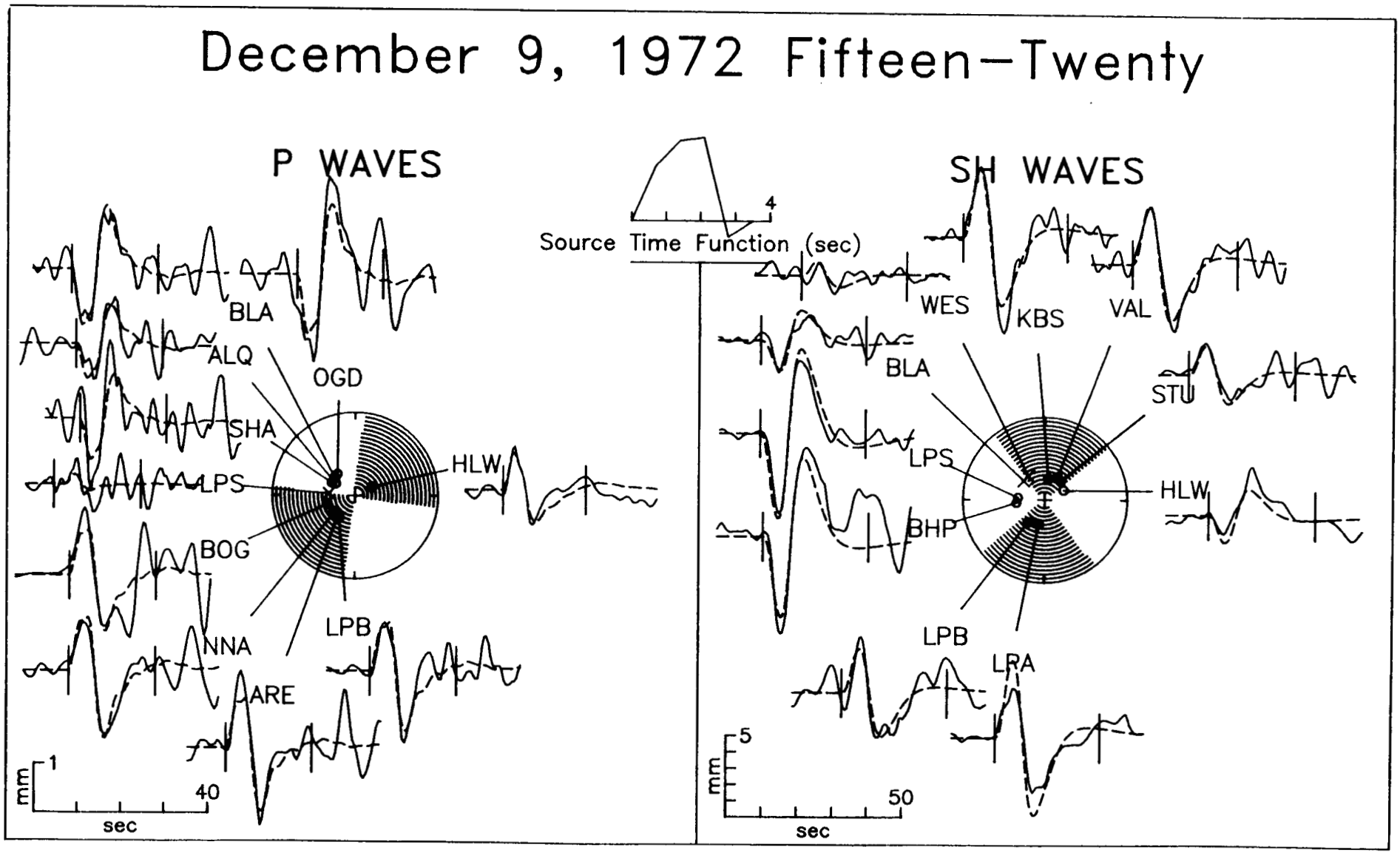
December 9, 1972 Fifteen–Twenty
P WAVES
SH WAVES
Source Time Function (sec)
4
BLA
ALQ
OGD
SHA
LPS
HLW
BOG
NNA
LPB
ARE
1
40
sec
mm
WES
KBS
VAL
BLA
STU
LPS
HLW
BHP
LPB
LRA
5
50
sec
mm

Figure A9

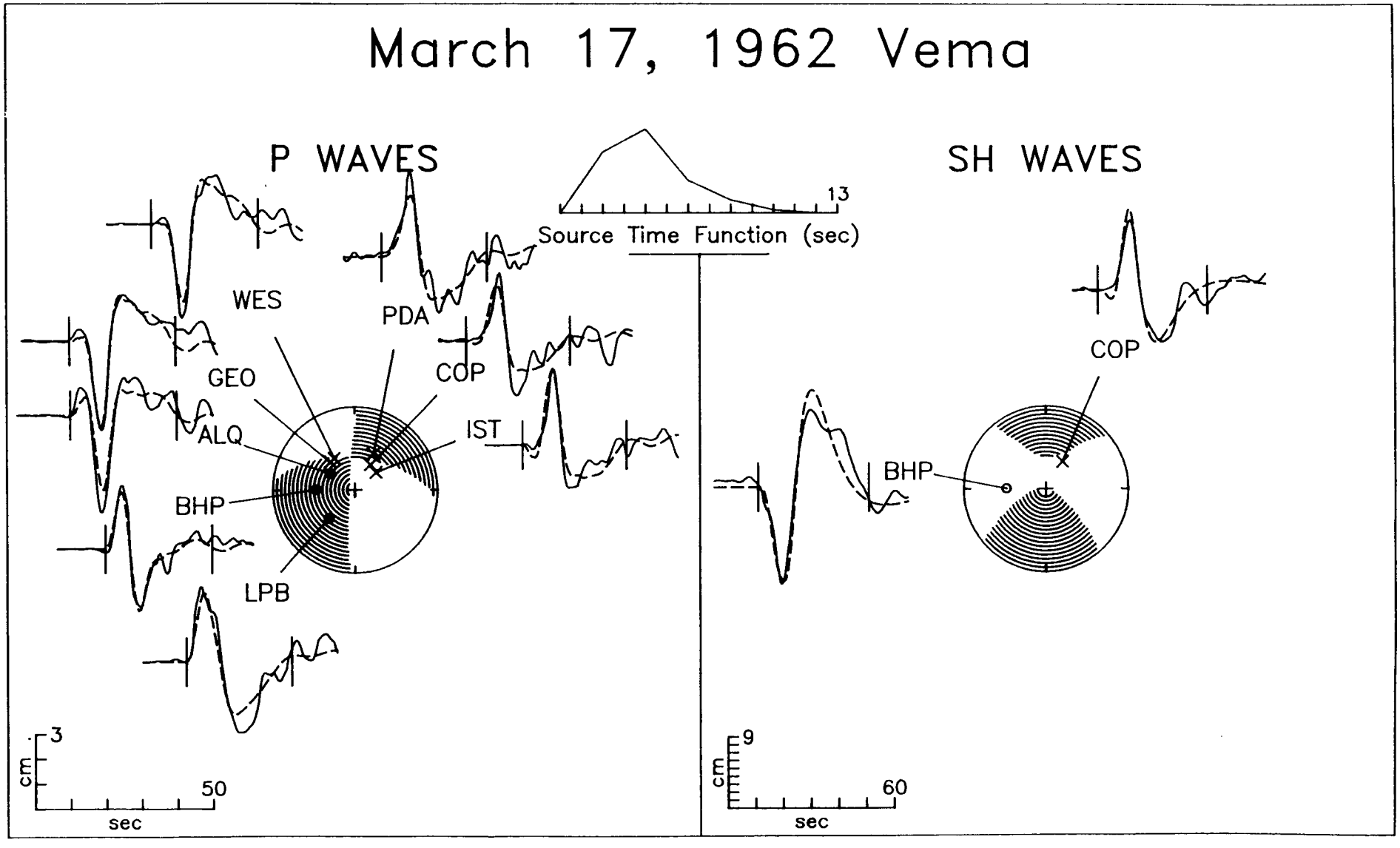
March 17, 1962 Vema
P WAVES
SH WAVES
13
Source Time Function (sec)
WES
PDA
COP
GEO
ALQ
IST
BHP
LPB
COP
BHP
3
cm
50
sec
9
cm
60
sec

Figure A10

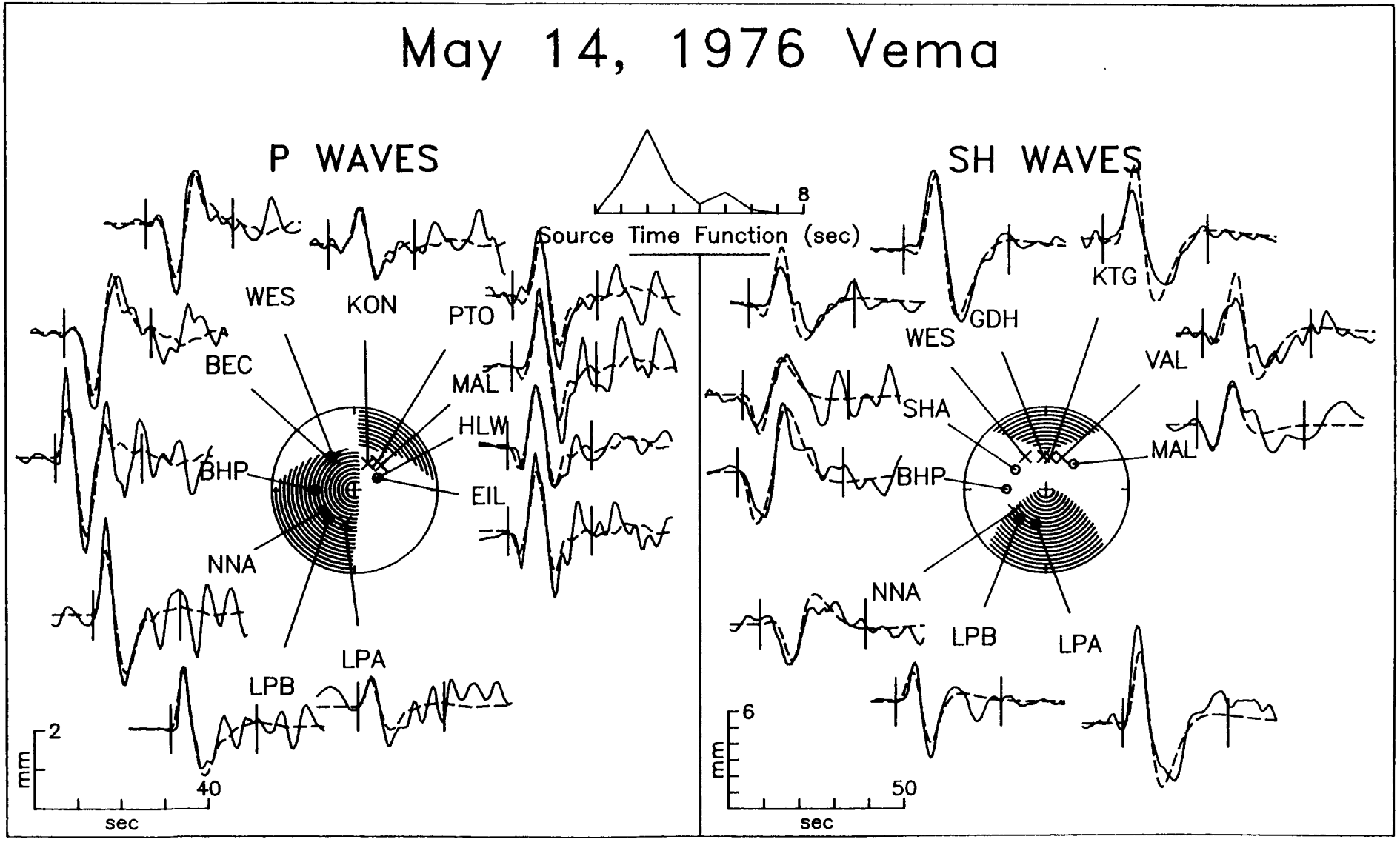
May 14, 1976 Vema
P WAVES
SH WAVES
Source Time Function (sec)
8
WES
KON
PTO
BEC
MAL
HLW
BHP
EIL
NNA
LPB
LPA
2
mm
40
sec
KTG
GDH
WES
VAL
SHA
MAL
BHP
NNA
LPB
LPA
6
mm
50
sec

Figure A11

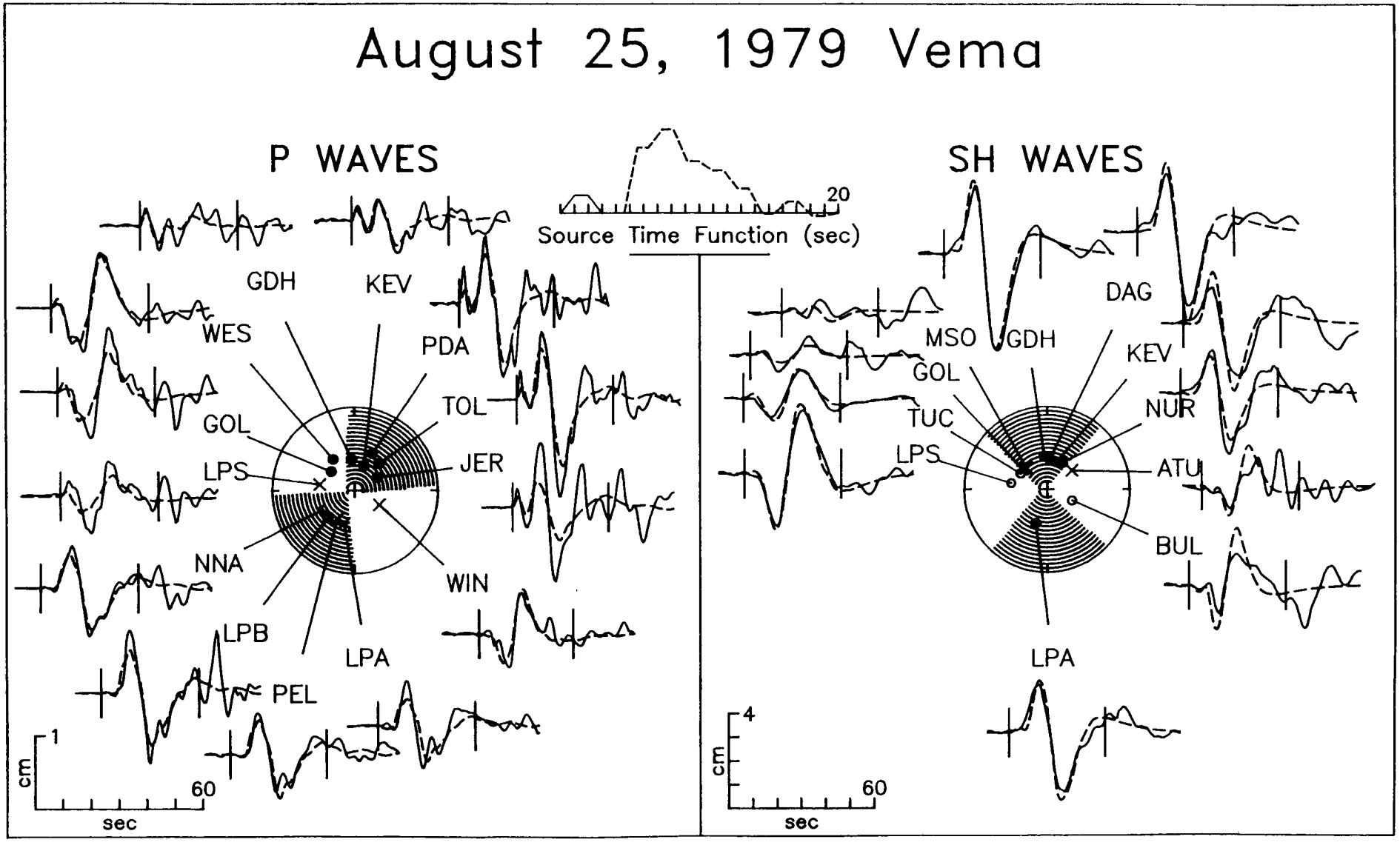
August 25, 1979 Vema
P WAVES
SH WAVES
Source Time Function (sec)
20
GDH
KEV
WES
PDA
GOL
TOL
LPS
JER
NNA
WIN
LPB
LPA
PEL
MSO
GDH
DAG
KEV
GOL
NUR
TUC
LPS
ATU
BUL
LPA
cm
1
60
sec
cm
4
60
sec

Figure A12